A THESIS

FOR THE DEGREE OF DOCTOR OF PHILOSOPHY

Combination of plasma with catalysis and adsorption towards enhancing the decomposition of volatile organic compounds

Trinh Quang Hung

Major of Energy & Chemical Engineering

FACULTY OF APPLIED ENERGY SYSTEM

GRADUATE SCHOOL

JEJU NATIONAL UNIVERSITY

2015. 08

Combination of plasma with catalysis and adsorption towards enhancing the decomposition of volatile organic compounds

Trinh Quang Hung

(Supervised by Professor Dr. Sang Baek Lee)

A thesis submitted in partial fulfillment of the requirement for the degree of

Doctor of Philosophy

2015. 08

This thesis has been examined and approved.

Young Jin Hyun
....

Sang Baek Lee
....

Ho Won Lee
....

Soo Hyoung Moon
....

Young Sun Mok
....

2015. 08

Major of Energy & Chemical Engineering

FACULTY OF APPLIED ENERGY SYSTEM

GRADUATE SCHOOL

JEJU NATIONAL UNIVERSITY

ACKNOWLEDGEMENTS

CONTENTS

ABREVIATIONS

AC	Alternative current
BE	Binding energy
BET	Brunauer–Emmett–Teller
DBD	Dielectric barrier discharge
DEE	Diethyl ether
EPA	USA Environmental Protection Agency
FE-SEM	Field emission scanning electron microscope
FE-TEM	Field emission transmission electron microscope
FTIR	Fourier–transform infrared
GC	Gas chromatograph
HAP	Hazardous air pollutant
HC	Hydrocarbon
HV	High voltage
IAQ	Indoor air quality
ICP	Inductively coupled plasma optical emission spectrometry
ID	Inner diameter
OD	Outer diameter
MFC	Mass flow controller
NMVOC	Non-methane volatile organic compound
NTP	Non-thermal plasma
ppm	Parts per million
SIE	Specific input energy
VOC	Volatile organic compound
WHO	World Health Organization
XRD	X-ray diffraction
XPS	X-ray photoelectron spectroscopy

LIST OF FIGURES

LIST OF TABLES

ABSTRACT

In this thesis, non-thermal plasma (NTP) has been combined with catalysts and dual functional adsorbent/catalysts for abatement of volatile organic compounds (VOCs). The main aims of this work are to optimize the VOC decomposition and energy efficiencies as well as to understand the effect of the scaling up a NTP reactor on the reactor performance.

The work is divided into six studies dealing with plasma-catalytic decomposition of acetone, diethyl ether (DEE) and ethylene. For the purpose of optimizing the VOC decomposition efficiency, various tandem catalyst arrangements of supported transition metal oxides have been investigated for NTP continuous treatment of acetone and DEE (Chapter 3, Sections 3.1 and 3.2). Despite the synergistic effect of NTP and catalysis, the energy efficiency of the process is still poor, especially at low VOC concentration. The cyclic adsorption/plasma oxidation of VOCs is therefore intensively studied in the next studies (Sections 3.3-3.5) in order to further enhance the energy efficiency. Finally, for the sake of practical application, effects of scalability on the NTP reactor performance are under investigation and presented in Chapter 4.

From the first study, the experimental results show that more than 90 % of acetone has been decomposed with a catalyst arrangement of in-plasma MnO_2 (0.1wt% Mn) followed by post-plasma MnO_2 (5.0 wt% Mn), showing a great performance enhancement compared to the tandem bare supports and ZnO (0.1 wt% Zn)-MnO_2 (5.0 wt% Mn) arrangement. The use of MnO_2 either in or post plasma region substantially promotes the acetone decomposition, obviously due to the dissociation of ozone into far more reactive oxygen atoms available for oxidizing acetone. However, as dealing with DEE, an ozone-reactive compound, the presence of Mn-based catalysts in plasma does not positively affect the DEE decomposition compared to the bare and Fe_2O_3 coated cordierites. Even worse, Mn-Fe mixed oxide, the best catalyst for decomposing ozone among prepared catalysts, lowers the DEE removal efficiency because of a large amount of ozone catalytically decomposed in plasma to molecular oxygen. The presence

of a catalyst with a high catalytic activity for zone decomposition in plasma is therefore not beneficial for abatement of the ozone-reactive VOCs. However, as Mn-Fe/cordierite is used in the post-plasma region of the Mn/cordierite one-stage reactor, the removal efficiency has been greatly enhanced by more than 10 %. Choosing appropriate catalysts to couple with NTP is therefore crucial and the nature of treated VOCs should be considered.

The abatement of acetone by cyclic treatment is performed in the third study using silver coated β-zeolite. Dilute acetone (300 ppm) is completely removed from the gas stream by adsorption on zeolite for 100 min and subsequently oxidized in oxygen plasma within 15 min. The acetone abatement by the cyclic operation has largely improved the energy efficiency with about 6.5 times higher than the continuous treatment at the same operating conditions.

Different from acetone, VOCs without polar groups within the molecule will be highly volatile and have low ability of adsorption. In such a case, modification of available adsorbents is needed to improve the adsorption capacity. In the fourth study, cyclic adsorption and oxidation of ethylene on 13X modified with Ag and Ag-M_xO_y (M: Co, Cu, Mn, and Fe) are investigated (Chapter 3, Section 3.4). The incorporation of Ag into zeolite affords a marked enhancement in ethylene adsorption capacity due to the Ag-C_2H_4 complex formation. Among additional metal oxides, Fe_xO_y with high oxidation catalytic activity is able to reduce the ozone emission while keeping a high effectiveness for oxidative removal of adsorbed ethylene.

In the next study (Section 3.5), it is found that the zeolite modification method (i.e., ion exchange and impregnation) strongly affects the ethylene adsorption capacity, by which Ag exchanged 13X (Ag-EX/13X) is superior over Ag impregnated 13X because of the higher dispersion of exchanged Ag^+ active cites. The adsorption and decomposition of ethylene are then performed on Ag-EX/13X with different reactor configurations including one-stage, two-stage and the combination of the two (hybrid). The use of hybrid reactor results in a more

effective generation of ozone and other reactive species, thereby shortening the oxidation time and therefore achieving higher energy efficiency, which is evaluated to be *ca.* 2.4 g $(kWh)^{-1}$.

In the final study, the specific input energy and VOC decomposition efficiency are found to be independent on the reactor size and the way reactor scaled up (i.e., in series or parallel). Based on the finding, the required energy and reactor size can be predicted for treatment of a specific gas stream with known VOC concentration and gas flow rate.

CHAPTER 1: INTRODUCTION

1.1. Air pollution and volatile organic compounds

1.1.1. Air pollution

According to the World Health Organization (WHO), air pollution is contamination of the indoor and outdoor environment by any chemical, physical, or biological agent that modifies the natural characteristics of the atmosphere.

Air pollution causes originate from both natural and human activities. Natural phenomena such as forest fires, lightning, volcanoes and dust storm can emit large amounts of pollutants of carbon oxides, nitrogen oxides, sulfur dioxide and particulate matter into the air. Besides, vegetation, biological decay, soil outgassing and sea spray also release the polluting species [1]. Although the contributions of natural sources are significant, the air pollution especially in urban areas is mainly attributed to anthropogenic causes (e.g., incineration of fossil fuels to produce energy, major industrial processes, and transportation) [2].

The pollutants those are major combustion-generated compounds include particulate matter, sulfur dioxide, nitrogen oxides, carbon monoxide, and unburned hydrocarbons [3]. In which, nitrogen oxides, carbon monoxide, and unburned hydrocarbons are known as precursors of the tropospheric ozone. Excess of atmospheric pollutants causes various environmental problems such as photochemical smog, acidification of soil and water, crop damage, altering rainfall patterns, and greenhouse effects. Exposure to the atmospheric pollutants also adversely impact on human health, from impairing the respiratory system to premature death [4–7].

1.1.2. Volatile organic compounds

Volatile organic compounds (VOCs) as defined by the USA Environmental Protection Agency (EPA) are any compound of carbon, excluding carbon monoxide, carbon dioxide, carbonic acid, metallic carbides or carbonates, and ammonium carbonate, which participates in atmospheric photochemical reactions. This includes any organic compound other than the compounds that have been determined to have negligible photochemical reactivity (e.g. methane, ethane, methylene chloride…). According to this definition a wide variety of organic compounds, such as aliphatic, aromatic and chlorinated hydrocarbons, aldehydes, ketones, esters, organic acids and alcohols can be considered as VOC [8]. Like most of pollutants, VOCs are mainly released from artificial sources, in order of millions tons per year over the world. In South Korea, the amount reported in 2008 was 857,856 ton, while the number recorded in the United States was approximately 15,000,000 ton [9,10].
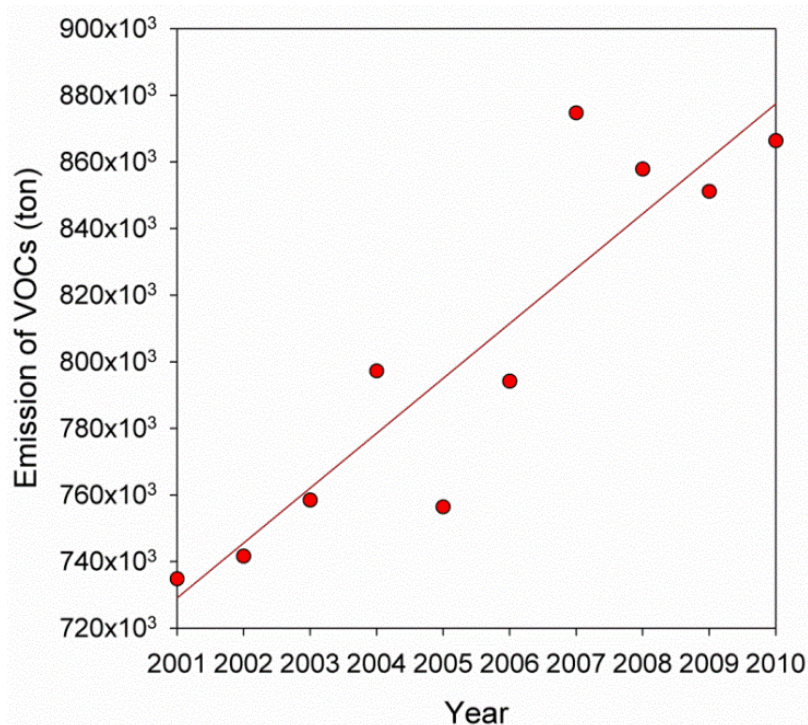
Figure 1. The VOC emission trend, South Korea.

According to South Korean Ministry of Environment, the total amount of emitted VOCs tended to linearly increase from 2001 to 2010, along with the country's economic development (Fig. 1). In 2010, the largest contribution to VOC emissions was made by organic solvent sector with *ca.* 63.7 %, followed by production processes and on-road mobile sources (Fig. 2) [9].
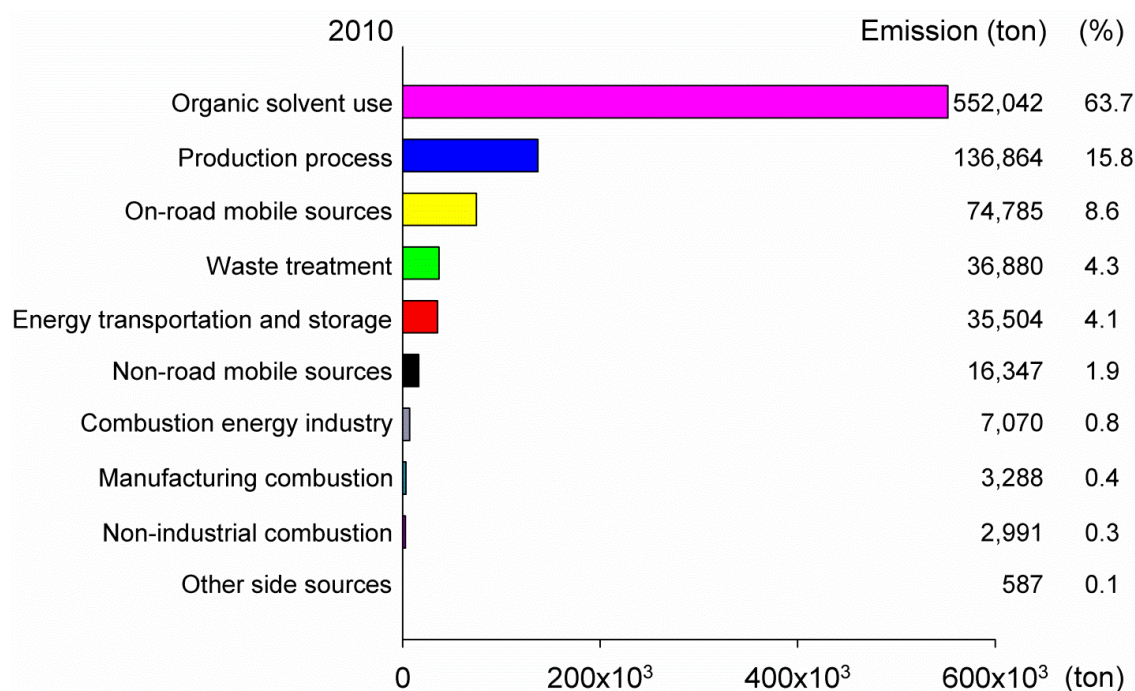
Figure 2. The emission sources of VOCs, South Korea, 2010.

As emitted into the atmosphere, in presence of sunlight and nitrogen oxides (NO_x), VOCs undergo complex photochemical reactions to form ozone, a key component of urban smog [11]. The mechanism of ozone formation from NO_x and VOCs is summarized as follows [12]:

$$RH + OH \rightarrow R + H_2O \tag{R 1}$$

$$R + O_2 + M \rightarrow RO_2 + M \tag{R 2}$$

$$RO_2 + NO \rightarrow NO_2 + RO \tag{R 3}$$

$$NO_2 \xrightarrow{\ h\nu\ } NO + O \qquad\qquad\qquad\qquad\qquad\qquad\text{(R 4)}$$

$$O + O_2 \rightarrow O_3 \qquad\qquad\qquad\qquad\qquad\qquad\qquad\text{(R 5)}$$
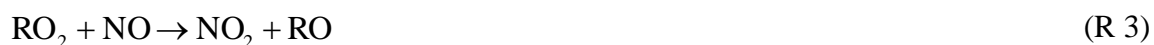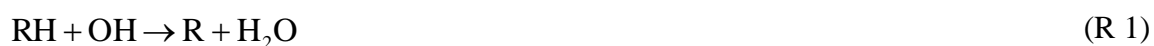
where RH is a VOC and M represents a third body.

In addition, next to carbon oxides and bio-aerosol, VOCs are major substances to be controlled by indoor air quality (IAQ) management. The restriction of indoor VOCs emission becomes urgent recently because nowadays, people stay indoors with more time than outdoors. Typically, citizens in metropolitan areas spend more than 80 % of time in indoor environments [13]. According to EPA, VOCs in indoor air are emitted by a wide array of products numbering in the thousands. Examples include: paints and lacquers, paint strippers, cleaning supplies, pesticides, building materials and furnishings, office equipment such as copiers and printers, correction fluids and carbonless copy paper, graphics and craft materials including glues and adhesives, permanent markers, and photographic solutions. Human who expose to VOCs can suffer various adverse health effects, for example, eye, nose, and throat irritation; headaches, loss of coordination, nausea; damage to liver, kidney, and central nervous system.

1.2. Abatement of VOCs by thermal and thermal catalytic oxidation methods

To cope with the atmospheric pollution, emission standards and regulations related to VOCs and HAPs (hazardous air pollutants) are getting stringent in many countries over the world. At the present stage, end-of-pipe treatment is a reasonable way to meet the environmental goals [14]. Thermal and thermal catalytic oxidation are typically conventional methods for abatement of VOCs, by which VOCs are converted into carbon dioxide and water before being emitted into the atmosphere.

For thermal oxidation, a certain amount of energy is required to overcome activation energy of combustion reaction, therefore temperature of the bulk gas have to be raised to a certain point. The temperatures usually exceeding 800–1200 ℃ are needed to achieve complete combustion, leading to high operating costs and exceeding formation of NO_x [8,15].

In recent years, many studies have focused on the catalytic oxidation of VOCs [16–20]. This technique has benefits of operating under mild conditions (temperatures: 200–500 ℃) and low NO_x formation [21]. Commonly used catalysts are supported precious metals, metal oxides and mixed metal oxides. Precious metals are characterized by good stability and high activity at low temperatures. However, their high cost and sensitivity to poisoning by chlorine and formation of toxic polychlorinated compounds have motivated the search for alternative catalysts. Oxides of transition metals, mainly Mn, Co, Fe and Cu have been explored intensively as effective and more economical catalysts for total oxidation of VOCs. A common feature of these materials is the presence of multiple oxidation states of transition metal in the structure, resulting in the ability of cations to undergo reversible oxidation and reduction under reaction [21–27].

A great advantage of the catalytic oxidation is that it can be used to treat exhausted air from the mobile sources [8,28]. In 1970s, a Pt-Pd catalyst known as two-way converter was utilized for oxidizing carbon monoxide (CO) and hydrocarbons (HC) those are among major combustion-generated compounds. Soon after, in 1980, a three way catalyst (Pt-Pd-Rh or Pt-Rh), which simultaneously removed CO, HC and NO_x was introduced, and it has been extensively used until today to reduce the emissions of combustion engines [29,30]. The catalyst industry has improved the performance of the three-way catalyst by utilizing improved formulations and layered structures. The new catalyst designs are more durable and thermally resistant. Development work continues to further improve the catalyst technology [31].
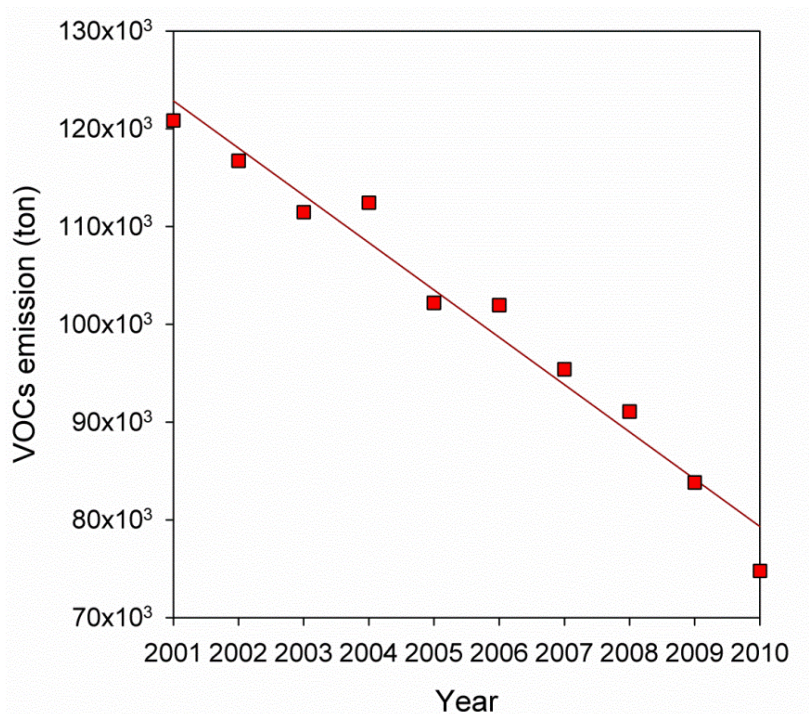
Figure 3. VOC emission by on-road mobile sources, South Korea

As seen from Fig. 3, in contrast to the total VOCs released, the emission by on-road mobile sources in South Korea has significantly decreased by ca. 38 % within the last decade, probably due to the performance improvement of catalytic converters used in cars along with more stringent emission standards.

1.3. Nonthermal plasma in combination with catalysis/adsorption for VOC abatement

1.3.1. Nonthermal plasma for VOC abatement

a) Physics of nonthermal plasma

Plasma, a quasi-neutral gas, considered as the fourth state of matter constitutes more than 99 % matter of the universe. There is a large number of different species existing in plasma including electrons, positive and negative ions, free radical, gas atoms and molecules in the ground or any higher state of any form of excited species. Nonthermal plasma (NTP) is

characterized by its thermal non-equilibrium state with electron temperature much higher than those of ions and neutral species [32]. For this type of plasma, the gas temperature is virtually equal to the atmospheric temperature, and the electron temperature is of the order of 1–10 eV or several tens of thousands of K [33].

NTP can be generated at atmospheric pressure and room temperature by either corona discharge or dielectric barrier discharge (DBD). Corona discharge has many applications where small concentration of exited or charged species are needed, for instance, electrostatic precipitators, copying machines, dry-ore separation system and high-speed printout devices. Meanwhile, DBD discharge is predestined for applications of large volume plasma chemistry such as ozone generation, surface treatment and air pollution control. Basic electrode arrangements of DBD configurations are shown in Fig. 4. They are distinguished by the presence of at least one insulating layer typically glass or ceramic materials between two planar or cylindrical electrodes connected to an AC power supply [15].

Breakdown in the gas gap between two electrodes is locally initiated by applying an electric field larger than the breakdown field. The growing electron avalanches quickly produce such a high space charge that self-propagating filament streamers are formed. The DBD plasma at atmospheric pressure is characterized by a large number of short-lived micro-discharges. These micro-discharges are almost cylindrical plasma channels and spread into large surface discharges at dielectric surface. The dielectric serves as dual purpose to limit the amount of charge and energy imparted to an individual micro-discharge, and at the same time distributes the micro-discharges over the entire electrode area. The formation of micro-discharges is featured by electron multiplication; excitation, dissociation, and ionization processes and space charge accumulation [35].
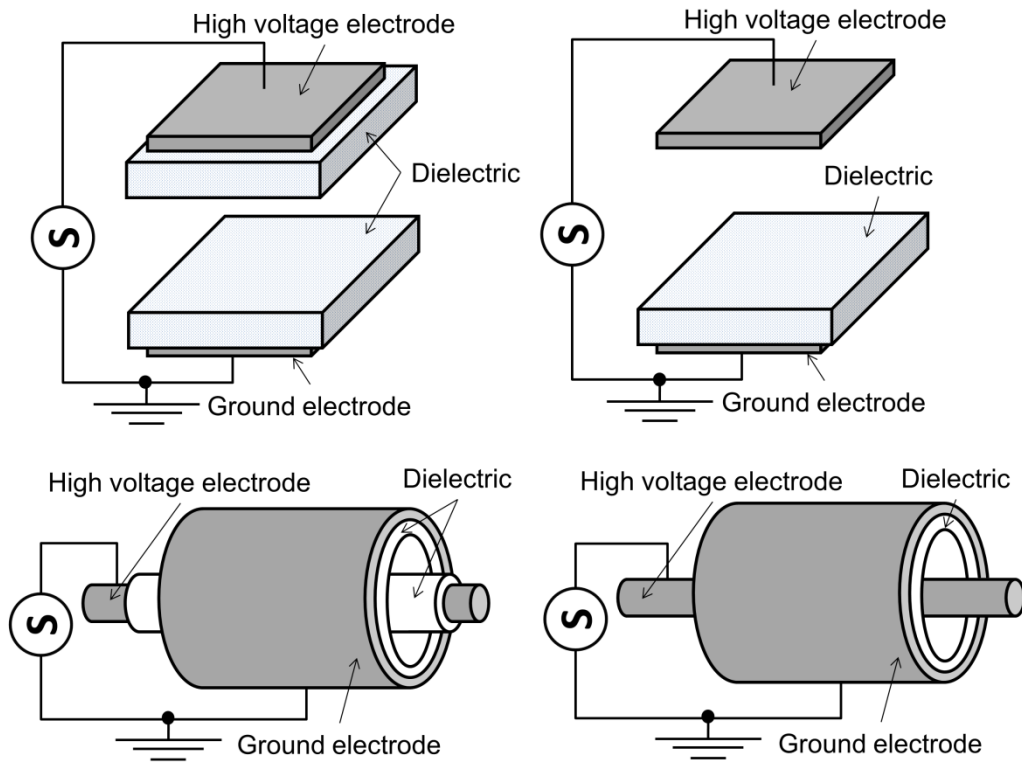
Figure 4. Typical DBD reactor configurations.

The charge transferred in the micro-discharge or accumulated on the dielectric plays an important role in the characteristics of the DBD, since it not only affects the electric field in the gas gap, but also enhances the atomic processes in the discharge [36]. During the rising part of external voltage, additional micro-discharges are initiated at new locations because the presence of residual charges on the dielectric has reduced the electric field at positions where micro-discharges have already occurred. On voltage reversal, however, the next micro-discharges will form at old micro-discharge locations. Since the voltage has collapsed at these locations, it takes less external voltage swing to reach breakdown in the following half period of opposite sign. Consequently, high-voltage low-frequency operation tends to distribute the micro-discharges on the available dielectric surface, while low-voltage, high-frequency operation tends to reignite

the old micro-discharge channels every half period. This memory effect due to charge accumulation on the dielectrics is a dominant feature in all barrier discharges [37].

b) Chemical activity of nonthermal plasma

High chemical efficiency is the main advantage of NTP with nearly all input energy converted to energetic electrons without significant heating of the bulk gas. The hot electrons can trigger many different chemical processes such as excitation, ionization and dissociation, leading to formations of various active species that can further react with more stable ones. Examples of these species are OH, O, and N radicals; excited N_2 molecules; and atomic and molecular ions (e.g., O^+, O_2^+) [38].

The elementary processes in NTP can be broadly divided into a primary process and a secondary process based on the time-scale of streamer propagation. Ionization; electronic, vibrational, and rotational excitation; fragmentation; light emission; and charge transfer are those processes included in the primary process within a timescale of about 10^{-8} s. The secondary process is the subsequent chemical reaction involving the products of primary processes. Some additional radical species and reactive molecules (O_3, HO_2, and H_2O_2) are also formed by radical-neutral recombination in the secondary process [39].

In treating gaseous pollutants in ppm (parts per million by volume) range, it is hard to expect that a direct decomposition of dilute pollutant through collisions with energetic electrons in the primary process play an important role. The majority of the electron energy is transferred to the dominant gas molecules of nitrogen and oxygen through many inelastic collisions and then leads to the formation of radicals. The decomposition of gaseous pollutants starts to occur only after the formation of radicals is initiated [40].

c) Nonthermal plasma for VOC abatement

Nonthermal plasma has been reported as an effective tool to eliminate VOCs from effluent gases due to its unique properties over the conventional techniques such as quick response at ambient temperature, achievement of high electron energies within short residence times, no concentration gradient limited and no additional disposal required. In addition, the system compactness, easy operation and flexible power adjustment to match the source flow are also advantages of NTP over other methods [41,42].

Unfortunately, high reactivity usually means a poor selectivity. Reactive species present in plasma not only react with pollutants but also undergo recombination process, leading to a poor selectivity of the radical, especially when degrading dilute pollutants [39]. The low energy efficiency, poor material balance and formation of unwanted byproducts are major obstacles for NTPs to stand alone in real applications. As an example, ethylene (concentration: 1898 ppm) decomposition using NTP was investigated by M. S. Gandhi et al. [43]. Among used reactors, the conventional DBD reactor resulted in a relatively low ethylene decomposition efficiency (ca. 40 % at specific input energy (SIE) of ca. 800 J L^{-1}) and poor selectivity toward carbon dioxide (CO_2). In another work, Holzer et al. reported that plasma oxidation of methyl tert-butyl ether (MTBE, 200 ppm) and toluene (450 ppm) resulted in carbon oxides (CO_x) selectivity smaller than 30 % at SIE above 1000 J L^{-1} for both VOCs [44]. Similar results were also observed in other studies [45,46]. Besides, various secondary undesired byproducts such as CO, formaldehyde (HCHO), formic acid (HCOOH), ozone (O_3), nitrogen oxides (NO_x and N_2O) were detected in plasma treated gases [47,48].

1.3.2. Combination of nonthermal plasma and catalysis for VOC abatement

In order to make NTP applicable, researchers have been trying to combine NTP with catalysis for removal of VOCs. The basis for the combination is that NTP and catalysis can compensate the weaknesses of each other. While NTP is nonselective but can be ignited under normal conditions of temperature and pressure, catalysis is featured as a selective process in which catalyst is usually activated at high temperature. The most important characteristic of this complementary combination is that plasma enables catalyst to work even at room temperature, offering advantages for treatment of VOCs in terms of energy efficiency, product selectivity and carbon balance [49,50].

a. *Plasma-catalysis reactor configuration*

Plasma-catalysis reactors are usually packed-bed DBD reactors. In which, catalyst is placed either in or post plasma region known as one- or two-stage configuration (also referred as one- or two-stage arrangement), respectively [51]. For the one-stage configuration, catalyst is directly in contact with electrical discharge and active species those are generally short-lived, e.g., excited-state atoms and molecules, reactive radicals, photons, and electrons. Meanwhile, for the two-stage configuration, catalyst is separated from plasma and exposed only to long-lived active species, namely ozone and, possibly, vibrationally excited species [52]. From the physics point of view, the average electric field in the one-stage packed-bed reactor will be enhanced compared to the empty reactor due to the short distance in the adjacency of contact points, resulting in the improvement of oxygen dissociation process and formation of oxidative radicals and reduction of gas breakdown voltage [53]. It has been experimentally demonstrated that lattice oxygen of catalyst can be also activated by plasma for oxidation of VOCs [39,54,55]. Moreover, the catalyst with a significant adsorption capacity will prolong the pollutant retention

11

time and increase the pollutant concentration in the plasma region, thereby improving the selectivity and removal efficiency [56].

b. *Catalysts used in plasma-catalysis combined system for VOC abatement*

In general, catalysts those are used for thermal catalytic oxidation are capable to work under plasma irradiation. Various supported catalysts such as Pt/TiO_2, Ag/TiO_2, $Cu/HZSM$-5, Pd/Al_2O_3, FeO_x/SBA-15, MnO_x/SMF, Mn-Co/Al_2O_3, etc., have been combined with plasma for VOC abatement purpose [57–63]. Due to the advantages from direct plasma-catalyst interaction, many studies focused have on the one-stage combination and found positive synergy of plasma and catalyst which significantly improves the VOC removal and energy efficiencies, enhances the VOC mineralization and suppresses the formation of byproducts [64–68].

Among catalysts, silver is not only known as a unique catalyst used for commercial production of ethylene oxide but also considered as one of the best catalysts for ozone decomposition and deep VOC oxidation [51,52,69–75]. The high activity of this metal in the oxidation process is associated with its ability to present at multiple oxidation states (+1 to +3) and the easy dissociation of oxygen molecules on its surface [76]. In combination with plasma, supported Ag strongly enhances the plasma discharges by facilitating generation of surface streamer. This physical property is correlated with the chemical effect of the catalyst. For example, Ag has better catalytic activity than Cu, which is consistent with the trend in plasma expansion [49,50]. According to Kim et al. [77], Ag is also superior over Pt for cyclic treatment of VOCs (i.e., VOC adsorption followed by oxygen plasma oxidation) due to its much larger enhancement factor than that of Pt. The enhancement factor is used to evaluate the potential of a catalyst for the cycled system and defined as the ratio of decomposition efficiency of VOC with respect to the O_2 partial pressure at the same specific input energy.

In other studies, iron (III) oxide (Fe_2O_3) was found to be the most desirable catalyst among transition metal oxides ((TiO_2, ZnO, V_2O_5, Fe_2O_3, Co_3O_4, MnO_2, and CuO) in combination with plasma for removal of diesel particulate matter (PM) [78,79]. The highest catalytic activity for the PM oxidation with Fe_2O_3 has been suggested to be due to the balance between the reduction rate and the re-oxidation rate within the redox catalytic cycles. Recently, M. Lu et al. investigated the decomposition of toluene in DBD plasma using FeO_x supported on SBA-15 and revealed that Fe^{2+} species with relatively low reduction temperature and excellent oxygen adsorption ability played a crucial role in the degradation of toluene [54].

Manganese oxides were also widely investigated in both one- and two-stage combinations for VOC abatement [56,80,81]. Ozone formed in plasma is effectively decomposed on manganese-based catalysts, forming atomic oxygen which plays a key role in VOC oxidation [82–86]. Recently, Mn-Fe mixed oxide has gained attraction due to its excellent activity for ozone decomposition, being capable to combine with NTP for VOC removal [87,88].

Unlike packed-bed reactor, a reactor using porous alumina or cordierite monoliths as catalyst supports results in low pressure drop, being meaningful from practical viewpoint. Plasma generated in a monolith with multi-parallel channels can exist in both filament and surface discharge modes. The strong filament discharge is advantageous for fragmentation of VOCs and ozone formation. Meanwhile, surface discharge is crucial for catalyst activation [89]. The combination of plasma with alumina or cordierite monoliths for environmental purpose has been recently reported, showing their potential for real application [90–93].

1.3.3. Combination of NTP-catalysis with adsorption for VOC abatement

Combination of adsorption and plasma-catalytic oxidation in one process for VOC abatement is a prominent way to further enhance the energy efficiency, especially at low-level VOC contamination [59,94–97]. In such a cyclic process, dilute VOCs are first removed from the gas stream and concentrated on the adsorbent without electrical discharge, and in the subsequent step, the enriched VOCs are plasma-catalytically oxidized. The intermittent operation includes a long time adsorption followed by a short time oxidation, leading to a great deal of reduction in the energy consumption [98].

As a result of various intriguing properties such as high adsorption capacity, molecular-sieving effect, and thermal stability, zeolite is a commonly used VOC adsorbent [99–101]. The adsorption behavior depends upon various physicochemical properties of both VOCs and zeolite (e.g., volatility, acidity, Si/Al ratio, crystal structure, pore structure, surface area, and pore volume) [102]. With highly volatile compounds such as ethylene, modification of available zeolites is needed to enhance the adsorption capability. In previous reports, zeolites such as NaX and NaY have been modified with various cationic surfactants and exchanged ions those have high affinity towards VOCs, thereby largely improving the adsorption capacity [103–106].

1.4. The concerns and objectives of this study

Although NTP generated by dielectric barrier discharge can produce various active species capable for VOC decomposition, the short-lived species (e.g., excited N_2, N, O and OH radicals) are highly nonselective to react with not only VOC but also with the background gas molecules and undergo the recombination reactions. In this sense, the effective recycling of plasma-induced ozone, a long-lived species for VOC oxidation is a good way to enhance the

VOC removal efficiency of plasma treatment. The combination of NTP with a catalyst could be beneficial for the ozonation of VOCs by changing the reaction pathway and inducing the formation of adsorbed atomic oxygen with higher activity for oxidation reactions than that of gaseous ozone. However, the presence of an ozone decomposition catalyst in NTP may not result in the same effect for treatment of VOCs those have different natures of reactivity towards ozone. For comparative study, acetone and diethyl ether are chosen as the model VOCs. In which acetone, a persistent VOC, hardly reacts with ozone in the gas phase, while diethyl ether is known as an ozone-reactive compound. The effects of the ozone decomposition catalysts such as MnO_2 and Mn-Fe mixed oxides on the continuous treatment of these VOCs are investigated in combination with NTP. Besides, the influences of other catalysts such as photocatalyst (ZnO) and oxidation catalyst (Fe_xO_y) are also tested. Despite many studies have proven the synergistic effect of NTP and catalysis, most of them dealt with the one- and two-stage combinations separately. This work tries to simultaneously couple NTP with catalysts in both in- and post-plasma regions (called hybrid reactor) in order to promote the decomposition of VOCs at low temperature by choosing the appropriate catalysts for each plasma region. The performances of one- and two-stage reactors are also under investigation for comparison and to help elucidate the mechanisms for VOC oxidation.

In an effort to further enhance the energy efficiency of acetone abatement, acetone contaminated air stream is treated using cyclic adsorption-plasma oxidation instead of continuous treatment with β zeolite as the adsorbent. The effect of silver coated on the zeolite on both oxidation time and ozone formation is examined along with the stability of the adsorbent/catalyst after several cycles of treatment.

For cyclic or sequential treatment, the adsorbent/catalyst is required to have both good characteristic for VOC adsorption and high catalytic activity for oxidation of adsorbed VOCs under NTP conditions. The VOCs with high molecular mass or possessing the polar groups in

15

the molecules such as acetone usually have high adsorbability on the solid surface. However, for compounds those are highly volatile (e.g., ethylene), the adsorption capacities of available commercial zeolites such β and 13X zeolites are not sufficient to completely adsorb the VOCs from gas stream for a long period of time and therefore, modification of these adsorbents is needed. In order to intensively study the cyclic adsorption-plasma oxidation of VOCs, the effects of the modification of 13X zeolite surface by different transition metals (e.g., Ag, Ag-Fe, Ag-Cu, Ag-Mn, and Ag-Co) and the modification methods (e.g., ion exchange and impregnation) on the ethylene adsorption as well as on the plasma-oxidative desorption of adsorbed ethylene are investigated. The performance of reactor with different configurations is also evaluated in order to minimize the oxidation time and energy consumption.

Most of studies on NTP for VOC abatement are performed on the laboratory scale. For practical purpose, the effects of scaling up a DBD packed-bed reactor is studied in this work by investigating the dependence of VOC removal rate on the reactor size, discharge power and specific input energy.

1.5.   Organization of the thesis

The thesis begins with chapter 1, which gives an overview of VOCs and the techniques for abatement of VOCs. In this chapter, non-thermal plasma in combination with catalysis and adsorption/catalysis is focused to be introduced. The objectives and structure of the thesis are given in this chapter (chapter 1). The following chapter (chapter 2) describes the methodology, where the nature of selected VOCs, experimental system, and details of reactor configuration, analyses and catalyst preparation methods are described. Chapter 3 includes sections 3.1 to 3.5 those are redrafted from published scientific articles, presenting experimental results and discussion related to plasma decomposition of acetone, diethyl ether and ethylene. Chapter 4

deals with the scale-up of plasma packed-bed reactor. The influences of reactor size and process parameters on the VOC removal efficiency are given. Finally, general conclusions drawn from the experimental results obtained in this thesis are provided in chapter 5.

CHAPTER 2: EXPERIMENTAL METHODS

2.1. Selected model VOCs

In this thesis, acetone (C_3H_6O), diethyl ether ($C_4H_{10}O$) and ethylene (C_2H_4) are chosen as model VOCs to be treated.

Acetone is used in innumerable products (e.g., solvent and paint thinner) and known to cause carcinogenic effect on human beings [107,108]. Unlike other solvents such as ethers and esters, ketones including acetone, methyl ethyl ketone and methyl isobutyl ketone are chemically very stable, being recalcitrant to decomposition.

Diethyl ether (DEE) is among the more common of the aliphatic ethers present in the atmosphere due to its use as fuel additive and solvent, contributing to the formation of photochemical smog. Aliphatic ethers are generally more reactive in the atmosphere than alkanes of similar chain length, and have propensities for ozone production on urban and regional scales that are similar to or larger than alkanes of similar size [109].

Interestingly, ethylene is commonly released from both man-made and natural sources. It is an important raw material widely used in various industrial reactions such as polymerization, oxidation, halogenation, alkylation and oligomerization. In nature, ethylene is produced throughout the life of plants as a hormone to stimulate the ripening of fruits, opening of flowers, and abscission of leaves [103,110]. Many physical changes in the appearances of fruits and vegetables are caused by ethylene, thereby degrading the quality of agricultural commodities during storage and transportation [104].

Table 1. The gas composition, flow rate and VOC initial concentration

VOC/ Treatment method	VOC/Background gas		Gas flow rate (L min^{-1})		VOC concentration (ppm)
Acetone/ Continuous treatment	Acetone/Air		2.0		300
Acetone/ Cyclic treatment	Adsorption	Oxidation	Adsorption	Oxidation	300
	Acetone/N$_2$	Pure O$_2$	2.0	2.0	
DEE/ Continuous treatment	DEE/Air		1.0		150
Ethylene/ Cyclic treatment with impregnated zeolite	adsorption	oxidation	adsorption	oxidation	270 and 650
	Ethylene/Air	Pure air	1.0 and 2.0	1.0 and 2.0	
Ethylene/ Cyclic treatment with ion exchanged zeolite	adsorption	oxidation	adsorption	oxidation	200
	Ethylene/Air	Pure air	1.0	1.0	

The VOC contaminated gas streams were prepared by mixing the gaseous VOCs with synthetic air (79 % N$_2$ and 21 % O$_2$, by volume) or nitrogen (N$_2$) before being fed to the experimental reactor system (see in the next section). The VOC initial concentrations and gas flow rates (at 25 ^{o}C and 1.0 atm) were controlled by mass flow controllers (MFC) and shown in Table 1. For information, 1 ppm is tantamount to a molar concentration of 0.0408 μmol L^{-1}.

For continuous treatment of VOCs, the contaminated gas stream was continuously introduced into the reactor with plasma turned on. Meanwhile, for cyclic treatment, dilute VOCs were first adsorbed on adsorbent/catalyst without plasma for a certain period of time. After that,

the gas stream was switched from VOC-contaminated gas to either pure oxygen or pure synthetic air and plasma was ignited soon afterwards.

2.2. Experimental setup

2.2.1. General experimental setup

The schematic diagram of experimental setup is shown in Fig. 5. Generally, the DBD reactor consisted of a dielectric quartz tube wrapped outside with a grounded aluminum foil, and a high voltage (HV) electrode was coaxially inserted into the quartz tube. More details about the reactor parameters are summarized in Table 2.
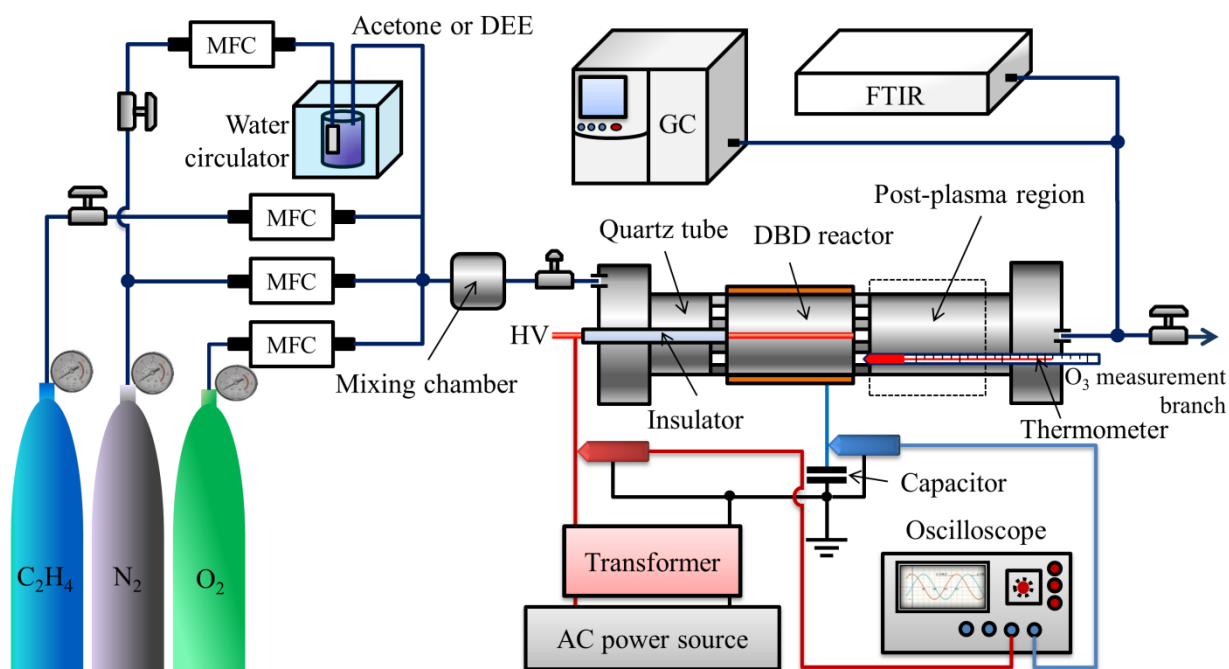
Figure 5. Experimental setup.

An alternating current (AC) power source was used to ignite plasma at a fixed frequency of 400 Hz. The DBD reactor was filled with different catalysts to construct the hybrid plasma-catalysis systems, depending on specific experiments. The preparation and amount of catalysts used will be presented in section 2.4.

Table 2. Parameters of DBD reactor.

VOC/ Treatment method	Dielectric		Discharge length (mm)	HV electrode	
	ID (mm)	Thickness (mm)		Material	OD (mm)
Acetone/ Continuous treatment	30	2	100	Stainless steel	4
Acetone/ Cyclic treatment	26	2	50	Stainless steel	6
DEE/ Continuous treatment	26	2	70	Copper	1
Ethylene/ Cyclic treatment with impregnated zeolite catalyst	26	2	100	Stainless steel	6
Ethylene/ Cyclic treatment with ion exchanged zeolite catalyst	26	2	50 and 100	Stainless steel	6

2.2.2. The plasma-catalysis reactor for continuous treatment of acetone

As seen from Fig. 6(a), two monolithic ceramic-supported catalysts (diameter: 29.5 mm; length: 150 mm each) having nineteen 4 mm–holes were placed in series inside the quartz tube.
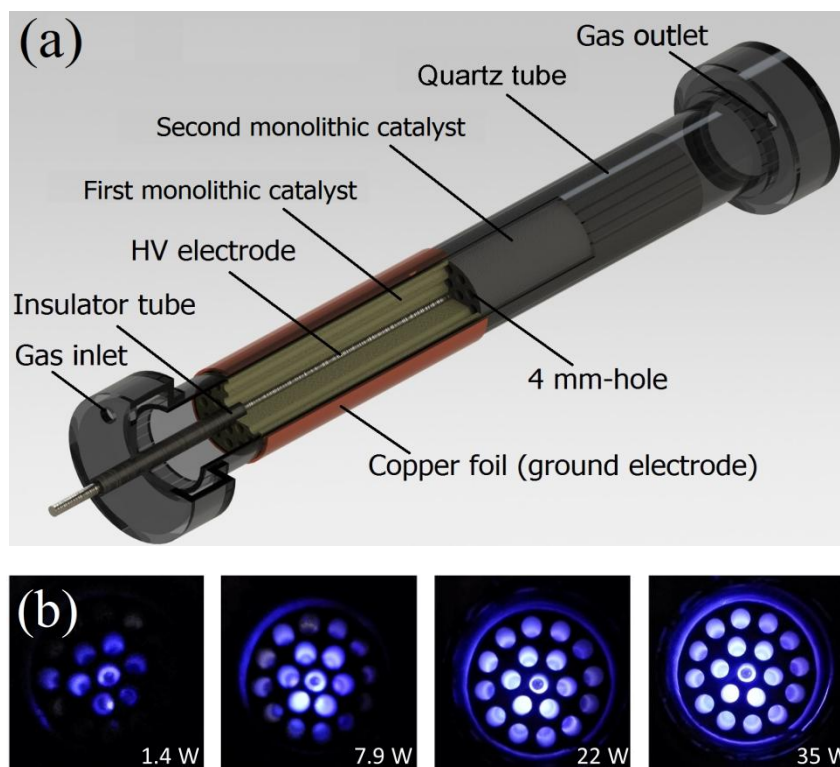
Figure 6. Cutaway view of plasma-catalysis reactor for continuous treatment of acetone (a) and plasma generation within the alumina monolith (b).

The HV electrode was coaxially inserted into the first monolithic catalyst loaded with ZnO (0.1 wt% Zn) or MnO_2 (0.1 wt% Mn). By which, the first catalyst was directly exposed to the plasma discharge. The aim of using the plasma-in-catalyst configuration was to investigate the combined effect of the plasma-catalysis on the decomposition of acetone. It can be seen from Fig. 6(b), the electrical discharge gradually spread out over the cross-section of the monolith by increasing the discharge power. The second monolithic catalyst was loaded with MnO_2 (5.0 wt% Mn), which was placed in the post-plasma region in order to further improve the acetone

22

decomposition by dissociating residual ozone to produce more reactive oxygen radical. For the sake of comparison, some experiments were carried out with the bare monoliths, which may clearly differentiate the catalytic effect from the plasma effect on the decomposition of acetone.

2.2.3. The plasma-catalysis reactor for continuous treatment of DEE

For DEE removal test, a one-stage reactor was constructed by placing different cordierite honeycomb supported catalysts including Mn, Fe and mixed Mn-Fe oxides directly in the discharge region of the DBD reactor (Fig. 7(a)).
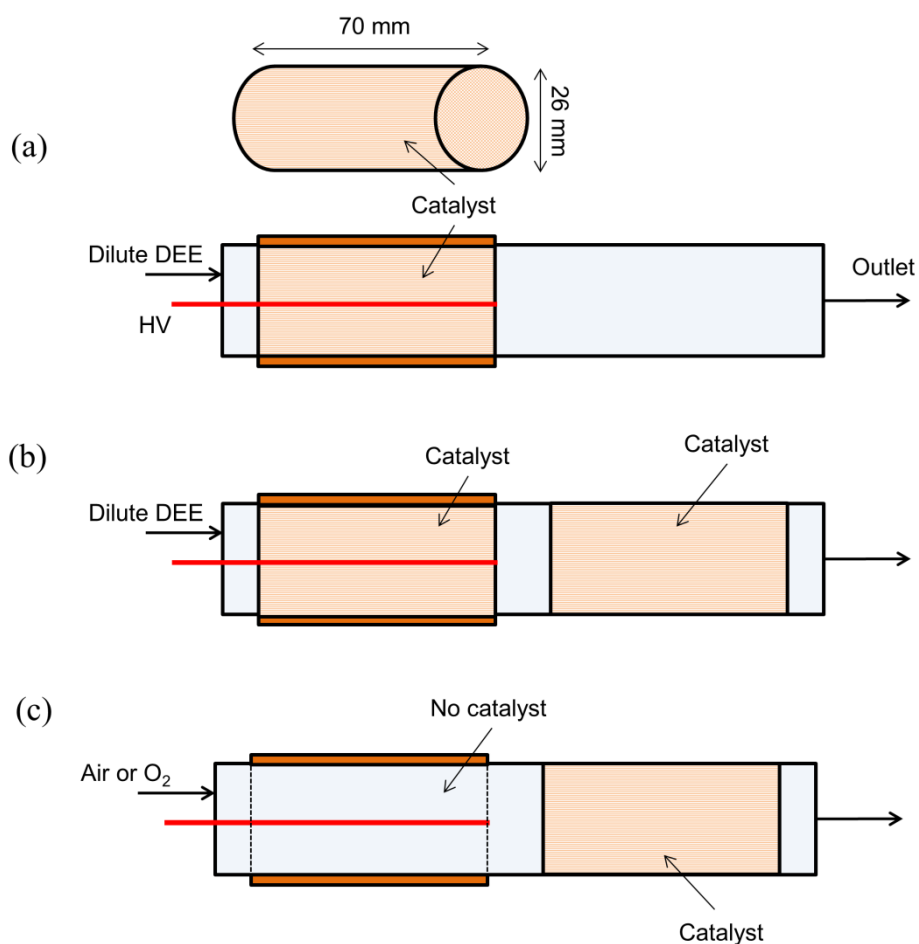
Figure 7. Plasma-catalysis reactor for continuous treatment of DEE.

To examine the catalytic activity for ozone decomposition, the investigated monolithic catalysts were placed downstream the blank DBD reactor (Fig. 7(b)). By which, ozone was first generated in the plasma reactor with either air or oxygen stream and subsequently decomposed in the catalyst bed at room temperature and a gas flow rate of 1.0 L min^{-1}. The ozone concentration was kept at 300 ppm for the both cases.

Similar to the continuous treatment of acetone, in order to archive higher performance in terms of DEE decomposition and energy efficiencies, an ozone decomposition catalyst was additionally placed in the post-plasma region (Fig. 7(c)). By which, residual ozone in plasma effluent was catalytically dissociated to give active atomic oxygen which, in turn, decomposed remaining DEE and further oxidized intermediate species.

2.2.4. The adsorption/plasma-catalysis reactor for cyclic treatment of acetone

The uses of alumina monolith and cordierite honeycomb result in a low pressure drop; however, their multi-channels and low specific surface areas make them impossible to be used as the VOC adsorbents. Meanwhile, zeolite with micro-porous structure and large specific surface area can be utilized as adsorbent for cyclic treatment of VOCs.

The removal of dilute acetone through consecutive adsorption and plasma-catalytic oxidation (i.e., cyclic process) was performed in a DBD reactor fully packed with Ag nanoparticle coated β−zeolite as both adsorbent and catalyst. As shown in Fig. 8, one cycle of the treatment included an adsorption step (100 min) followed by a plasma-catalytic oxidation one (15 min). In the oxidation step, oxygen was used as the gaseous oxidizing agent instead of air in order to avoid the formation of nitrogen oxides.
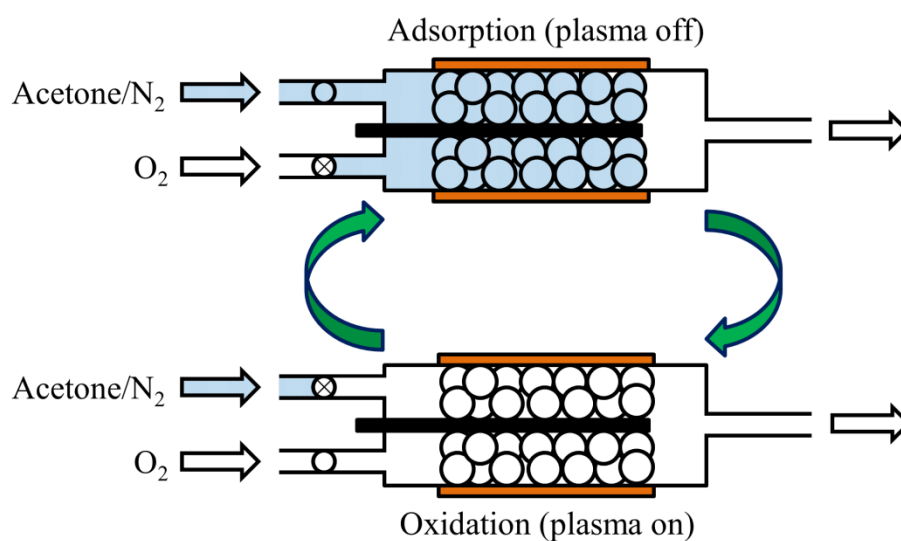
Figure 8. Adsorption/plasma-catalysis reactor for cyclic treatment of acetone.

For the sake of comparison, continuous plasma-catalytic treatment of acetone was also carried out in the same reactor with an initial acetone concentration of 300 ppm in air (flow rate: 2.0 L min^{-1}). The adsorption capacity for acetone was separately examined in a packed-bed column at 1000 ppm of acetone in N$_2$ gas (flow rate: 2.0 L min^{-1}).

2.2.5. The adsorption/plasma-catalysis reactor for cyclic treatment of ethylene using silver-based bimetallic impregnated 13X zeolite

Dynamic adsorption of dilute ethylene on silver and silver-based bimetallic impregnated zeolite and plasma-catalytic oxidation of the adsorbed ethylene were investigated using a packed-bed DBD reactor similar to that shown in Fig. 8, in which the discharge region was fully packed with Ag or Ag-M$_x$O$_y$ (M: Co, Cu, Mn, and Fe) impregnated 13X zeolite.

2.2.6. The adsorption/plasma-catalysis reactor with different configurations for cyclic treatment of ethylene using silver-exchanged 13X zeolite

To investigate the effects of reactor configuration and elucidate the roles of plasma induced active species, the cyclic treatment of ethylene was carried out in a reactor with three different configurations (i.e., one-stage, two-stage and hybrid), as shown in Fig. 9.
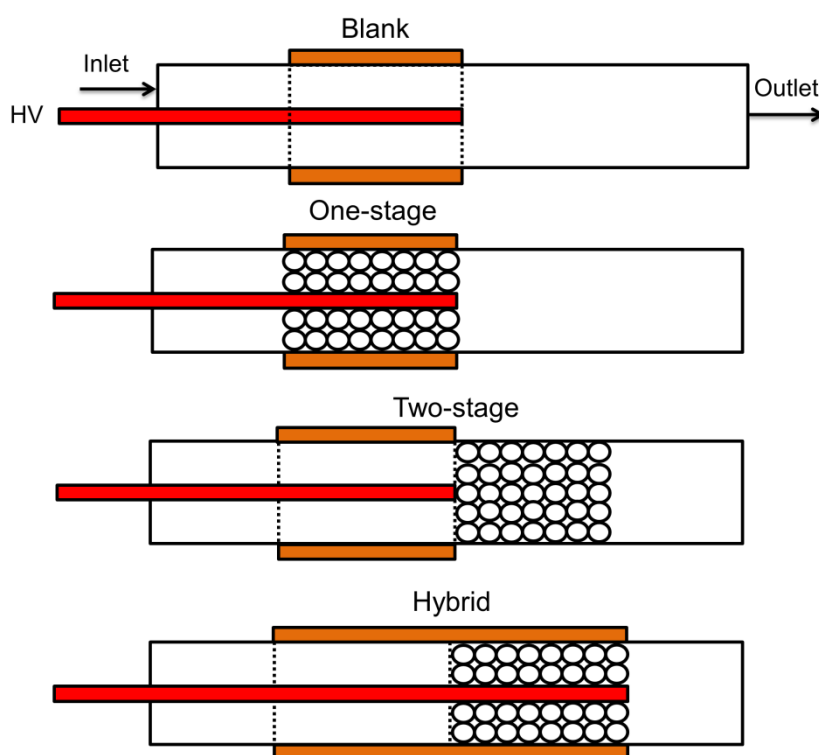
Figure 9. Adsorption/plasma-catalysis reactor for cyclic treatment of ethylene using silver-exchanged 13X zeolite.

In the one-stage configuration, the 50-mm long discharge region was fully packed with silver-exchanged 13X zeolite, while for the two-stage configuration, the same amount of the packing material was placed downstream the discharge region. The hybrid reactor was

combination of the one- and two-stage reactors, resulting in a 100-mm long discharge region in which the first half was left blank and the second half was filled with the adsorbent/catalyst.

2.3. Measurement methods

2.3.1. Electrical and temperature measurement

The high voltage applied to the reactor was recorded by a digital oscilloscope (Tektronix DPO3034) via a high voltage probe with an attenuation ratio of 1000:1 (Tektronix P6015A). Charge dissipated in the plasma reactor was measured by measuring the voltage across the capacitor (capacitance: 0.1 µF) connected to the reactor in series using a 10:1 voltage probe (Tektronix P6139B). The discharge power was determined from voltage-charge Lissajous figure.

For continuous treatment of VOCs, the specific input energy (SIE) was calculated by:

$$\text{SIE (J L}^{-1}) = \frac{60P}{Q} \qquad \text{(E 1)}$$

where P is the discharge power in W, Q is the gas flow rate in L min^{-1}, and 60 is the conversion factor from minutes to seconds. The SIE was varied by changing the applied voltage.

In plasma-catalysis process, the gas temperature (i.e., reactor temperature) may not sufficient for catalyst activation, but it can negatively affect the formation of ozone, especially in presence of catalyst. For *in-situ* measurement of the reactor temperature, an ethanol thermometer was placed 5 mm downstream from the discharge region.

2.3.2. Concentration measurement of gaseous species

The concentration of VOCs before and after the reactor was monitored by a gas chromatograph (GC, Bruker 450-GC) equipped with a flame ionization detector (FID) and a 60 m x 0.32 mm BR-624ms capillary column. A Fourier–transform infrared (FTIR) spectrometer

(Bruker IFS 66/S) with a 21-cm long gas cell was used to identify and measure the concentrations of gaseous products at the reactor outlet. The intensity of infrared absorbance at a characteristic wavenumber for a certain compound is proportional to its concentration. The FTIR was calibrated for VOCs, CO and CO_2 with known concentrations. For the quantification of other byproducts identified, they were assigned in the spectra, and the measured absorbance was converted into concentration using standard compilations [111]. All samples were collected at a resolution of 0.5 cm^{-1} with 10 scans. The concentration of ozone was measured using a portable gas analyzer (PortaSens II, Analytical Technology, Inc.). For the continuous treatment, the VOC decomposition efficiency is then calculated by:

$$\eta = \frac{[VOC]_{in} - [VOC]_{out}}{[VOC]_{in}} \times 100\%$$

(E 2)

where $[VOC]_{in}$ and $[VOC]_{out}$ are the inlet and outlet VOC concentrations, respectively.

For the cyclic treatment, the energy yield (Y) was defined as follows:

$$Y (J\,\mu mol^{-1}) = \frac{T \times P}{A} \times 60$$

(E 3)

where T is the plasma-catalytic oxidation time in min, P is the discharge power in W, A is the total amount of VOC adsorbed in μmol.

The average CO_2 generation rate (R_{CO_2}) was calculated by following equation:

$$R_{CO_2} (mL\,min^{-1}) = \frac{Q \int_0^T C_{CO_2} \times 10^{-6}}{T} \times 1000$$

(E 4)

where C_{CO_2} is the concentration of CO_2 in ppm, Q is the gas flow rate in L min^{-1}, and 1000 is the conversion factor from liters to milliliters.

The CO_2 selectivity (S_{CO_2}) was defined as:

28

$$S_{CO_2} = \frac{n_{CO_2}}{\sum\limits_{i=1}^{n} a_i \times n_i^{other}}$$

(E 5)

where n_{CO_2} and n_i^{other} are the amounts of CO_2 and any carbon-containing byproduct other than CO_2, respectively, a_i is the number of carbon atoms contained in any carbon-containing byproduct molecule, and n is the number of carbon-containing byproducts except CO_2.

The contribution of an individual carbon-containing product (A) detected at the outlet of the reactor to the carbon balance was evaluated as the percentage ratio of the atomic carbon contained in the product A (C_A) to the atomic carbon in the adsorbed VOC (C_{tot}):

$$\%C_A = \frac{C_A}{C_{tot}} \times 100$$

(E 6)

The mineralization efficiency is defined as the fraction of the adsorbed VOC oxidized to carbon dioxide which corresponds to the contribution of CO_2 to the carbon balance.

The energy efficiency was defined by the mass of VOC removed (g) per electrical energy input (kW h).

2.4. Catalyst preparation

2.4.1. Preparation of ceramic supported catalysts for continuous treatment of acetone

The ceramic membrane used for supporting catalysts consisted mainly of alumina, and its Brunauer-Emmett-Teller surface area, average pore size, and pore volume were measured to be 2.1 m^2g^{-1}, 1.2 µm and 0.135 cm^3g^{-1}, respectively. The supported catalysts including ZnO (0.1 wt% Zn) and MnO_2 (0.1 and 5.0 wt% Mn) were prepared using an incipient wetness impregnation method [90]. After impregnating the ceramic membrane with respective aqueous acetate ($Zn(CH_3CO_2)_2$, Sigma-Aldrich, for ZnO) and nitrate ($Mn(NO_3)_2.6H_2O$, Sigma-Aldrich,

for MnO$_2$) solution, it was dried overnight at 110 ℃ in a dry oven, and then calcination was performed in air atmosphere at 550 ℃ for 5 h, thereby forming the corresponding metal oxides.

2.4.2. Preparation of cordierite supported catalysts for continuous treatment of DEE

The cordierite honeycomb in cylindrical shape (diameter: 26 mm, length: 70 mm) was cut from a commercial cordierite monolith (diameter: 144 mm, high: 152 mm, 400 cells per square inch). Different catalysts including Mn, Fe and Mn-Fe mixed oxides were prepared by a dip-coating method using Mn(NO$_3$)$_2$.6H$_2$O (Junsei Chemical) and Fe(NO$_3$)$_3$.9H$_2$O (Daejung Chemicals & Metals) as metal precursors.

For preparation of the Mn-Fe catalyst, a mixture of the two nitrates was used. The cordierite support was dipped into the respective aqueous nitrate solution at room temperature and then dried overnight in the dry oven at 110 $^{\circ}$C before calcined at 500 $^{\circ}$C for 3 h. The dipping step was repeated several times before calcination.

Finally, cordierite supported Mn (1.7 wt%), Fe (1.6 wt%) and Mn-Fe (1.5-1.5 wt%) catalysts, denoted as Mn/cordierite, Fe/cordierite and Mn-Fe/cordierite, respectively, were obtained. The contents of active components were estimated from amounts of solutions adsorbed on cordierite supports.

2.4.3. Preparation of adsorbent/catalysts for cyclic treatment of acetone

The catalyst support was β-zeolite pellets (diameter: 3 mm; Si/Al molar ratio: 130; Brunauer–Emmett–Teller (BET) specific surface area: 550~600 m^2 g^{-1}) purchased from Cosmo Fine Chemicals. Silver nanoparticles were dispersed onto the zeolite pellets by using ultra-sonication for 30 min in the presence of water, which was then dried in the dry oven at 100 $^{\circ}$C

for several hours to obtain zeolite-supported Ag catalyst (3.0 wt%). The preparation of silver nanoparticles followed a procedure described elsewhere [112].

For treatment of acetone, the amount of Ag-coated β-zeolite packed in the reactor was 15 g. The acetone adsorption capacity was separately measured with 30 g of adsorbent (acetone initial concentration: 1000 ppm).

2.4.4. Preparation of adsorbent/catalysts for cyclic treatment of ethylene

2.4.4.1. Preparation of silver-based impregnated 13X zeolite:

Commercial 13X pelleted zeolite (diameter: 4.2 mm, Cosmo Fine Chemicals) was modified with Ag and Ag-M_xO_y (M: Co, Cu, Mn, and Fe) by the incipient wetness impregnation method. An appropriate amount of respective metal nitrate was dissolved in the deionized water (20 mL of water for 40 g of zeolite) under stirring condition for 30 min in dark. For preparation of a bimetallic adsorbent/catalyst, a mixture of silver nitrate and the nitrate of each corresponding metal was used. The prepared solution was added dropwise onto the zeolite pellets. Then, the impregnated zeolite was dried overnight in the dry oven at 110 ^{o}C before calcined at 500 ^{o}C for 5 h in ambient air. For convenience, the adsorbent/catalysts were named as Ag(a%)/13X and Ag-M(b-c%)/13X, such as Ag(1.0%)/13X and Ag-Co(1.0-0.7%)/13X, in which a, b, and c stand for the weight percentages of the corresponding metals. The reactor was packed with 29 g of each adsorbent/catalyst, unless otherwise mentioned.

2.4.4.2. Preparation of silver-exchanged 13X zeolite:

In this part, the parent 13X zeolite was exchanged with an aqueous solution of silver nitrate (0.02 M) at 80 ^{o}C for 4 h under vigorous stirring condition. The Ag-exchanged 13X was then filtered, washed several times with deionized water, then dried overnight in the dry oven at

110 ^{o}C and finally calcined at 500 ^{o}C for 3 h in ambient air. The content of Ag in zeolite was determined to be *ca*. 3.0 wt% using inductively coupled plasma optical emission spectrometry (Agilent Technologies, 700 series ICP-OES). For comparison purpose, the parent 13X zeolite was also modified by the incipient wetness impregnation method with the same amount of Ag loading (3.0 wt%). These prepared adsorbent/catalysts were denoted as Ag-EX/13X and Ag-IM/13X, respectively.

Each Ag-modified zeolite with a weight of 30 g was packed into a quartz tube (inner diameter: 26 mm) for measuring the ethylene adsorption capacity. Meanwhile, 15 g of Ag-EX/13X was used with the three different plasma/catalysis reactor configurations (described in the previous section) for the cyclic adsorption/oxidation test.

2.5. Catalyst characterization

The prepared catalysts were ground into fine powder and their X-ray diffraction (XRD) was performed on a diffractometer system (D/MAX2200H, Bede 200, Rigagu instruments) equipped with Cu K$_{\alpha}$ radiation (40 kV, 40 mA).

The powdered catalysts were well mixed with potassium bromide (KBr) and pressed into disks for the FTIR analysis using a FTIR spectroscopy (NICOLET 6700).

The morphology of catalysts and dispersion of active components were characterized by a field emission scanning electron microscope (FE-SEM, JEOL JSM-6700F) and a field emission transmission electron microscope (FE-TEM, JEOL JEM-2100F).

The surface chemistry of the supported catalysts was characterized by an X-ray photoelectron spectroscopy (XPS, Theta Probe AR-XPS System, Thermo Fisher Scientific) with monochromatic Al K$_{\alpha}$ radiation (1486.6 eV) operated at 15 kV and 150 W X-ray excitation sources. The binding energies were calculated with reference to C1s peak (284.6 eV).

The Brunauer-Emmett-Teller (BET) surface areas of the catalysts were measured by N_2 adsorption at 77 K using a surface area analyzer (TriStar II 3020, Micromeritics).

In addition, the content of active component in the ion-exchanged zeolite was determined using an inductively coupled plasma optical emission spectrometry (ICP, Agilent Technologies, 700 series ICP-OES).

CHAPTER 3: RESULTS AND DISCUSSION

3.1. Continuous plasma-catalytic treatment of acetone in annular porous monolithic ceramic-supported catalysts

Redrafted from:

Quang Hung Trinh and Young Sun Mok, Chemical Engineering Journal 251 (2014) 199–206

3.1.1. SEM characterization of the catalysts
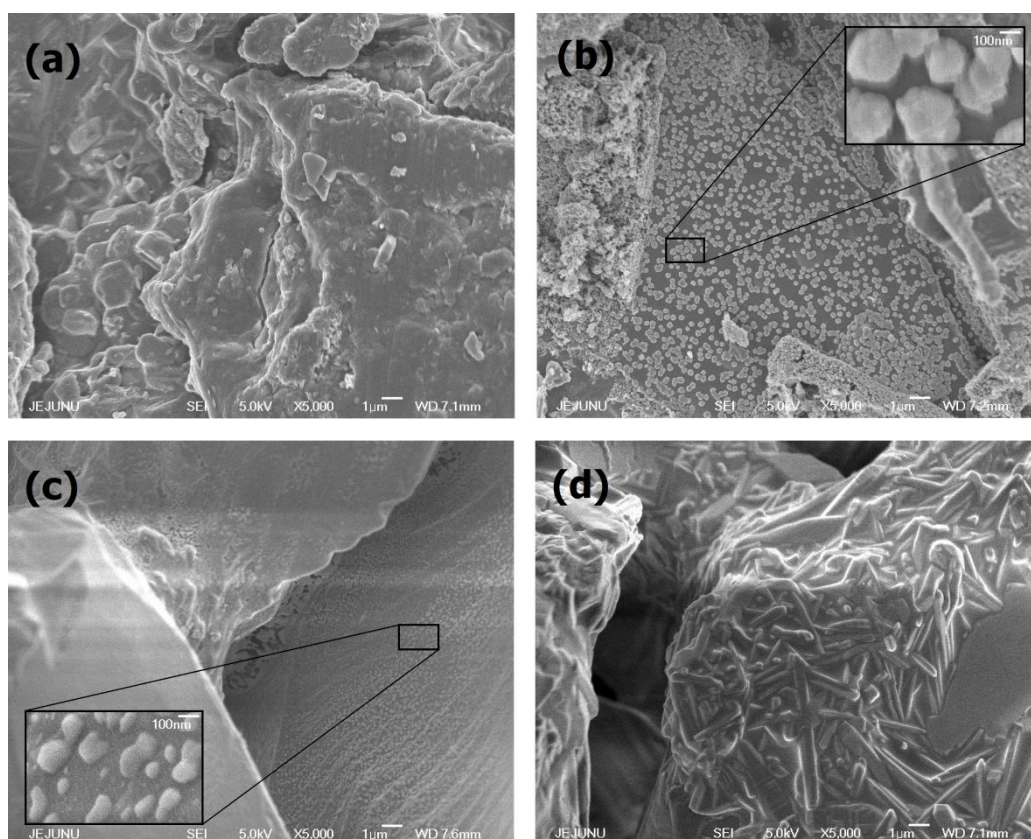
Figure 10. SEM images of bare ceramic support (a), ZnO-loaded (0.1 wt% Zn) (b), MnO$_2$–loaded (0.1 wt% Mn) (c) and MnO$_2$–loaded (5.0 wt% Mn) (d).

Figure 10 shows the SEM images of ceramic supports with and without catalyst loading. As can be seen from Fig. 10(a), the bare ceramic support showed a smooth and clean surface. In

Fig. 10(b) and (c), the ZnO and MnO_2 nanoparticles that were uniformly dispersed on the surface could be clearly distinguished from the ceramic support. The insets of Fig. 10(b) and (c) tell that the mean sizes of the MnO_2 and ZnO nanoparticles were approximately 100 and 200 nm, respectively. With higher loading (5.0 wt% Mn), the shape of the active component changed to nanorod, as shown in Fig. 10 (d).

3.1.2. Acetone decomposition efficiency

Fig. 11 shows the plasma-catalytic decomposition efficiency of acetone as a function of SIE for different catalyst arrangements listed in Table 3.
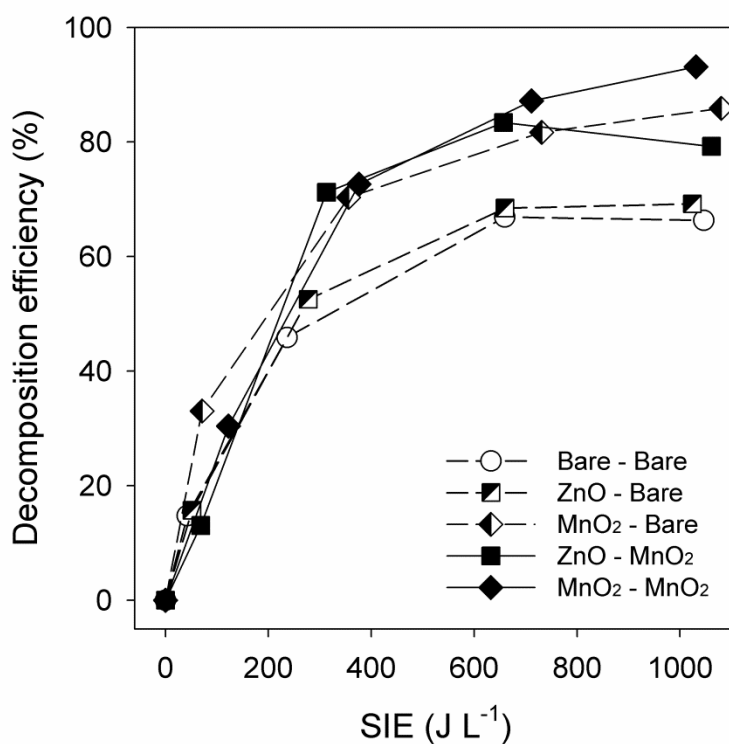
Figure 11. Acetone decomposition efficiency for different catalyst arrangements.

Table 3. Catalyst arrangements in the plasma-catalysis reactor.

Configuration	First monolith	Second monolith
Bare–bare	Without catalyst loading	Without catalyst loading
ZnO–bare	Coated with ZnO (0.1 wt% Zn)	Ditto
MnO_2–bare	Coated with MnO_2 (0.1 wt% Mn)	Ditto
ZnO–MnO_2	Coated with ZnO (0.1 wt% Zn)	Coated with MnO_2 (5.0 wt% Mn)
MnO_2–MnO_2	Coated with MnO_2 (0.1 wt% Mn)	Ditto

The acetone decomposition efficiency for the bare–bare arrangement gradually increased with increasing the SIE and then saturated at about 67 %. The use of the ZnO-bare arrangement only slightly improved the acetone decomposition efficiency, which reveals that the photo-catalytic activity of ZnO for the decomposition of acetone was not significant under the influence of non-thermal plasma. On the other hand, the MnO_2-bare arrangement exhibited a noticeable enhancement in the decomposition efficiency. As can be seen, the acetone decomposition efficiency kept on increasing with increasing the SIE, reaching 82 % at a SIE of 731 J L^{-1}. Further increase in the SIE up to 1080 J L^{-1} led to just a slight increment in the decomposition efficiency.

The performances for the tandem arrangements of the catalysts were evaluated by loading MnO_2 (5.0 wt% Mn) on the second monolithic ceramic support. As shown in Fig. 11, the MnO_2–MnO_2 arrangement showed better decomposition performance than the MnO_2-bare case. In detail, the MnO_2–MnO_2 arrangement decomposed about 87 % and 93 % of acetone at 711 and 1031 J L^{-1}, respectively. The difference in the decomposition efficiency between the MnO_2–MnO_2 and the MnO_2–bare arrangement reflects the amount of acetone decomposed in the post-plasma region. In the post–plasma region, long-lived reactive species, namely, ozone can be involved in the catalytic decomposition of acetone [65,113]. The dissociation of ozone

on MnO_2 produces oxygen atom that is a far stronger oxidant than ozone itself, which can account for the enhanced decomposition efficiency for the MnO_2–MnO_2 arrangement. It should be noted that the reactivity of ozone with acetone is extremely low and stronger oxidants other than ozone is needed. In this regard, the use of MnO_2 catalysts in the post-plasma region is advisable. Acetone is a stable compound, so that it does not break down easily. Recently, Zheng et al. [47] investigated the decomposition of acetone in a DBD reactor with different packing materials. They obtained maximum decomposition efficiency of 80 % (initial concentration: 100 ppm, gas flow rate: 200 mL min^{-1}) at 630 J L^{-1} using γ–Al_2O_3 packing material (specific surface area: 174 m^2 g^{-1}).
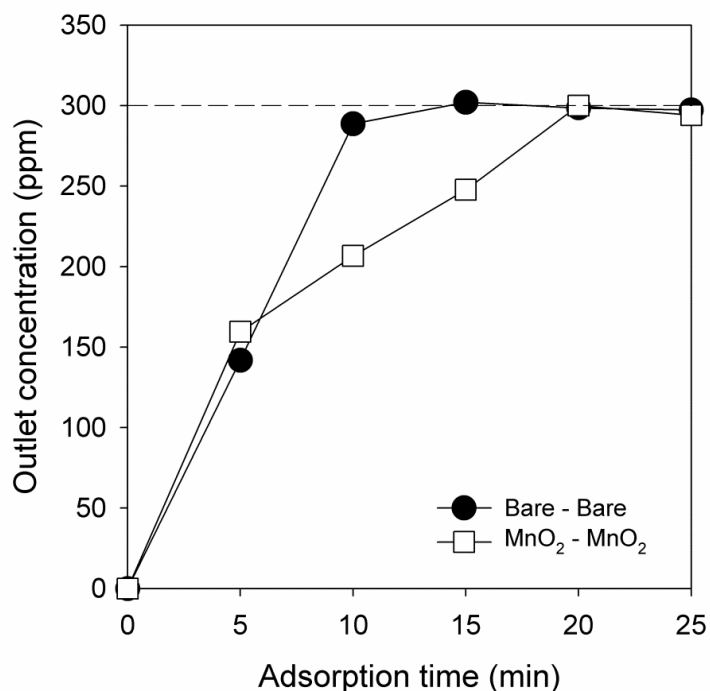
Figure 12. Acetone adsorption for bare-bare and MnO_2-MnO_2 arrangements.

In a plasma-catalytic decomposition process, the adsorption capability and therefore the surface area of packing material play important roles [114]. The specific surface area of the monolithic ceramic support (2.1 m^2 g^{-1}) is a lot smaller than that of γ–Al_2O_3. In view of the high initial

concentration (300 ppm) and the small specific surface area of the ceramic support used in this work, 87% decomposition efficiency at 711 J L^{-1} for the MnO_2–MnO_2 arrangement is noteworthy, which is ascribed to the aforementioned MnO_2 effect. For information, the adsorption breakthrough curves of the bare-bare and MnO_2-MnO_2 arrangements for acetone at a concentration of 300 ppm under room temperature are presented in Fig. 12. From this figure, the adsorption capacities of the bare-bare and MnO_2-MnO_2 arrangements for acetone were estimated to be 0.49 and 0.66 μmol g^{-1}, respectively. Even though the presence of MnO_2 slightly improved the acetone adsorption capability, the supported catalyst has a very low acetone adsorption capacity compared to highly porous alumina or zeolite pellets.

3.1.3. Ozone concentration

In order to get insight into the role of ozone in the decomposition of acetone, the concentration of ozone was measured downstream the reactor for the different catalyst arrangements listed in Table 3.

As shown in Fig. 13 (a), the concentration of O_3 increased steeply with increasing the SIE up to about 700 J L^{-1} and leveled off thereafter in all the catalyst arrangements examined. Electron-impact O_2 dissociation which ultimately affects the rate of ozone generation strongly depends on SIE and it is natural that the concentration of ozone should increase with increasing the SIE. The slight decrease in the ozone concentration above 700 J L^{-1} is obviously due to the dielectric heating of the monolithic ceramic. It is well known that the rate of ozone generation is inversely proportional to the temperature. The dependence of the reactor temperature measured downstream the plasma region on the SIE is shown in Fig. 13 (b). The *in-situ* temperature measurement showed that the reactor temperature increased with increasing the SIE, reaching 152 ^{o}C at about 1.0 kJ L^{-1} (Fig. 13 (b)). The increase of the reactor temperature must have speeded up the decomposition of ozone.
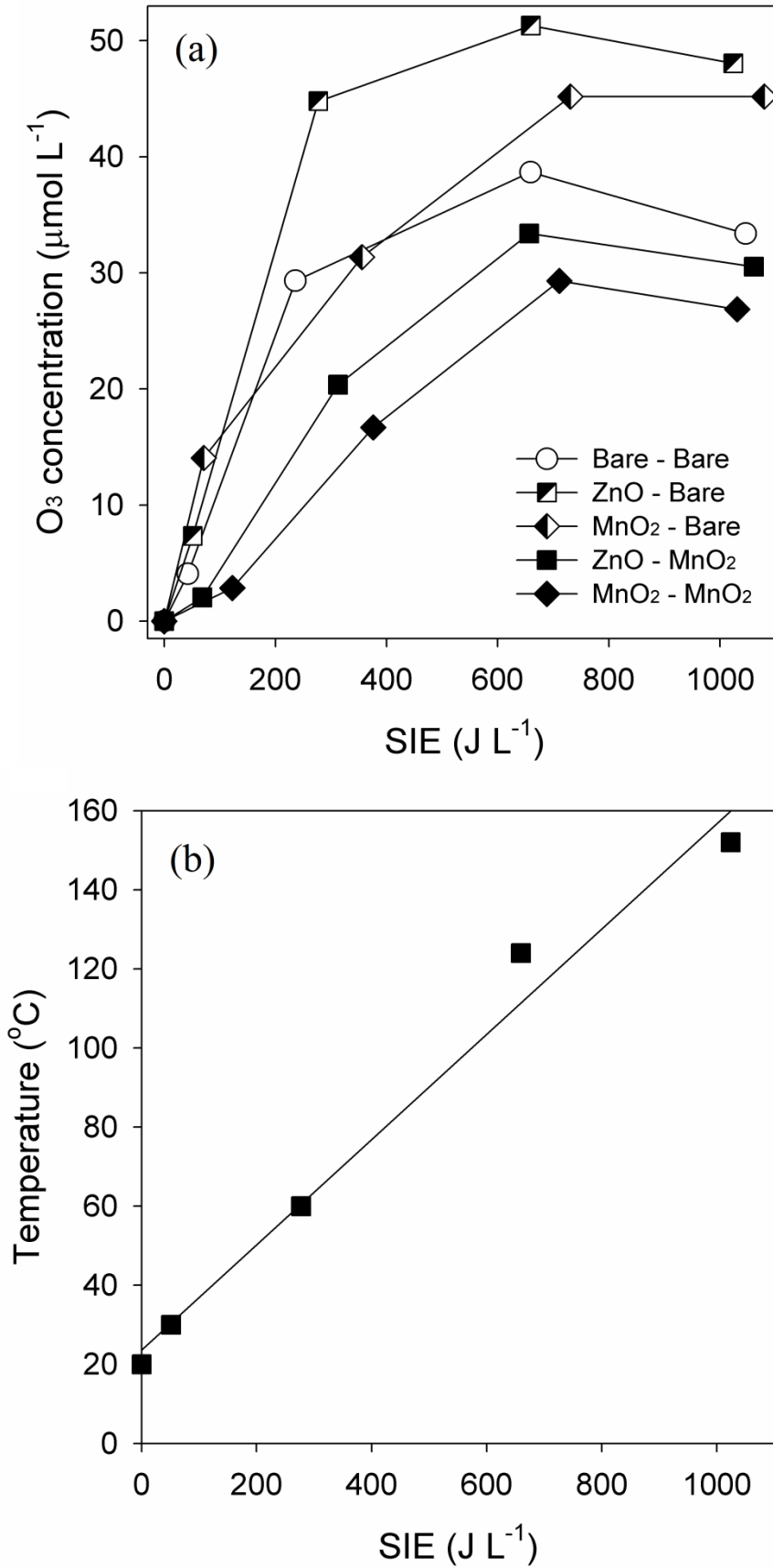
Figure 13. Ozone concentration for different catalyst arrangements (a), reactor temperature (b).

As seen in the Fig. 13(a), the concentration of ozone for the ZnO-bare arrangement was considerably higher than that for the MnO_2-bare arrangement. Moreover, the concentration of ozone was greatly reduced by using the MnO_2-loaded monolithic ceramic in the post-plasma region. As shown in Fig. 11, both the MnO_2–MnO_2 and ZnO-MnO_2 arrangements resulted in substantial enhancement in the decomposition efficiency, compared to the cases of MnO_2–bare and ZnO-bare. These observations indicate that ozone itself hardly oxidized acetone but the atomic oxygen created from ozone on MnO_2 catalyst contributed to the decomposition of acetone. The catalytic decomposition of ozone can be summarized by the following reactions [115]:

$$O_3 + * \rightarrow O* + O_2 \qquad (R\ 6)$$

$$O_3 + O* \rightarrow O_2* + O_2 \qquad (R\ 7)$$

$$O_2* \rightarrow O_2 + * \qquad (R\ 8)$$

where the symbol * stands for the active site on the catalyst surface. The active oxygen atoms generated by reaction (R 6) can effectively oxidize acetone in the post-plasma region. Meanwhile, the lower concentration of ozone for the bare-bare arrangement than the ZnO-bare and MnO_2-bare cases indicates that the catalyst can facilitate the formation of ozone when it is exposed to the plasma.

3.1.4. Product formation and decomposition pathway

Fig. 14 shows the FTIR spectra of the effluent before and after the plasma treatment at a SIE of 659 J L^{-1} for the bare-bare arrangement. The gaseous products identified by the FTIR included carbon oxides (CO and CO_2) and aldehydes (HCHO and CH_3CHO), among which carbon oxides were dominant. Regarding the decomposition of acetone, there are numerous reactions known in the literature [116].
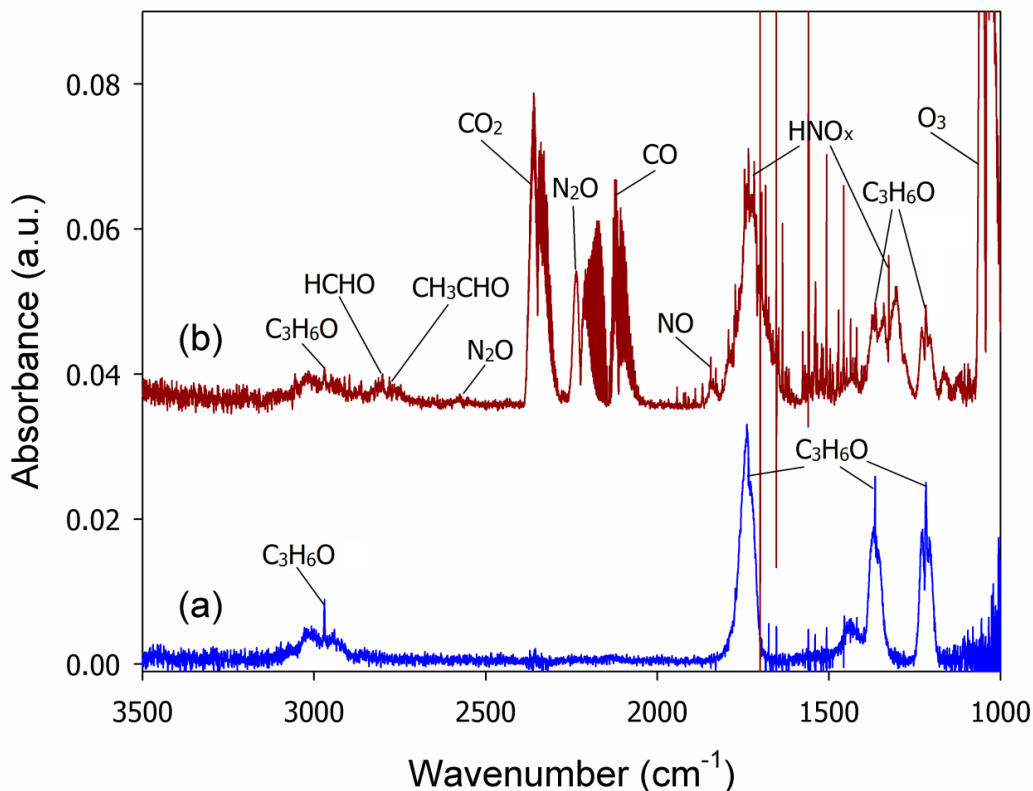
Figure 14. FTIR spectra of the effluent before (a) and during the plasma treatment (b) for the bare-bare arrangement (SIE: 659 J L^{-1}).

The reactions in Table 4 and Table 5 were chosen, based on the magnitude of rate constant. The reactions responsible for the decomposition of acetone are summarized in Table 4. All the rate constants are the values at 298 K [116]. First, the energetic electrons created by the electrical discharge collided with the gas molecules to produce reactive species such as $N_2^*(A^3\Sigma_u^+)$, $N_2^*(B^3\Pi_g)$, $O(^1D)$ and $O(^3P)$ [117]. Subsequently, these species and electrons dissociated acetone molecules into fragments (CH_3 and CH_3CO) by reaction (R 9). The recombination of CH_3CO (reaction (R 10)) and the partial oxidations of the fragments via several steps (reactions (R 11)-(R 19) and (R 24)) can explain the formation of CH_3CHO and HCHO. The carbon–containing intermediates were further oxidized to CO and CO_2 through reactions (R 20)–(R 31).

Table 4. Reactions responsible for the oxidative decomposition of acetone.

	Reaction	Rate constant at 298 K $(cm^3\ mol^{-1}\ s^{-1})$
(R 9)	$CH_3COCH_3 + energetic\ species\,(e^-,\ N_2(A^3\sum_u^+)) \rightarrow CH_3CO + CH_3$	
(R 10)	$2CH_3CO \rightarrow CH_3CHO + CH_2CO$	8.99×10^{12}
(R 11)	$CH_3CO + O \rightarrow CO_2 + CH_3$	9.64×10^{12}
(R 12)	$CH_3 + O \rightarrow CH_2O + H$	5.66×10^{13}
(R 13)	$CH_3 + O_2 \rightarrow CH_3O_2$	1.08×10^{12}
(R 14)	$CH_3 + O_3 \rightarrow CH_3O + O_2$	1.57×10^{12}
(R 15)	$CH_2CO + H \rightarrow CH_3 + CO$	3.47×10^{10}
(R 16)	$CH_3O_2 + O \rightarrow CH_3O + O_2$	2.59×10^{13}
(R 17)	$CH_3O + O \rightarrow CH_2O + OH$	6.03×10^{12}
(R 18)	$CH_3O + O_2 \rightarrow CH_2O + HO_2$	1.15×10^{9}
(R 19)	$CH_3O + OH \rightarrow CH_2O + H_2O$	1.81×10^{13}
(R 20)	$CH_3CHO + O \rightarrow CH_3CO + OH$	2.70×10^{11}
(R 21)	$CH_3CHO + OH \rightarrow CH_3CO + H_2O$	8.35×10^{12}
(R 22)	$CH_2O + O \rightarrow OH + HCO$	1.01×10^{11}
(R 23)	$CH_2O + OH \rightarrow H_2O + HCO$	6.03×10^{12}
(R 24)	$HCO + CH_3CO \rightarrow CH_3CHO + CO$	9.04×10^{12}
(R 25)	$HCO + O \rightarrow OH + CO$	3.01×10^{13}
(R 26)	$HCO + O \rightarrow CO_2 + H$	3.01×10^{13}
(R 27)	$HCO + O_2 \rightarrow CO + HO_2$	3.37×10^{12}
(R 28)	$HCO + O_3 \rightarrow H + CO_2 + O_2$	5.00×10^{11}
(R 29)	$HCO + OH \rightarrow H_2O + CO$	1.02×10^{14}
(R 30)	$CO + O \rightarrow CO_2$	3.88×10^{12}
(R 31)	$CO + O(^1D) \rightarrow CO_2$	4.82×10^{13}

Besides, several nitrogen–containing byproducts such as N_2O, NO and HNO_x were also observed in the FTIR spectrum. The reactions related to the formation of these byproducts are given in Table 5.

Table 5. Reactions leading to formation of nitrogen-containing byproducts.

	Reaction	Rate constant at 298 K ($cm^3 \, mol^{-1} \, s^{-1}$)
(R 32)	$N_2 + O(^1D) \rightarrow N_2O$	1.27×10^{11}
(R 33)	$N_2O + O(^1D) \rightarrow 2NO$	4.04×10^{13}
(R 34)	$N + O_2 \rightarrow NO + O$	5.12×10^7
(R 35)	$NO + O \rightarrow NO_2$	1.81×10^{13}
(R 36)	$NO + O_3 \rightarrow NO_2 + O_2$	1.13×10^{10}
(R 37)	$NO + OH \rightarrow HNO_2$	2.17×10^{13}
(R 38)	$NO + HO_2 \rightarrow NO_2 + OH$	5.73×10^{12}
(R 39)	$NO_2 + H \rightarrow NO + OH$	7.70×10^{13}
(R 40)	$NO_2 + O \rightarrow NO_3$	1.32×10^{13}
(R 41)	$NO_2 + OH \rightarrow HNO_3$	4.52×10^{13}
(R 42)	$NO_3 + HO_2 \rightarrow O_2 + HNO_3$	1.15×10^{12}
(R 43)	$NO_3 + CH_3O \rightarrow CH_2O + HNO_3$	9.11×10^{11}

The formation of N_2O can be interpreted by reaction (R 32), and reactions (R 37) and (R 41)–(R 43) led to the formation of nitrous and nitric acids (HNO_x). The trace of NO_2 could not be detected by the FTIR, suggesting that most of NO_2 generated has been converted into HNO_x. The formation of NO which appears as a weak absorption band in the spectrum can be explained by reactions (R 33) and (R 34).

Fig. 15 presents the concentrations of the carbon–containing products in the effluent for the bare-bare arrangement as a function of SIE. As seen, the concentrations of all products increased as the SIE was increased. Acetone was found to be oxidized primarily to CO of which

concentration rapidly increased with increasing the SIE up to 659 J L^{-1} and then slowed down. It is not surprising that CO is the main product, because O_2 is involved in reaction (R 27) responsible for the formation of CO. Note that the concentration of O_2 (20% by volume) is far higher than those of other plasma-induced reactive species leading to the formation of CO_2 (reactions (R 26) and (R 28)).
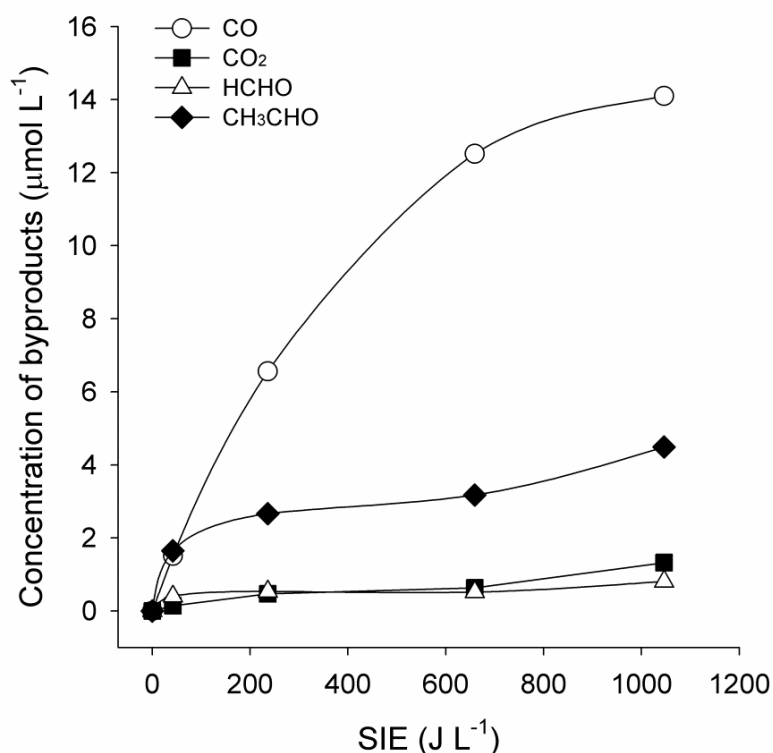
Figure 15. Concentrations of carbon-containing gaseous products for the bare-bare arrangement.

Fig. 16 shows the FTIR spectra of the effluent gases obtained with the MnO_2–MnO_2 and ZnO–MnO_2 arrangements. Both of the catalyst arrangements formed CO, CO_2, HCHO and CH_3CHO. In case of the MnO_2–MnO_2, however, more CO_2 was formed, and the trace of NO disappeared from the spectrum. The removal of NO can be explained in the same line as the enhanced acetone decomposition resulting from the dissociation of ozone on MnO_2. That is, the atomic oxygen formed by reaction (R 6) helps improve the oxidation of NO.
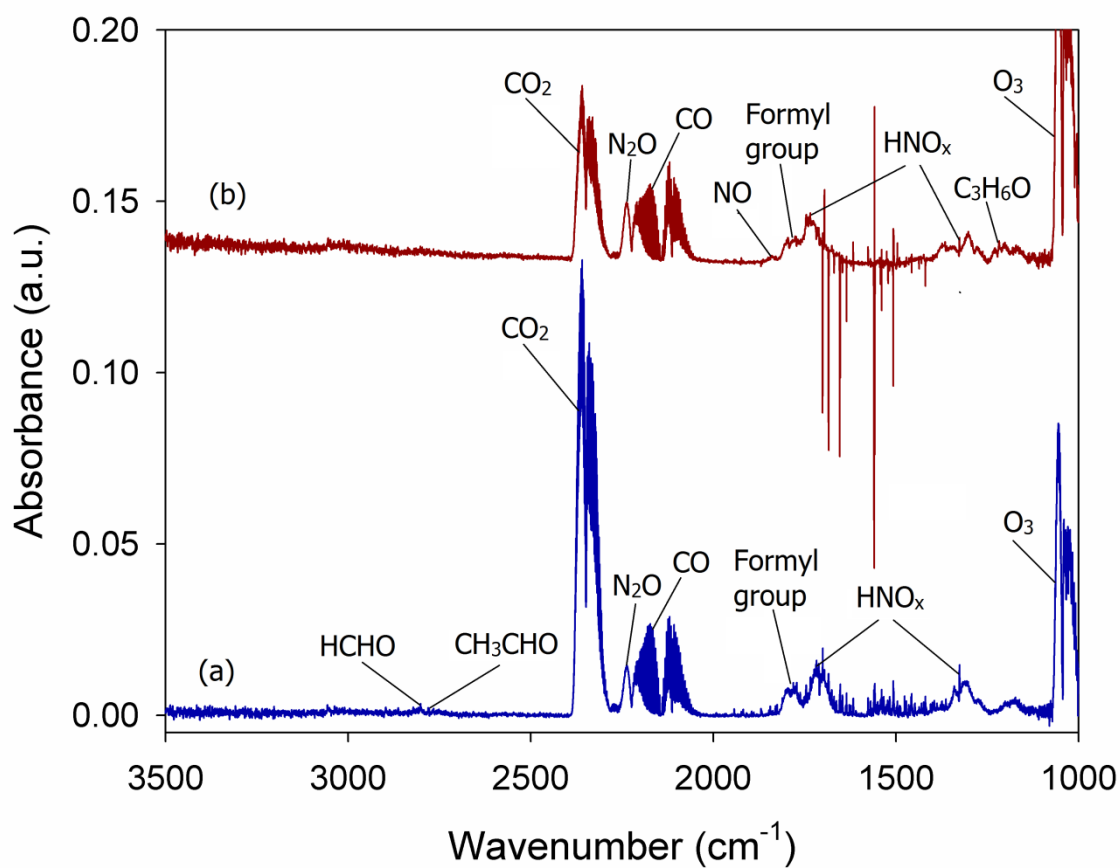
Figure 16. FTIR spectra of effluent gas obtained with MnO_2–MnO_2 arrangement at 711 J L^{-1} (a) and ZnO–MnO_2 arrangement at 657 J L^{-1} (b).

Fig. 17 presents the product concentrations obtained with the MnO_2–MnO_2 and ZnO–MnO_2 arrangements as functions of SIE. Similar to the observation with the bare–bare arrangement, the product concentrations of MnO_2–MnO_2 and ZnO–MnO_2 tended to increase with increasing the SIE. As expected from the enhanced acetone decomposition (Fig. 11), the MnO_2–MnO_2 arrangement produced more carbon-containing products than the ZnO–MnO_2 arrangement did.
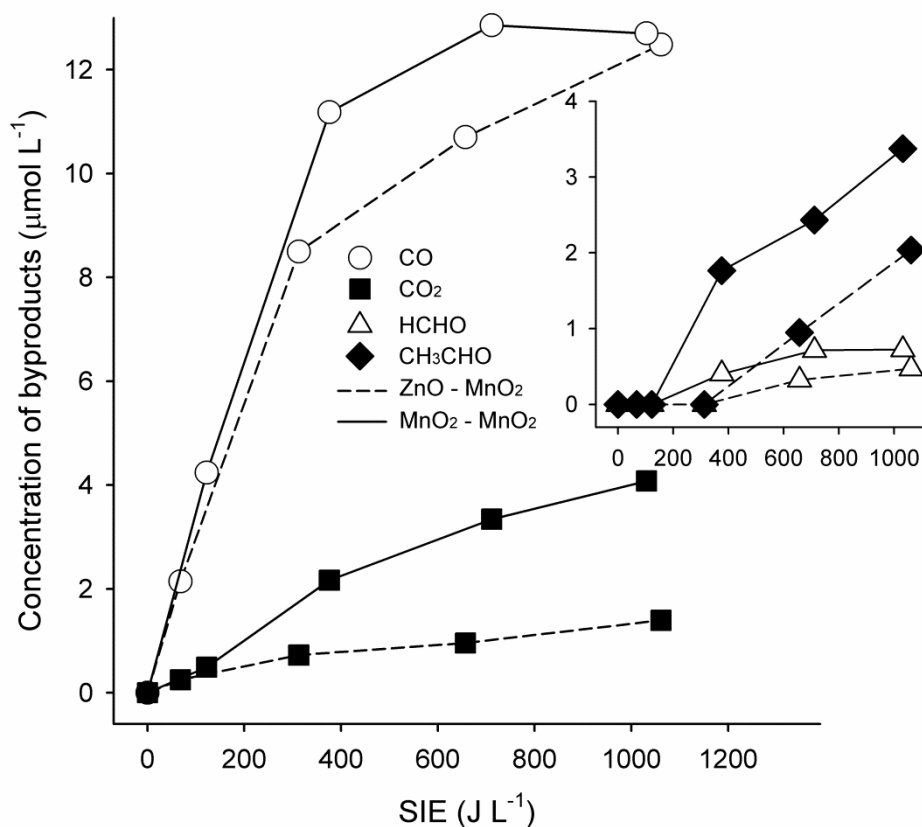
Figure 17. Concentrations of carbon-containing products obtained with MnO_2-MnO_2 and ZnO-MnO_2 arrangements.

Fig. 18 shows the cumulative carbon concentration as a function of SIE for the MnO_2–MnO_2 arrangement. The concentration of carbon atom corresponding to the initial concentration of acetone is 36.6 μmol L^{-1}. As can be seen, the increase in the SIE increased the carbon concentration accounting for the identified byproducts. However, the amount of the missing carbon also showed an increasing trend. The missing carbon resulting in poor carbon balance can be interpreted by the formation of low and nonvolatile organic compounds. Indeed, polymer-like deposit with brownish color was formed, which was accumulated on the inner wall as a result of repeated use of the reactor.
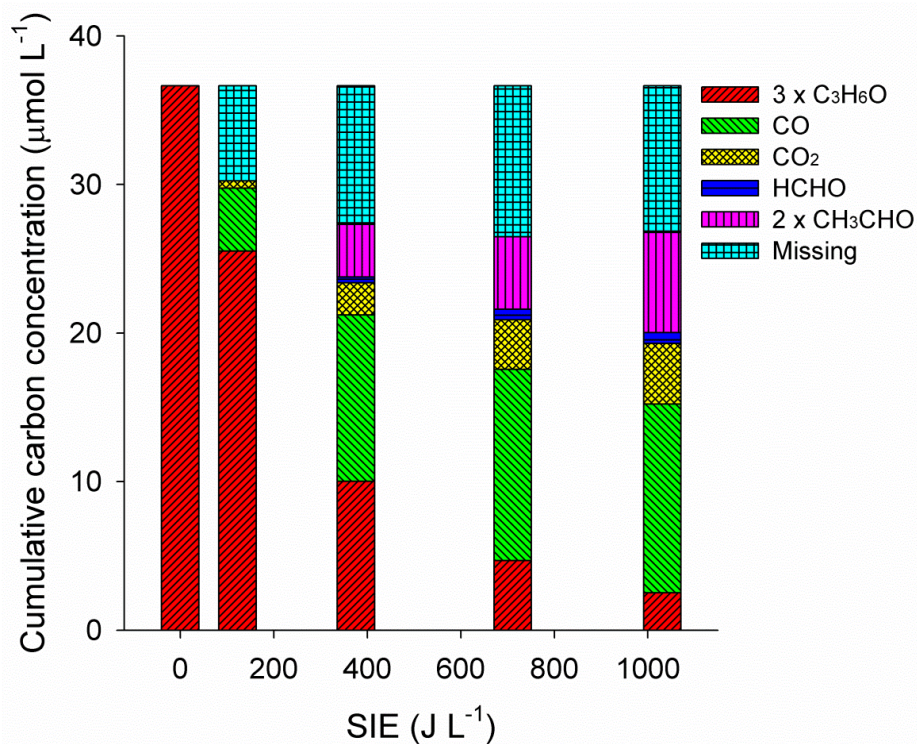
Figure 18. Distribution of carbon–containing gaseous products for MnO_2–MnO_2 arrangement.
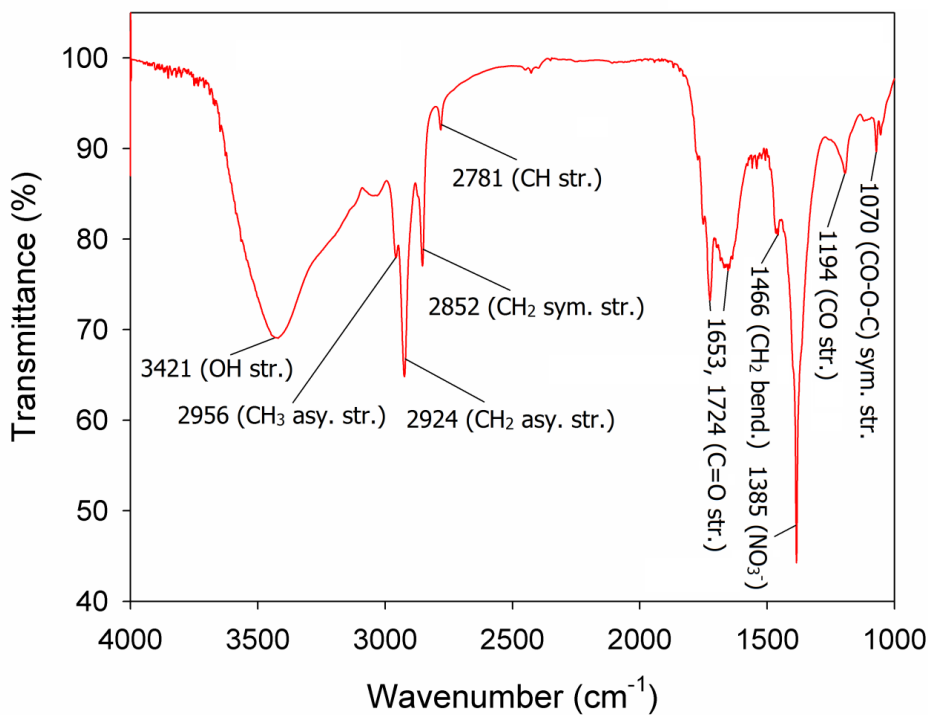
Figure 19. FTIR spectrum of polymer-like deposit collected from reactor inner wall.

The brownish polymer–like deposit on the reactor wall (the inner surface of the quartz tube in which the monolith is placed) was collected, well mixed with KBr powder, and then pelletized for FTIR characterization. The FTIR spectrum in Fig. 19 shows that the polymer–like deposit consists of methyl (CH_3), methylene (CH_2), and methine (CH) groups. The CH_3 group appears at a wavenumber of 2956 cm^{-1} by the asymmetric stretching vibration. The absorption bands peaking at 1466, 2852, 2924 cm^{-1} are due to the bending, symmetric and asymmetric stretching vibrations of CH_2, respectively, and the peak at 2781 cm^{-1} can be assigned to the CH stretching. The stretch bands of carbonyl group (C=O) are observed at 1653 and 1724 cm^{-1} [118,119]. In addition, the peaks at 1070 and 1194 cm^{-1} are indicative of the CO–O–C and C–O (of ester group) stretching vibrations [120,121]. The sharp intensive peak located at 1385 cm^{-1} is due to the presence of nitrate (NO_3^-), which confirms that HNO_3 was formed in the reactor [122].
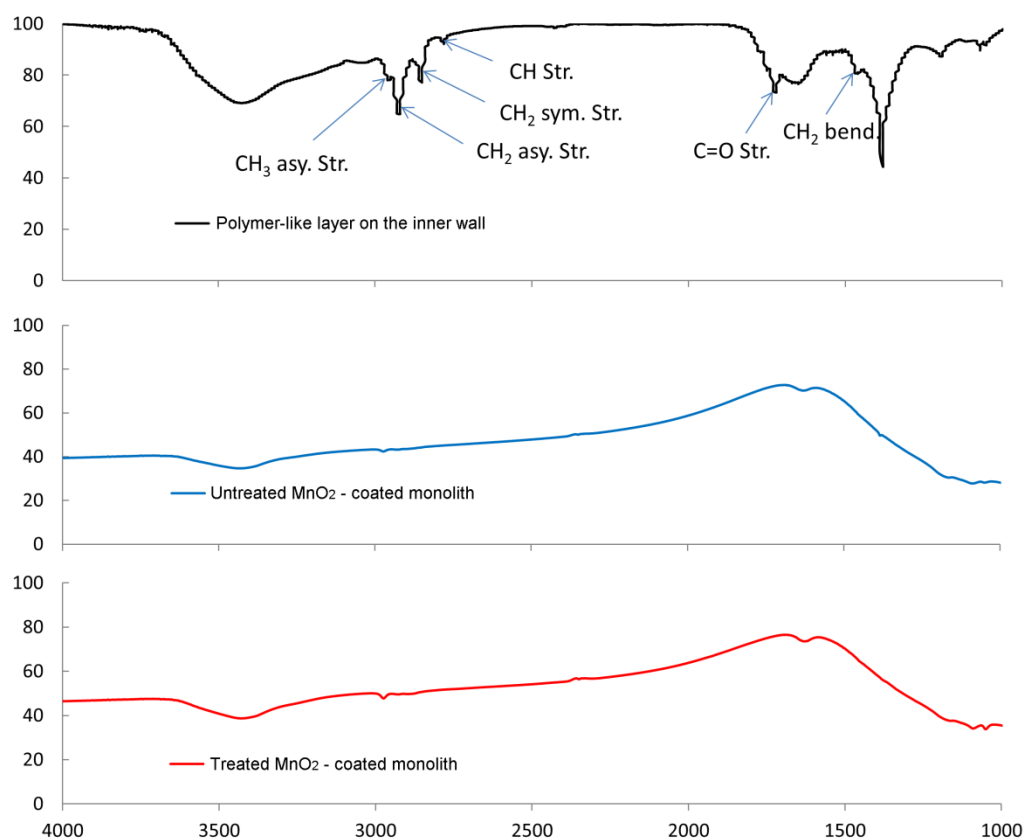
Figure 20. FTIR spectra of fresh and used MnO_2-coated monoliths.

The formation of polymer-like deposit on the MnO_2-coated monolith which was placed in the plasma region was also examined by FTIR. Figure 20 compares the FTIR spectrum of the MnO_2-coated monolith used for acetone treatment with that of fresh one. As shown, both spectra are quite similar to each other and the traces of organic compounds were under detectable levels. This observation suggests that the MnO_2-coated monolith effectively prevents the formation of polymer-like deposit as a result of enhanced oxidation capability.

To summarize, the oxidative decomposition of acetone over multichannel monolithic ceramic-supported catalysts combined with non-thermal plasma is investigated. The tandem plasma-catalytic reactor consisted of two ceramic-supported catalysts containing zinc oxide (ZnO) and/or manganese oxide (MnO_2), in which the first supported catalyst was exposed to the plasma discharge and the second one was placed in the post-plasma region. Several sets of catalyst arrangements such as MnO_2-loaded monolith followed by bare monolith, ZnO-loaded monolith followed by bare monolith, ZnO-loaded monolith followed by MnO_2-loaded monolith and two consecutive MnO_2-loaded monoliths with different Mn contents were examined in relation to the acetone decomposition and the product formation. More than 90 % of acetone is decomposed at a specific input energy (SIE) of about 1.0 kJ L^{-1} with the catalyst arrangement of MnO_2 (0.1 % Mn) followed by MnO_2 (5.0 % Mn), while the decomposition efficiency obtained with two consecutive bare monoliths was about 66 % at almost the same SIE. The use of ZnO in the plasma discharge region does not largely improve the acetone decomposition efficiency. Wherever it is placed either in the plasma discharge region or in the post-plasma region, MnO_2 catalyst substantially promotes the acetone decomposition, obviously due to the dissociation of ozone into far more reactive oxygen atoms available for oxidative transformation of acetone.

-----------------------o0o-----------------------

49

The question is whether the effects of the ozone decomposition catalyst in combination with NTP are the same for other VOCs, especially for those with high reactivity towards plasma-induced ozone. In such a case, ozone and ozone-induced atomic oxygen are both involved in the oxidation reactions. The plasma catalytic decomposition of diethyl ether, an ozone-reactive VOC, using Mn-based catalysts is therefore studied in the next section.

3.2. Continuous plasma-catalytic treatment of DEE in annular cordierite honeycomb supported catalysts

Redrafted from:

Quang Hung Trinh and Young Sun Mok, Catalysts 5(2015), 800-814

3.2.1. XRD characterization of the prepared catalysts

Powder XRD patterns for the bare cordierite and cordierite supported catalysts are shown in Fig. 21.
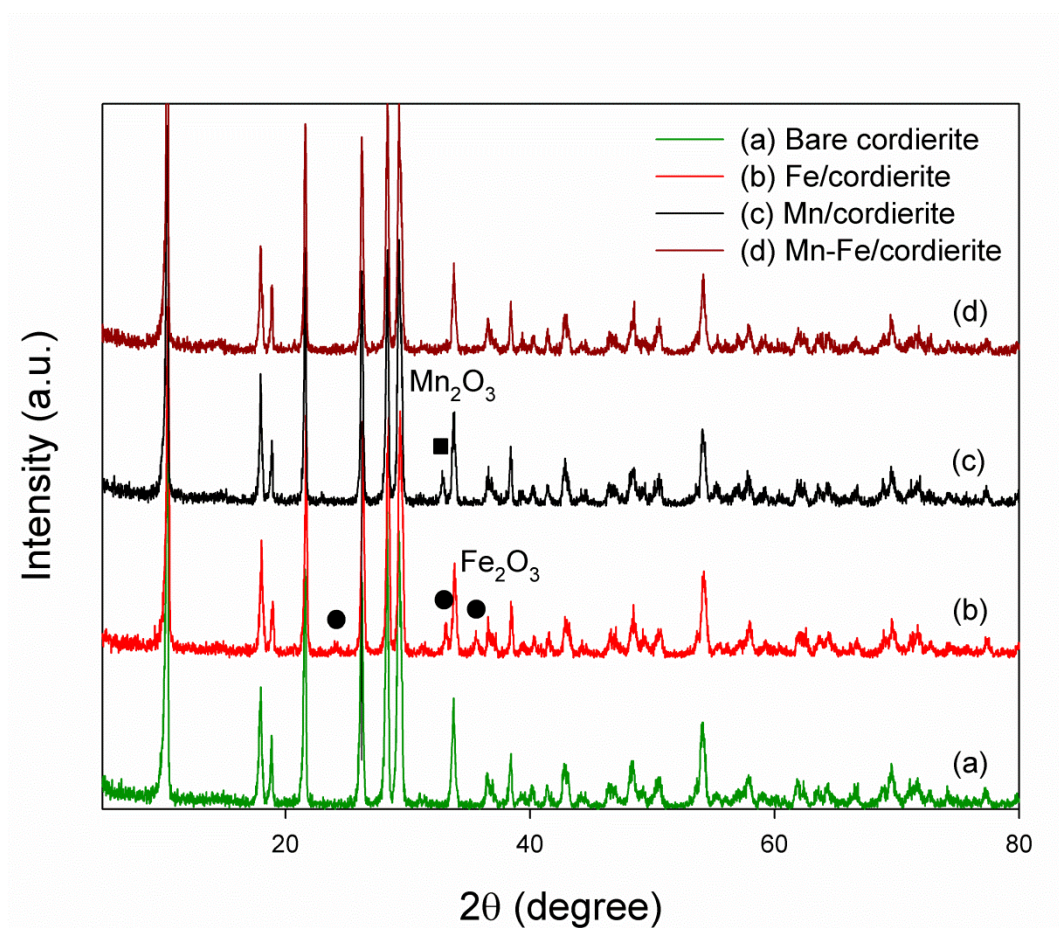
Figure 21. Powder XRD patterns of bare and coated cordierites.

As can be seen, the separate introduction of the manganese and iron oxides into cordierite led to the appearance of new diffraction peaks. For Fe/cordierite, several peaks were observed at 2θ, namely at 24.0°, 33.0°, and 35.6°, and were assigned to the formation of α-Fe_2O_3 [123]. A new peak that appeared at 32.8° for Mn/cordierite was attributed to the presence of Mn_2O_3. Other peaks of this phase (e.g., at 38.3° and 55.2°) overlapped with those of the support [124]. Interestingly, the XRD pattern of cordierite did not exhibit any changes after co-impregnation of the two metal oxides. This observation suggested a strong interaction between the Mn and Fe species, which likely existed as an amorphous mixed oxide. A similar result was reported by Lian et al. for a bimetallic Mn-Fe catalyst prepared by a hydrothermal method [87].

3.2.2. Catalytic activities of prepared catalysts for ozone decomposition

The catalytic activities of the prepared catalysts toward the decomposition of ozone generated in the air plasma were investigated and shown in Fig. 22(a). The preliminary experiment showed that the bare cordierite support did not show any activity for ozone decomposition. Meanwhile, all the prepared catalysts were observed to achieve a complete destruction of ozone early in the test. However, the performance of the catalysts subsequently decreased to different extents as a function of time-on-stream. Both the Mn and Fe-coated cordierites exhibited a drastic attenuation in their respective catalytic activities. Indeed, the ozone decomposition efficiency of Fe/cordierite reached zero after 6 h, whereas that of Mn/cordierite was reduced to only *ca.* 20 % during the same period of time. As expected, the behavior exhibited by Mn-Fe/cordierite differed from those of the other catalysts. The ozone decomposition efficiency for the mixed oxide catalyst gently decreased to *ca.* 89 % after 3 h, which exceeded the simple sum of those of the monometallic catalysts. This result clearly showed the synergistic effect of Mn and Fe on the decomposition of ozone. The low

crystallinity of the Mn-Fe mixed oxide, as observed by XRD, which indicated more defects and possibly an enhanced surface area, is believed to favor the decomposition of ozone [87].
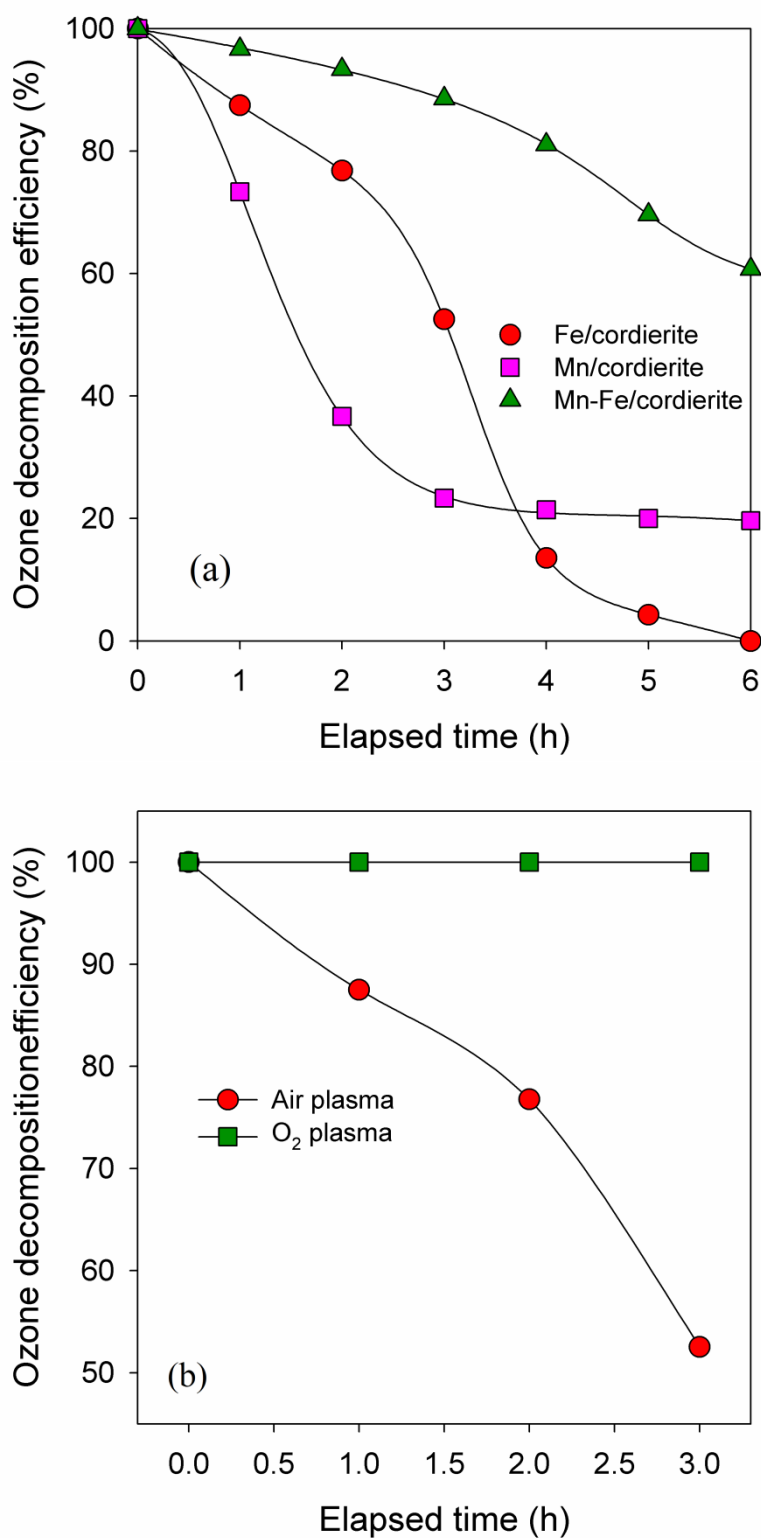
Figure 22. Ozone decomposition on prepared catalysts with air plasma (a) and on Fe/cordierite with oxygen plasma (b) (initial concentration: 300 ppm).

The deactivated Fe/cordierite was then regenerated at 250 $^{\circ}$C for 1h in ambient air to further investigate the catalyst performance for ozone decomposition with oxygen plasma. As shown in Fig. 22(b), Fe/cordierite recovered its catalytic activity after the thermal treatment. In contrast to its behavior in the presence of air-generated ozone, catalyst deactivation was not observed during 3 h with oxygen plasma. The nitrogen oxides (NO_x) that formed in the air plasma were thus considered to be responsible for the degradation of the catalysts. The strong adsorption of NO_x resulted in a blockage of the active sites that are used for ozone decomposition. In our preliminary experiment, the Fe/cordierite could not be regenerated below a temperature of 150 $^{\circ}$C. Hence, the selection of an ozone decomposition catalyst with a long-term stability at low temperature should be considered, especially in the two-stage arrangement. The use of oxygen plasma is ineffective unless a cyclic treatment (i.e., VOC adsorption followed by oxygen plasma oxidation) is applied [14,125].
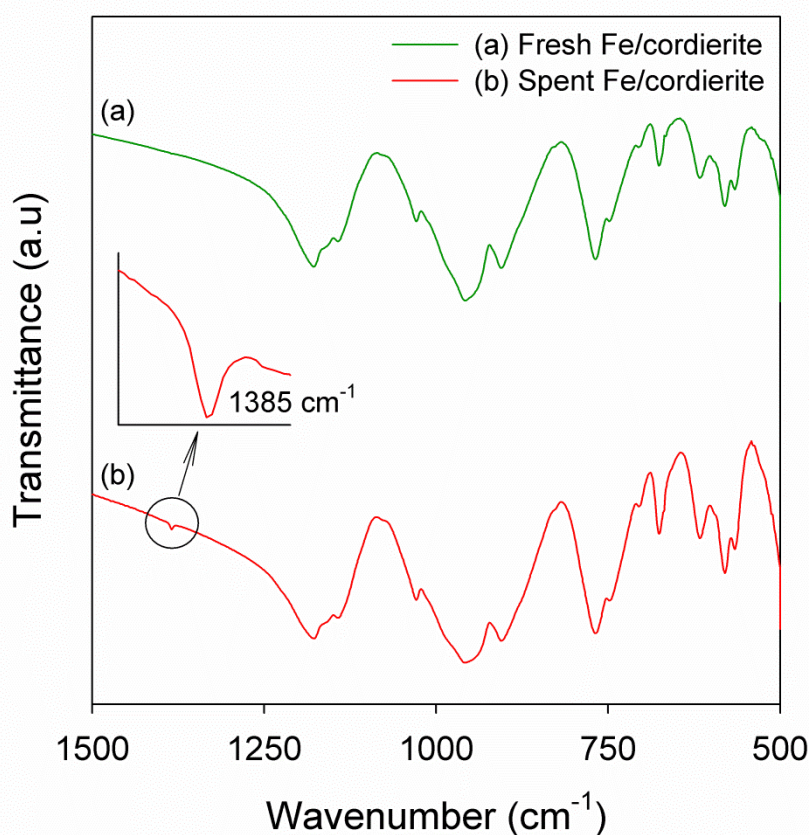
Figure 23. FTIR spectra of Fe/cordierite before and after ozone decomposition with air plasma.

54

Samples of Fe/cordierite were collected before and after the ozone decomposition test (with air plasma), after which they were powdered, thoroughly mixed with KBr, and then pelletized for FTIR characterization. As shown in Fig. 23, the FTIR spectrum of the supported catalyst did not display any characteristic changes after the ozone decomposition reaction, except for a peak that appeared at a wavenumber of 1385 cm^{-1}, which confirmed the presence of nitrate species (NO_3^-) that formed according to the following reactions [126]:

$$3NO_2 + O_2^-(\text{surf}) \rightarrow 2NO_3^-(\text{ads}) + NO \qquad \text{(R 44)}$$

$$2NO_2 + O_2^-(\text{surf}) \rightarrow NO_3^-(\text{ads}) + NO_2^-(\text{ads}) \qquad \text{(R 45)}$$

3.2.3. DEE decomposition in one-stage reactor
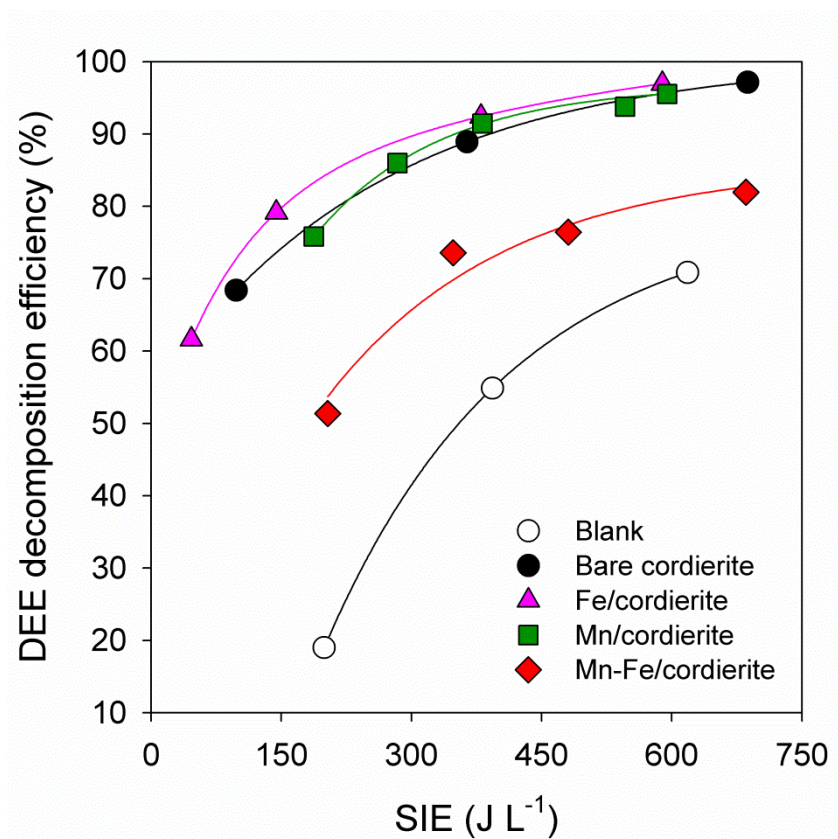
Figure 24. DEE decomposition efficiency in one-stage reactor with different catalysts

The DEE decomposition efficiency in one-stage reactor with different catalysts is shown in Fig. 24. For comparison, the experiment was also performed with the blank DBD reactor. Generally, in all of the cases, the DEE removal rate increased as the specific input energy (SIE) was increased. For the blank reactor, ca. 71 % of DEE conversion was obtained at an SIE of ca. 618 J L^{-1}, a result which was in good agreement with a previous report, which described the energy efficiency for DEE decomposition using a double dielectric barrier discharge (DDBD) reactor [42]. The introduction of cordierite honeycomb into the plasma appeared to improve the destruction of DEE, especially for low amounts of SIE. The improvement was probably due to the modification of plasma discharge and the extension of the DEE resident time. Unexpectedly, the separate incorporation of Fe and Mn into the cordierite did not lead to any further improvement in the DEE decomposition, indicating that, in this case, most of the DEE was destroyed by the plasma. Therefore, in the three particular cases, ca. 96 % of DEE was removed from the gas stream at an SIE of ca. 600 J L^{-1}. Jo et al. also reported a similar result for the plasma-catalytic decomposition of ethylene using bare and MnO_2-coated alumina ceramic membranes [90]. Even worse, the bimetallic Mn-Fe/cordierite catalyst lowered the DEE decomposition efficiency by more than 15 % across the whole range of SIEs that were used. Raising the SIE beyond this range to 900 J L^{-1} resulted in only a ca. 90 % of DEE conversion.

Figure 25(a) shows the outlet ozone concentration during decomposition of DEE in the one-stage reactor as a function of SIE with different catalysts. For comparison, the ozone concentration of the blank reactor is also included. At low SIE, the presence of the bare and Fe coated cordierites resulted in the formation of more ozone probably by enhancing the local electric field near the catalyst surfaces.
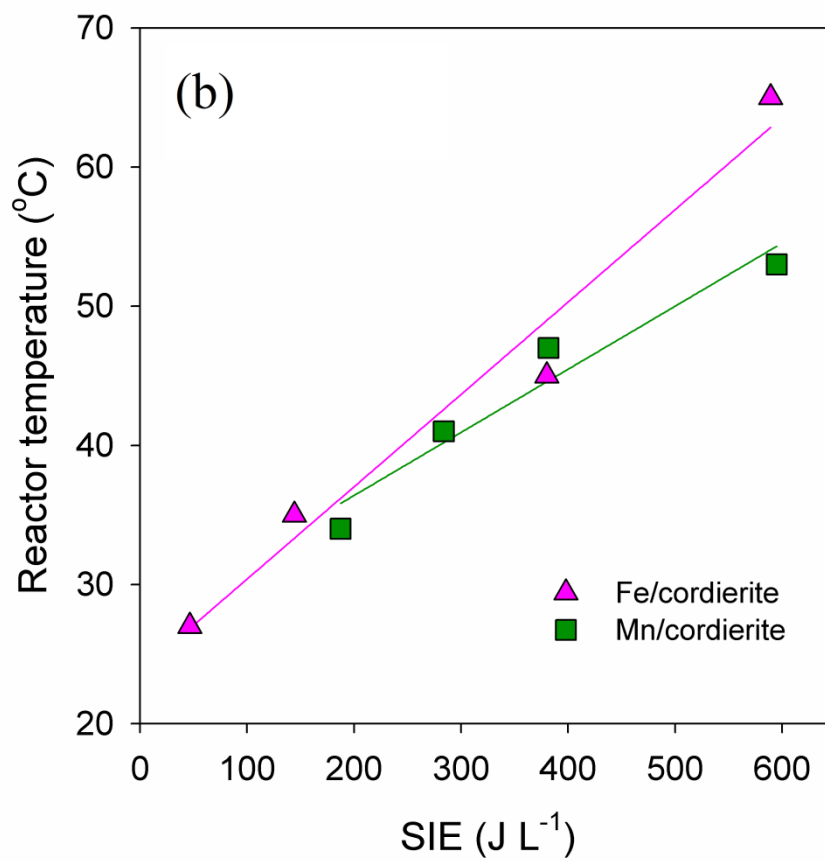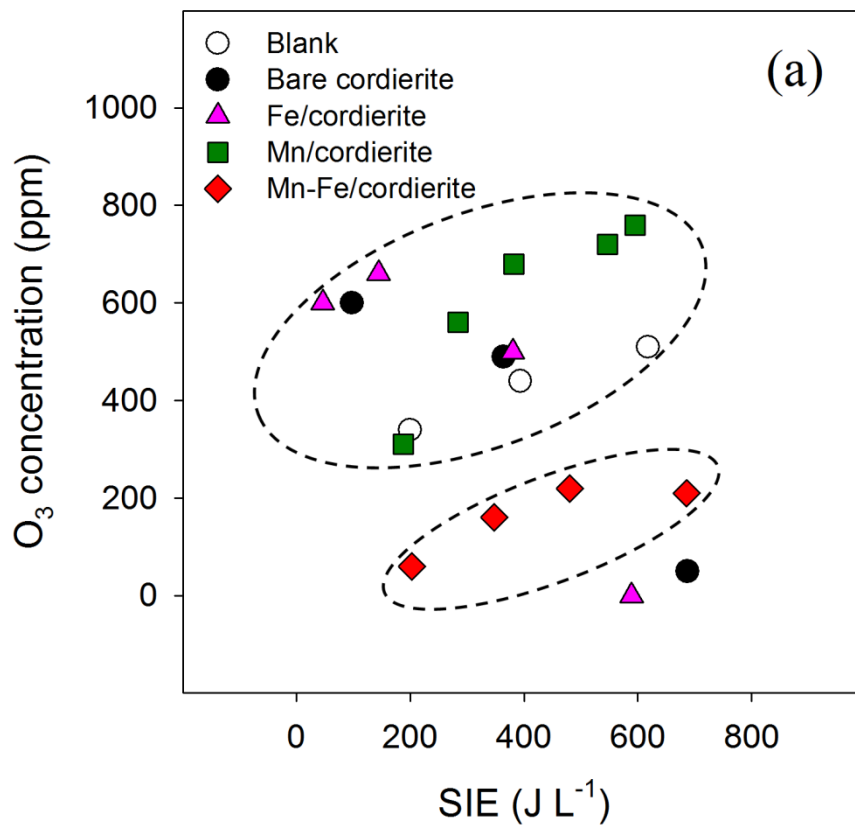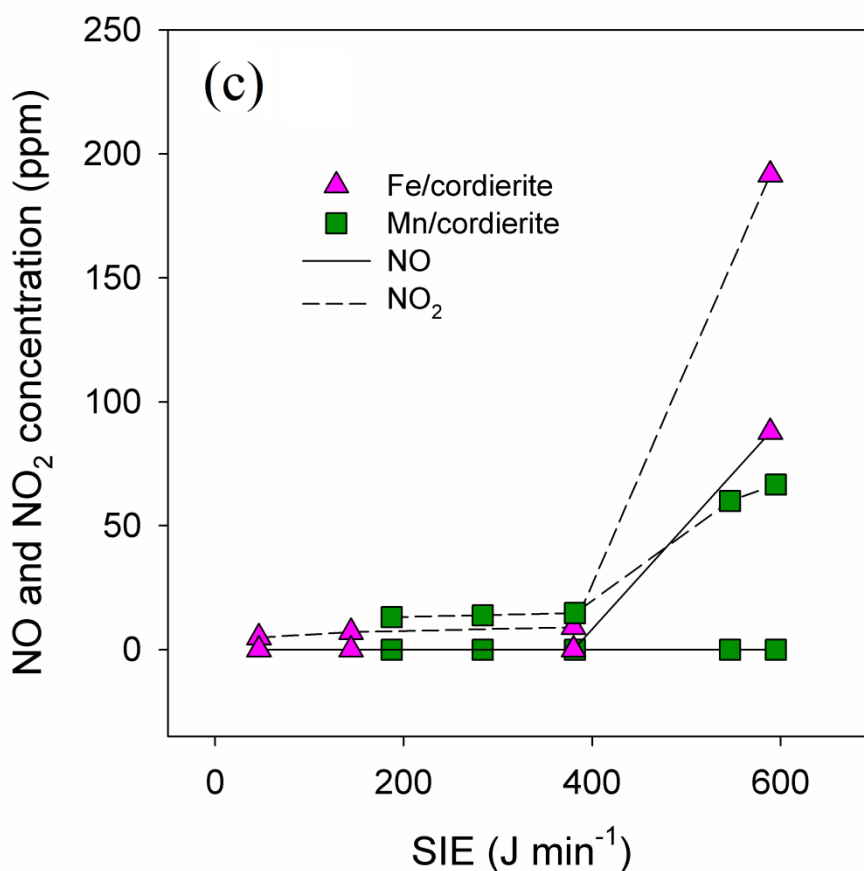
Figure 25. Outlet ozone concentration (a), reactor temperature (b) and NO and NO_2 concentrations (c) during decomposition of DEE in one-stage reactor.

As opposed to its reduced ability to affect DEE decomposition, the catalytic activity of the Mn-Fe/cordierite was observed to exceed those obtained using the other methods for ozone decomposition under plasma activation. The ozone concentration of Mn-Fe/cordierite was saturated at only 220 ppm, while the saturation values obtained otherwise ranged to above 600 ppm. This behavior was similar to that observed in the ozone decomposition test (shown in section 3.2.2). Thus, the one-stage combination of plasma with a well-performing ozone decomposition catalyst (i.e., Mn-Fe/cordierite) did not prove advantageous for the removal of DEE. It seemed that under plasma activation, Mn-Fe/cordierite accelerated the decomposition of O_3 to O_2, in that the adsorbed $O^{\bullet}$ radicals that formed were not mainly consumed during the

oxidation of DEE. As proposed by Li and Oyama [127], the decomposition of ozone is initiated by the dissociative adsorption of ozone to form an oxygen molecule and an atomic oxygen species, which in turn reacts with ozone to finally form molecular oxygen. The mechanism is summarized in the reaction sequence (R 6) to (R 8) (see section 3.1.3). Through reaction (R 7), the ozone that effectively formed near the catalyst surface might compete with the DEE for atomic oxygen. The low DEE decomposition efficiency with Mn-Fe/cordierite suggested that in plasma, besides active short-lived species, ozone itself played a significant role in the reaction of DEE. In an earlier study, Ogata et al. [128] also reported that the use of a Cu-Cr catalyst to dissociate ozone into active atomic oxygen species was not effective for the reaction under plasma discharge, for which the extent of the decomposition of toluene and dichloromethane in a one-stage reactor was almost the same or even worse (for an increasing amount of catalyst) than in a conventional plasma reactor. These authors concluded that, for the single-stage combination (i.e., the one-stage arrangement), the ozone decomposition property of the catalysts was not important. Similarly, Van Durme et al. [129] found that when MnO_2-CuO/TiO_2 was subjected to a plasma, it resulted in a low toluene removal efficiency compared to TiO_2, which does not have the ability to decompose ozone. However, a positive effect was observed for in-plasma supported MnO_x when dealing with acetone, a persistent compound [81,126], in which case the formation of ozone-induced atomic oxygen therefore becomes important. It is noted that, unlike acetone, the above VOCs (e.g., ethylene, diethyl ether, and toluene) are more reactive with ozone. The gas-phase reaction of ozone with toluene, for example, is slow; however, in the presence of plasma discharge, ozone could be excited, whereby its activity increased [130,131]. The destruction of vibrationally excited ozone, generated by three-body reaction, was reported to be about 1600 times faster than ground-state ozone due to collisions with oxygen atoms [132,133].

Interestingly, the ozone concentrations of the bare and Fe-coated cordierites reached almost zero at a high SIE of ca. 600 J L^{-1}. In our preliminary experiment, ozone was only significantly decomposed in the gas phase above 150 ^{o}C; however, as seen in Fig. 25(b), the reactor temperature did not exceed 70 ^{o}C, indicating the negligible thermal decomposition of ozone. The occurrence of a zero ozone concentration at high input energies was also reported elsewhere [128,134]. It was proposed that O_3 is consumed by NO, which is favorably formed at high SIE values to produce NO_2, which subsequently reacts with atomic oxygen to regenerate NO [135]. The catalytic cycle for O_3 destruction by NO_x is described as follows:

$$NO + O_3 \rightarrow NO_2 + O_2 \qquad\qquad (R\ 46)$$

$$NO_2 + O \rightarrow NO + O_2 \qquad\qquad (R\ 47)$$

Net reaction:

$$O_3 + O \rightarrow O_2 + O_2 \qquad\qquad (R\ 48)$$

The concentrations of NO_x at the outlet of the one-stage reactor for the Mn and Fe coated cordierites were measured during plasma-catalytic oxidation of DEE. As can be seen in Figure 25(c), NO was not detected within the investigated range of SIE for Mn/cordierite but appeared at above 400 J L^{-1} for the Fe/cordierite. Meanwhile, the formation of NO_2 slowly took place at SIE below 400 J L^{-1} for both catalysts and then steeply increased as further raising SIE, especially for the Fe/cordierite. At the SIE of *ca.* 590 J L^{-1}, the NO_2 concentration obtained with the Fe/cordierite reached *ca.* 190 ppm, while that of the Mn/cordierite was only *ca.* 60 ppm. The concentration of NO was much less than that of NO_2 because NO rapidly reacted with ozone (R 46) and atomic oxygen (R 49) to form NO_2.

$$NO + O \rightarrow NO_2 \qquad\qquad (R\ 49)$$

The regeneration of NO from NO_2 through reaction (47) was relatively slow. The behaviors of the two catalysts for the formation of NO_x were in contrast to their effects on the O_3

concentration at high SIE shown in Figure 25(a), indicating that NO_x played significant roles in the suppression of O_3 formation.

Our results indicated that it is possible to improve the performance of the reactor by using a hybrid reactor containing Mn/cordierite in the plasma and Mn-Fe/cordierite in the post-plasma stage. This reactor, henceforth denoted as the Mn+(Mn-Fe) reactor, was proposed for further experiments (see Fig. 7(c), section 2.2.3), in which the post-plasma catalyst bed was left at room temperature.

3.2.4. DEE decomposition in Mn+(Mn-Fe) reactor
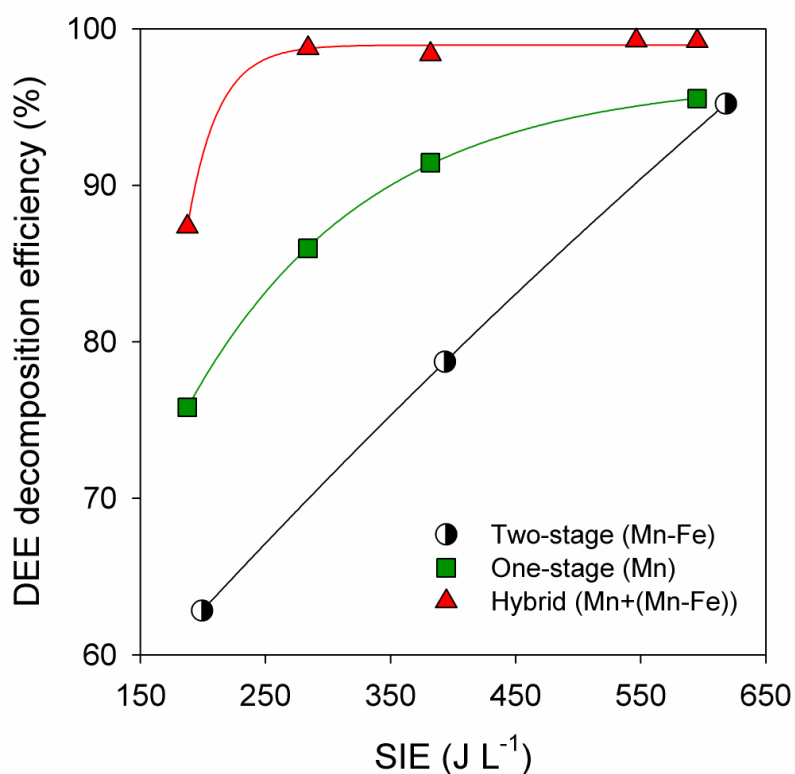
Figure 26. DEE decomposition efficiency of hybrid Mn+(Mn-Fe) reactor and one-stage reactor with Mn/cordierite catalyst.

As seen from the Fig. 26, the efficiency of the DEE decomposition increased by more than 10 % compared to that without Mn-Fe/cordierite at SIE values below 300 J L^{-1}, after which saturation occurred at around 99 %. Thus, an appropriate combination of plasma with the two Mn-based catalysts resulted in an obvious improvement of the reactor performance in terms of both DEE conversion and energy consumption. The ozone that formed during plasma discharge and its catalytic dissociation to produce atomic oxygen in the post-plasma stage was thus effective for achieving the oxidation of DEE.
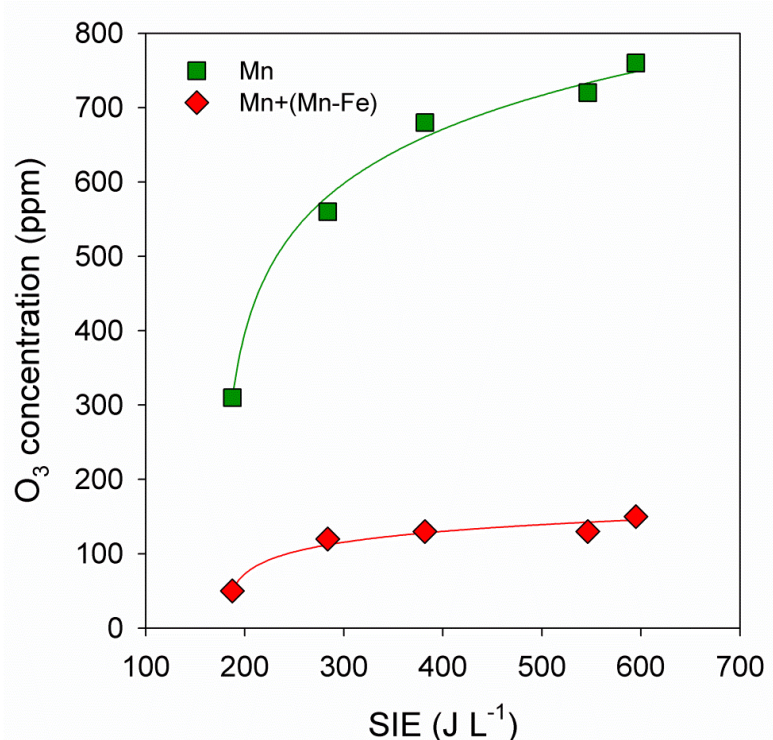
Figure 27. Outlet ozone concentrations of Mn+(Mn-Fe) hybrid and Mn one-stage reactors.

The combination also substantially diminished the emission of ozone, a toxic gas, to levels below 200 ppm (Fig. 27). Additionally, it is shown in Figure 26 that the hybrid reactor was also more efficient than the two-stage reactor with Mn-Fe/cordierite as the post-plasma catalyst, especially at low values of SIE. The result came from the advantage of the in-plasma catalysts, which probably altered the plasma discharge mode and enhanced the residence time of gaseous species.
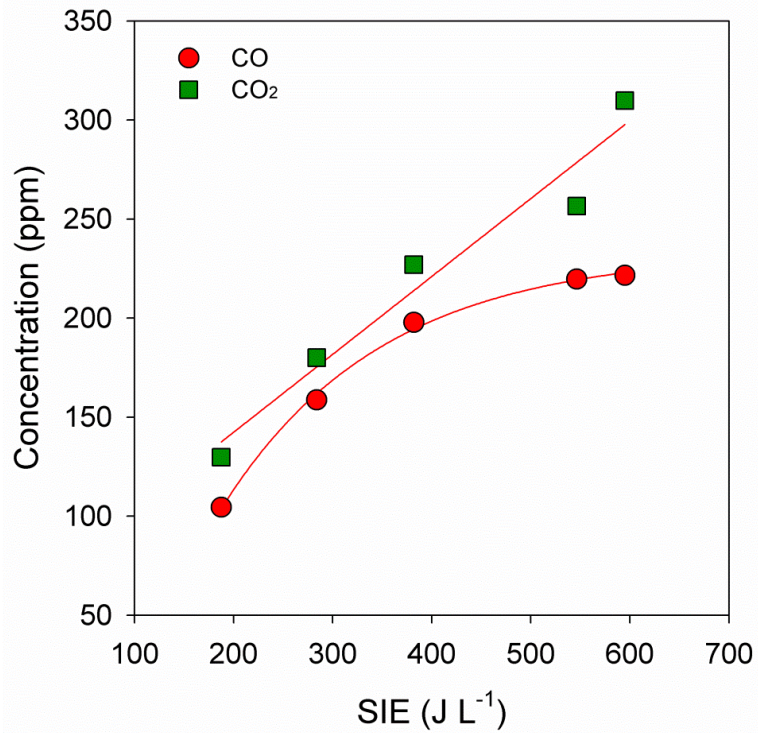
Figure 28. CO_x concentrations during DEE decomposition in hybrid Mn+(Mn-Fe) reactor.
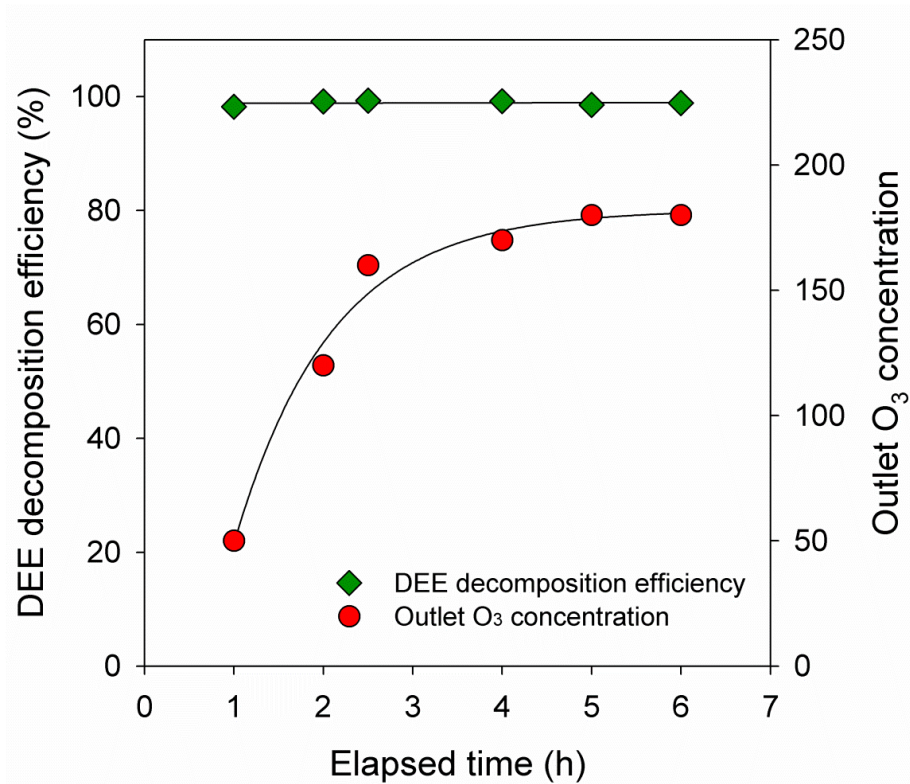
Figure 29. DEE decomposition efficiency and outlet ozone concentration of hybrid Mn+(Mn-Fe) reactor at SIE of 382 J L^{-1}.

The concentrations of carbon oxides (CO and CO_2) that were detected during DEE decomposition in the Mn+(Mn-Fe) reactor are shown in Fig. 28. The amount of CO_2 increased almost linearly as the SIE was increased, whereas that of CO tended to rise exponentially to a maximum within the SIE range. These trends were also observed in previous studies, thereby implying a high degree of oxidation of VOCs to CO_2, which is favored at high SIEs [81,90]; that is, ca. 89 % of DEE was oxidatively transformed to carbon oxides at around 600 J L^{-1}.

The stabilities of catalysts used in the Mn+(Mn-Fe) reactor were judged in terms of DEE decomposition efficiency and outlet ozone concentration at SIEs of ca. 382 J L^{-1}. From Fig. 29, it can be seen that there was no decline in the DEE decomposition efficiency during the course of experiment. The outlet ozone concentration, however, increased with time-on-stream and reached a steady-state at 180 ppm after 5 h. This indicated that the unreacted DEE and oxidation products, such as CO_x, H_2O, and the intermediates that had reversibly adsorbed on Mn-Fe/cordierite, could partially inhibit NO_x adsorption, slowing down the catalyst deactivation.

In summary, the removal of dilute diethyl ether (DEE, concentration: 150 ppm) from an air stream (flow rate: 1 L min^{-1}) using non-thermal plasma combined with different cordierite-supported catalysts, including Mn, Fe, and mixed Mn-Fe oxides, is investigated. The experimental results show that the decomposition of DEE occurs in a one-stage reactor without the positive synergy of plasma and supported catalysts, by which ca. 96 % of DEE is removed at a specific input energy (SIE) of ca. 600 J L^{-1}, except when the mixed Mn-Fe/cordierite is used. Among the catalysts that were examined, Mn-Fe/cordierite, the catalyst that is the most efficient at decomposing ozone is found to negatively affect the decomposition of DEE in the one-stage reactor. It is proposed that in plasma, a large amount of ozone is rapidly decomposed on Mn-Fe/cordierite to molecular oxygen without involvement in the oxidation of DEE. However,

when Mn-Fe/cordierite is utilized as catalyst in the post-plasma stage of the two-part hybrid reactor, in which Mn/cordierite is directly exposed to the plasma, the reactor performance in terms of DEE decomposition efficiency is improved by more than 10 % compared to that achieved without Mn-Fe/cordierite at low values of SIE. The ozone that is formed during the plasma stage and its subsequent catalytic dissociation during the post-plasma stage to produce atomic oxygen therefore play important roles in the removal of DEE.

------------------------o0o------------------------

The plasma-catalytic continuous treatment of acetone and DEE with proper combination of NTP and tandem Mn-based catalysts has shown a great enhancement in the VOC removal efficiency and reduction of byproduct and ozone emissions. However, the energy efficiency of the process is still low, especially at very low VOC concentration because the plasma-induced reactive species mainly react with the background gas molecules. Enrichment of VOCs by adsorption on the adsorbent/catalyst before plasma ignition is a feasible way to increase the VOC concentration in the plasma region and therefore increase the number of treated VOC molecules per unit of consumed energy. The major requirement of such cyclic treatment is that VOCs are completely removed from the gas stream during a long-time adsorption step, while NTP should be able to regenerate the adsorbent/catalyst by oxidative desorption of adsorbed VOCs in the subsequent short-time oxidation stage. In the next section, cyclic treatment of acetone will be investigated and compared with the continuous treatment under the same operating conditions.

3.3. Adsorption and plasma-catalytic oxidation of dilute acetone over β-zeolite supported silver nanoparticles

Redrafted from:

Quang Hung Trinh, M. Sanjeeva Gandhi and Young Sun Mok, Japanese Journal of Applied Physics 54 (2015) 01AG041-6

3.3.1. TEM characterization of the catalyst
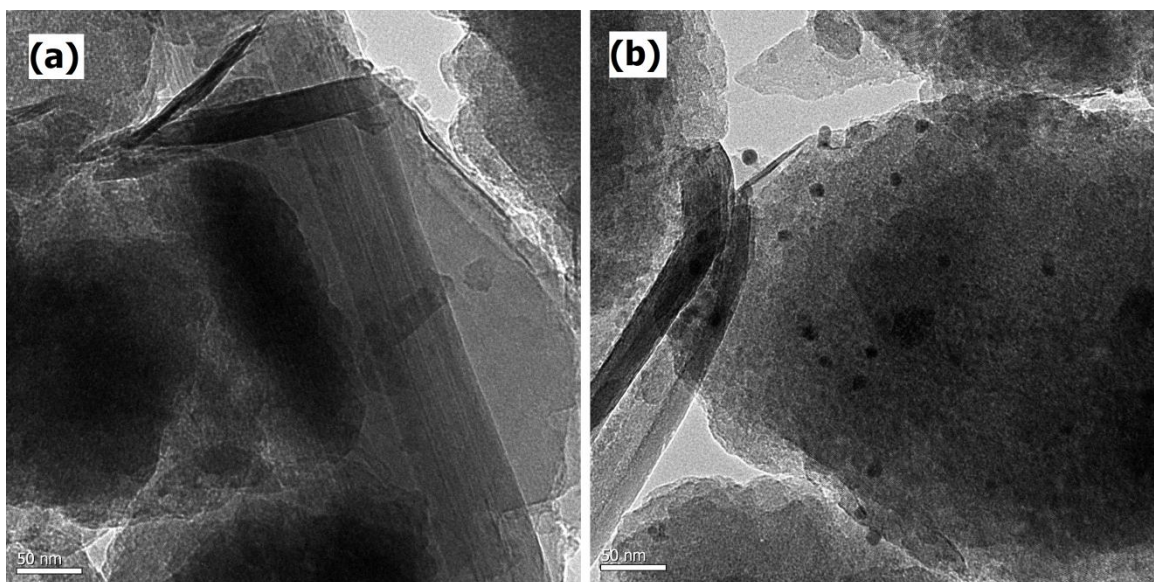
Figure 30. TEM images of bare zeolite (a) and Ag-coated zeolite (b).

TEM images of the bare and Ag-coated zeolites are shown in Fig. 30. The black spots in Fig. 30(b) indicated the presence of Ag nanoparticles with an average particle size of *ca.* 12 nm.

3.3.2. Adsorption capacity of the Ag-coated zeolite
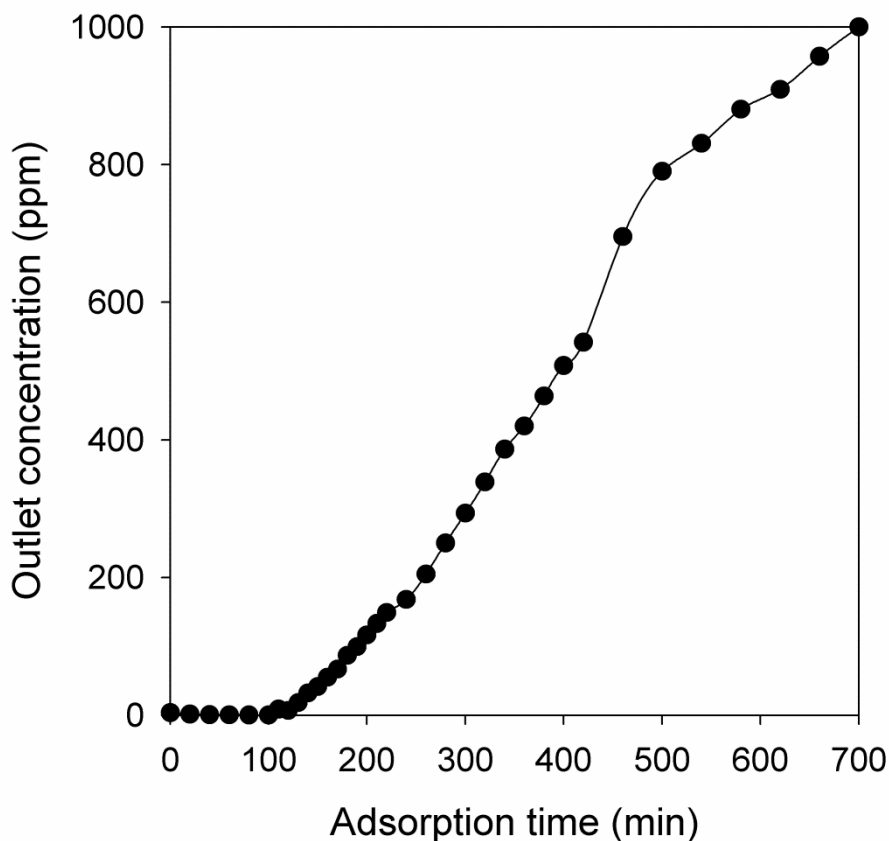
Figure 31. Temporal variation of acetone concentration at outlet of packed-bed column (inlet

acetone concentration: 1000 ppm, Ag-coated zeolite: 30 g).

Figure 31 shows the temporal variation of the acetone concentration at the outlet of the packed-bed column (30 g of adsorbent) for an inlet concentration of 1000 ppm. As seen, for the first 100 min of the adsorption, acetone was almost completely removed from the gas stream, and then the concentration of acetone gradually increased, reaching the inlet concentration in 700 min. From the breakthrough curve, the amount of acetone adsorbed on the Ag-coated zeolite was estimated to be 1.07 mmol g^{-1} at 25 $^{\circ}$C.

3.3.3. Gaseous product formation in one cycle of treatment

As aforementioned, during the adsorption step, the model gas at an acetone concentration of 300 ppm was continuously fed into the reactor for 100 min. During this step, acetone was not detected at the outlet of the reactor. The amount of acetone accumulated in the reactor was calculated to be 2.45 mmol.
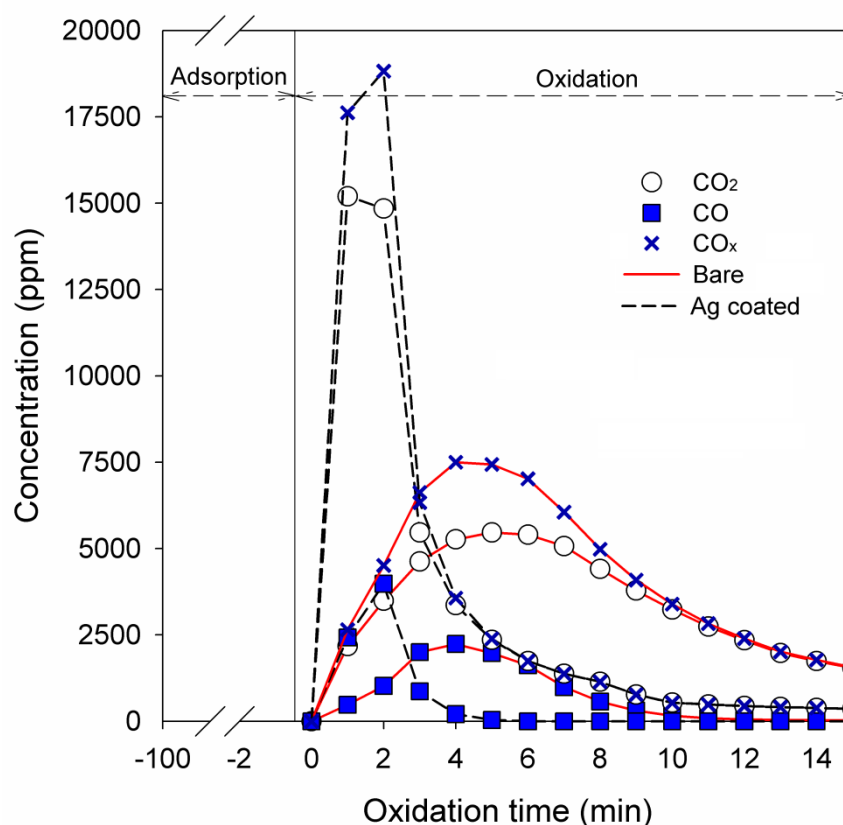
Figure 32. Concentrations of CO and CO_2 for one cycle of treatment with and without Ag loading (discharge power: 25 W for bare zeolite; 28 W for Ag-coated zeolite).

Figure 32 shows the concentrations of CO and CO_2 produced during the plasma-catalytic oxidation step (15 min) for the bare and Ag-coated zeolite. The discharge power determined from the Lissajous voltage-charge figure was 25 W for the bare zeolite and 28 W for the Ag-coated zeolite. As can be seen, the concentration of CO_x (CO and CO_2) obtained with the Ag-

coated zeolite sharply increased to the maximum value (about 18800 ppm), and then quickly

decreased within 10 min. Thereafter, the concentration of CO_x kept below 400 ppm. On the

other hand, the concentration of CO_x obtained with the bare zeolite slowly increased to the

maximum value (about 7500 ppm), and then slowly decreased. In both cases, CO_2 was more

abundant than CO in the effluent stream. For cyclic treatment of VOCs, the combination of

plasma and silver catalyst not only minimized the emission of ozone but also speeded up the

oxidation reactions, and therefore, shortened the plasma-catalytic oxidation period. In Fig. 32,

the peaking of CO_x concentration for Ag-coated zeolite in the early stage of the plasma-catalytic

oxidation step can be attributed to the generation of strong oxidizing atomic oxygen from the

decomposition of ozone on the surface of silver catalyst.
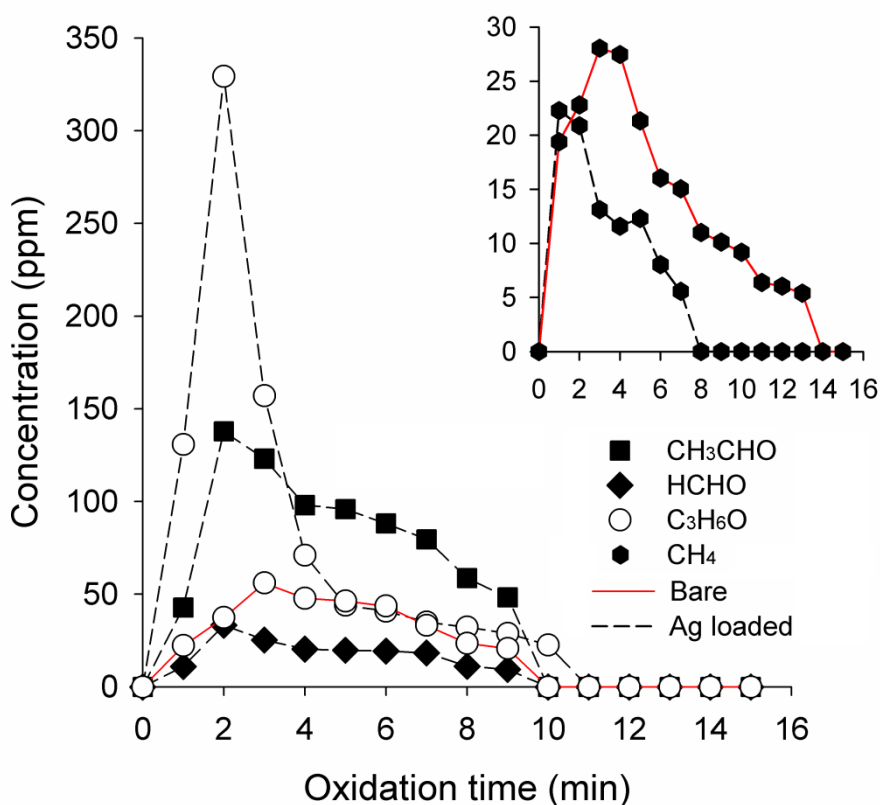
Figure 33. . Concentrations of desorbed acetone and the gaseous organic byproducts produced

during oxidation step for one cycle of treatment with and without Ag loading (discharge power:

25 W for bare zeolite; 28 W for Ag-coated zeolite).

The concentrations of desorbed acetone and other carbon-containing byproducts produced during the plasma-catalytic oxidation step are shown in Fig. 33. The desorption of acetone lasted for about 10 min when the Ag-coated zeolite was used. The instant concentration of the acetone desorbed from the Ag-coated zeolite surpassed that from the bare zeolite probably due to partial blockage of zeolite pores by Ag nanoparticles. However, considering that the adsorption was carried out for 100 min, the amount of the acetone desorbed was not so much.

As shown in the inset of Fig. 33, methane (CH_4) was the only carbon-containing byproduct other than CO_x when the bare zeolite was used. The use of the Ag-coated zeolite somewhat reduced the formation of CH_4, however, gave rise to the formation of formaldehyde (HCHO) and acetaldehyde (CH_3CHO). The increases in the concentrations of aldehydes with the Ag-coated zeolite can be explained with the enhanced oxidation of adsorbed acetone and intermediates to gaseous byproducts due to the highly oxidative atomic oxygen formed on the catalyst surface. For the Ag-coated zeolite, the removal efficiency, carbon balance and fraction of CO_x contributed to the carbon balance were estimated to be 97.0, 66.8 and 61.8 %, respectively. The energy efficiency with adsorption/oxidation cyclic treatment was calculated to be 19.72 g kW h^{-1}.

Figure 34 shows the temporal variations of the ozone concentration in the effluent stream during the plasma-catalytic oxidation step. For the bare zeolite, the concentration of ozone suddenly started to increase up to 350 ppm at ca. 1 min and then decreased. After the initial transient state, the concentration of ozone maintained stable at ca. 30 ppm. On the other hand, the concentration of ozone obtained with the Ag-coated zeolite kept almost constant at ca. 20 ppm throughout the plasma-catalytic oxidation step.
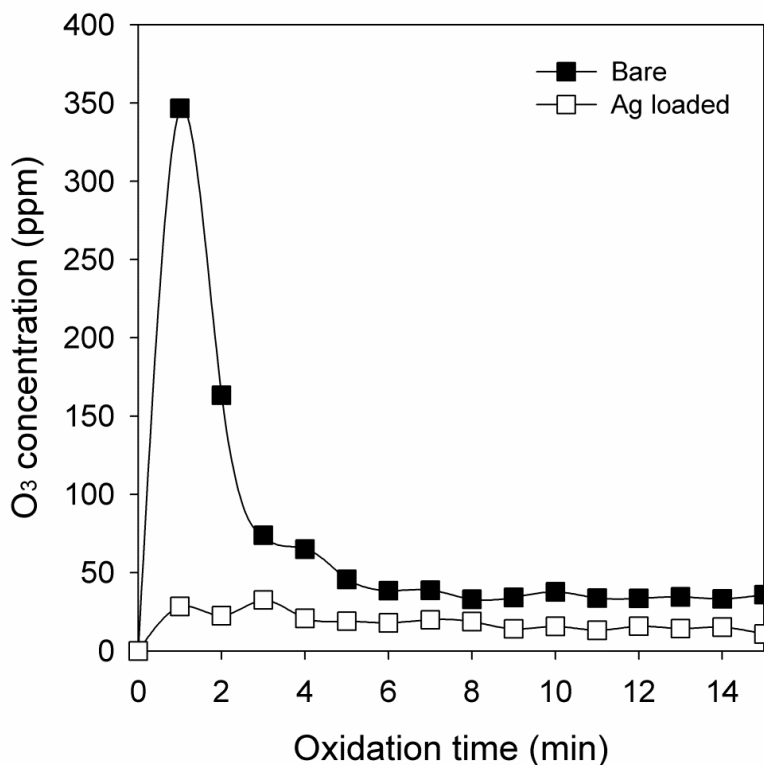
Figure 34. Temporal variations of O_3 concentration in effluent during oxidation step for bare and Ag-coated zeolite (discharge power: 25 W for bare zeolite; 28 W for Ag-coated zeolite).

3.3.4. Gaseous product formation during four cycles of treatment

Four consecutive adsorption/plasma-catalytic oxidation cycles were performed using the Ag-coated zeolite. The concentrations of carbon-containing products and desorbed acetone are shown in Fig. 35. During plasma-catalytic oxidation steps, the contents of all emitted compounds rapidly increased in the early stage, showing maxima at the same time, and then gradually decreased. Within four cycles corresponding to more than 7 h of continuous treatment, there was no significant deactivation of the catalyst. Besides, it was observed that the concentration curves tended to be broader as the adsorption/plasma-catalytic oxidation cycles were repeated. This phenomenon may have resulted from the formation and accumulation of low volatile or nonvolatile byproducts. During the plasma-catalytic oxidation step, not only the

adsorbed acetone but also such low volatile or nonvolatile byproducts deposited on the surface are oxidized to produce gaseous compounds such as CO, CO_2, aldehydes and methane, which makes their concentration peaks wider. The formation of low volatile or nonvolatile compounds during the plasma treatment of VOCs has been evidenced previously.
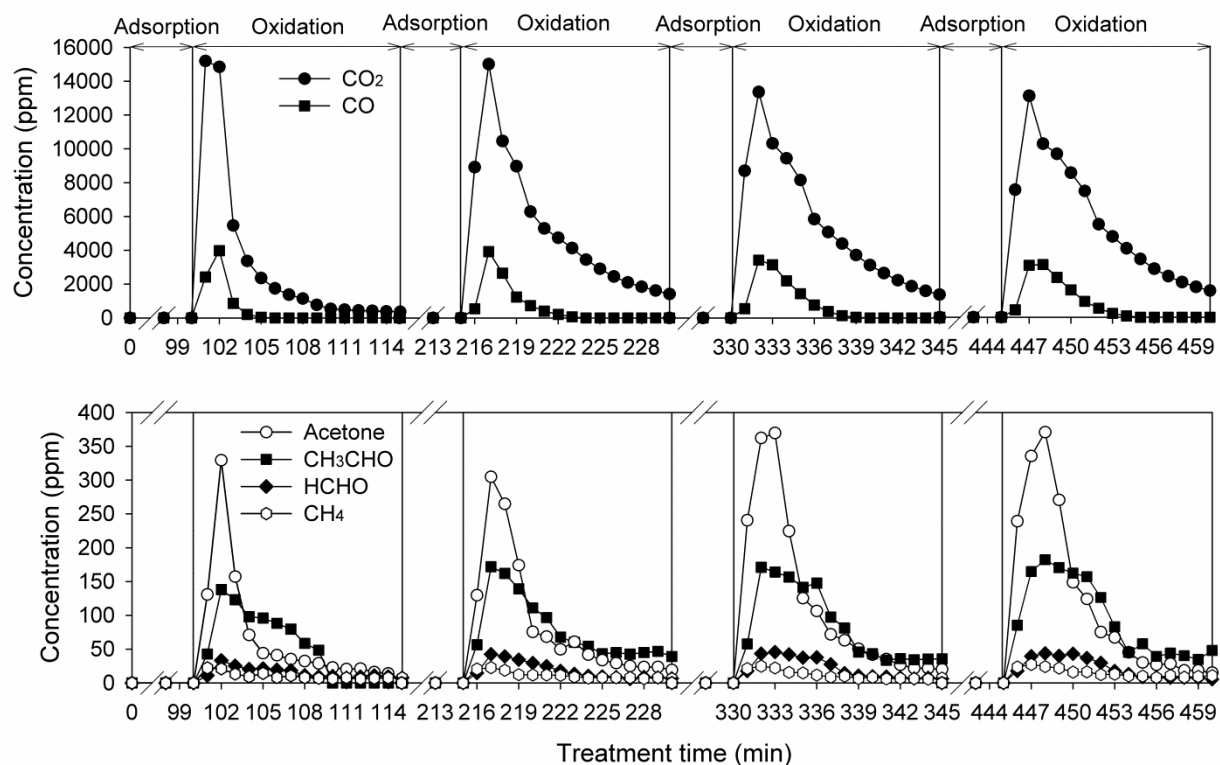
Figure 35. Concentrations of gaseous products and desorbed acetone during four cycles of treatment using Ag-coated zeolite.

3.3.5. Gaseous product formation during continuous treatment of acetone

In the both cases of bare and Ag-coated zeolites, the carbon-containing products identified for continuous plasma-catalytic treatment were only CO and CO_2 (Fig. 36).
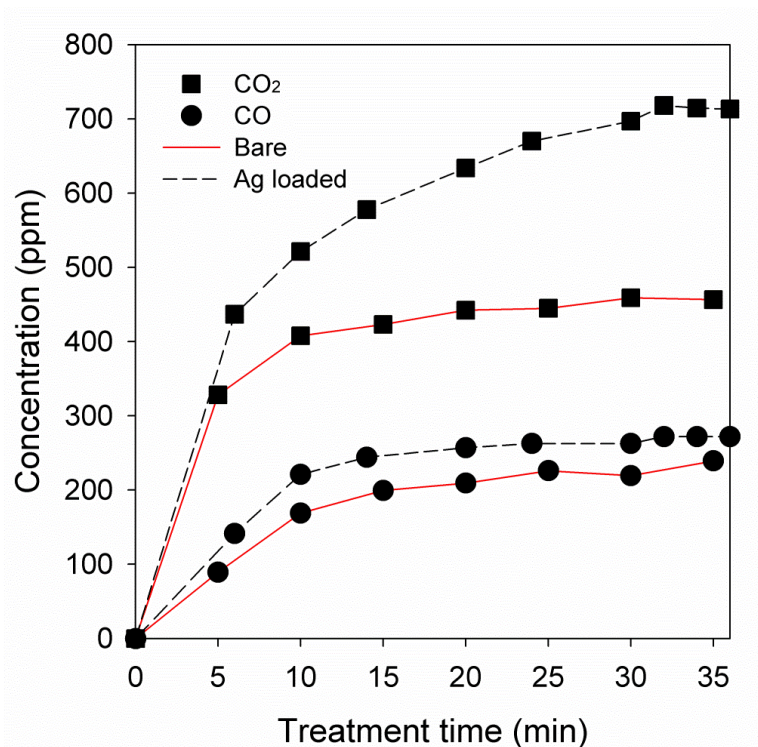
Figure 36. Concentrations of CO_x from continuous treatment using bare and Ag-coated zeolite.

As seen, the increases in the concentrations of carbon oxides were rapid in the early stage, and then slowed down, reaching steady-state in about 30 min. The Ag-coated zeolite produced more CO and CO_2 than the bare zeolite. At the reactor outlet, concentration of unreacted acetone was measured to be negligible, less than 1 % of the initial concentration regardless of catalysts used. However, compared to the cyclic treatment, the continuous treatment exhibited much lower energy efficiency (ca. 3.05 g kW h^{-1}).

The main reaction pathways responsible for the formation of gaseous byproducts are proposed and described in Fig. 37. The gaseous (Fig. 37(a)) and adsorbed (Fig. 37(b)) acetone molecules are first dissociated into CH_3 and CH_3CO radicals by plasma-induced energetic species such as electrons and $N_2^*(A^3\Sigma_u^+)$ (path (1)). Subsequently, the recombination of CH_3CO fragments in the gas phase leads to the formation CH_3CHO (path 2). Meanwhile, CH_3 fragment

could be further dissociated to create atomic hydrogen (H) and CH_2 free radicals. These radicals, in turn, react with hydroxyl radicals (OH) to generate HCHO (path (14)).
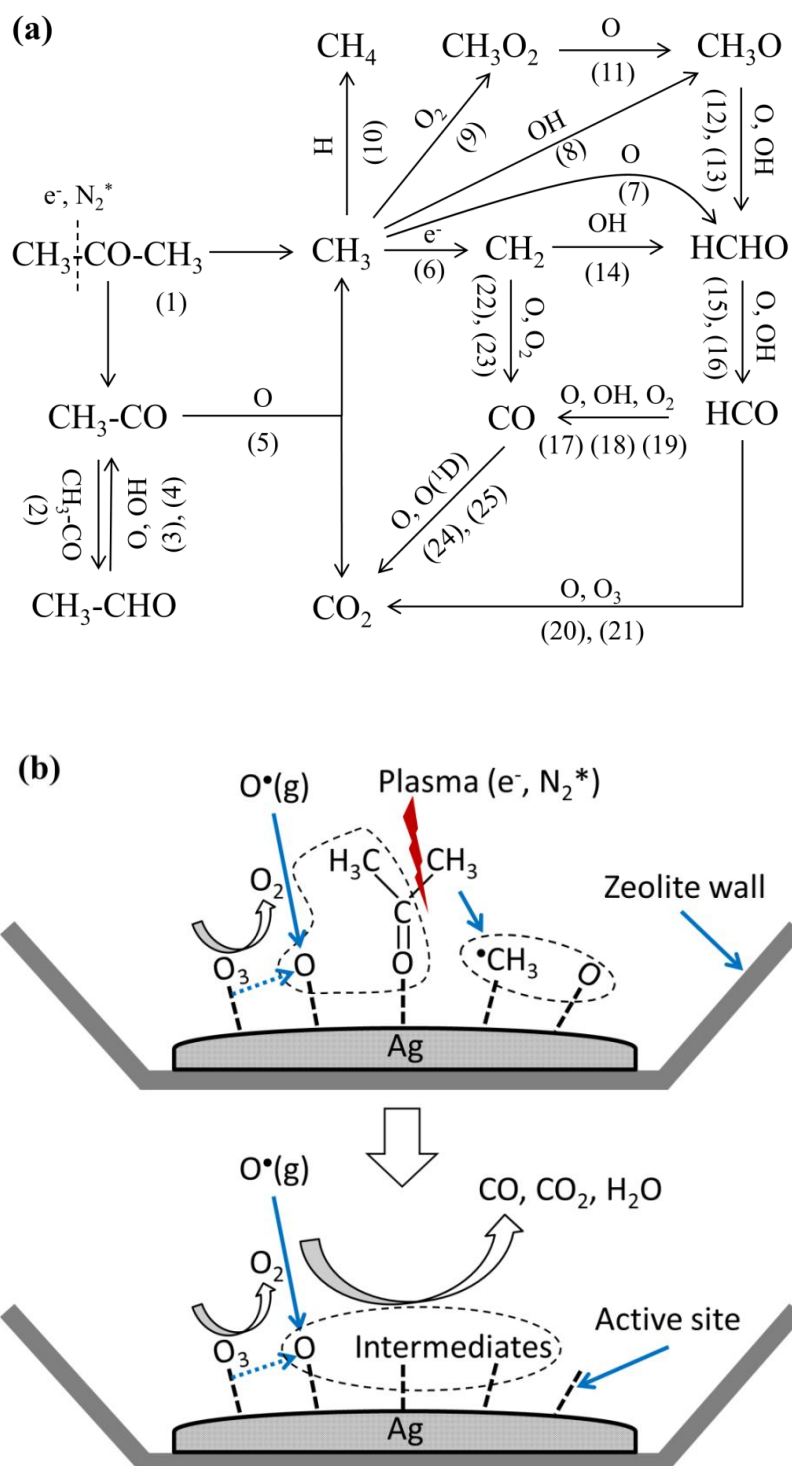
Figure 37. Proposed reaction pathways for acetone oxidation in gas phase (a) and on catalyst (b).

Some other pathways such as (8), (12) and (13); and (9) and (11)-(13) also explain the formation of HCHO. The combination of H and CH_3 (path 10) is responsible for the generation of CH_4. Further oxidations of the intermediates by the oxidizing agents such as atomic oxygen (O), OH radicals and O_2 finally lead to the formation CO_x through (15)-(25). The rapid formation of CO_2 and relatively low content of ozone during the first 4 min of the oxidation step in presence of silver catalyst clearly showed that the decomposition of ozone took place on the silver catalyst to produce atomic oxygen, eventually facilitating the oxidation process. Regarding the plasma-catalytic oxidation of the adsorbed acetone, the carbon balance was not good (66.8 %). The low carbon balance was also observed in other works. Sivachandrian et al. [136] investigated the coupling of titanium oxide as a sorbent with plasma. When the regeneration of acetone-adsorbed TiO_2 surface was performed, the global fraction of adsorbed species removed from the surface by the plasma treatment was about 27 %, and only 12 % of which was converted to CO_x.

To summarize, the abatement of acetone using a combination of non-thermal plasma, catalysis and adsorption is investigated using silver nanoparticle-coated β-zeolite serving as both adsorbent and catalyst. The effects of the zeolite-supported silver catalyst on the reduction of unwanted ozone emission and the behavior for the formation of gaseous byproducts are examined. The experimental results showed that the β-zeolite had a high acetone adsorption capacity. Acetone with a concentration of 300 ppm is removed from the gas stream and enriched on the zeolite surface during the adsorption step of the cyclic process (100 min). In the succeeding step, the adsorbed acetone is plasma-catalytically treated under oxygen-flowing atmosphere to recover the adsorption capability of the surface. The plasma-catalytic oxidation of the acetone adsorbed in the previous adsorption step is completed in 15 min. The abatement of acetone by the cyclic adsorption and plasma-catalytic oxidation process is able to increase the performance of the reactor with respect to the energy efficiency, compared to the case of

continuous treatment. The use of the zeolite-supported silver catalyst largely decreases the emission of unreacted ozone and shortened the oxidation time due to the enhanced oxidation of the adsorbed acetone and intermediates.

------------------------o0o------------------------

The excellent adsorption capability of acetone on zeolite surface is one of the key features to achieve the high energy efficiency in the cyclic treatment. However, different from ketones, the highly volatile organic compounds such as olefins (without polar functional groups within the molecule) usually have low affinity to be adsorbed on the commercial zeolites (e.g., 4A, 13X, Y, and β-zeolite), and therefore the modification of these adsorbents towards improving the adsorption capacity is required. The effects of the modifying 13X zeolite by silver and bimetallic silver-M (M: Co, Cu, Fe and Mn) on the ethylene adsorption and plasma-catalytic oxidation will be investigated in the next section.

3.4. Adsorption and plasma-catalytic oxidation of dilute ethylene over silver-based bimetallic impregnated 13X zeolite

3.4.1. Catalyst characterization

Figure 38 shows the XRD patterns of the commercial 13X zeolite before and after loading Ag (1.0 and 1.5%) and Ag-Fe (1.0-0.7%). The patterns of the other samples were also taken, which are however not shown here. Despite incorporating metals into the zeolite, all the catalysts prepared showed similar XRD patterns to the bare zeolite, with no appearance of additional diffraction peaks. This observation suggests that the silver and transition metal species were highly dispersed in the zeolite cavities and below the detection limit for XRD.

The TEM images of the bare 13X and Ag(1.0 %)/13X, as shown in Fig. 39, further supports for this inference as the active component was hardly distinguished from the zeolite support.
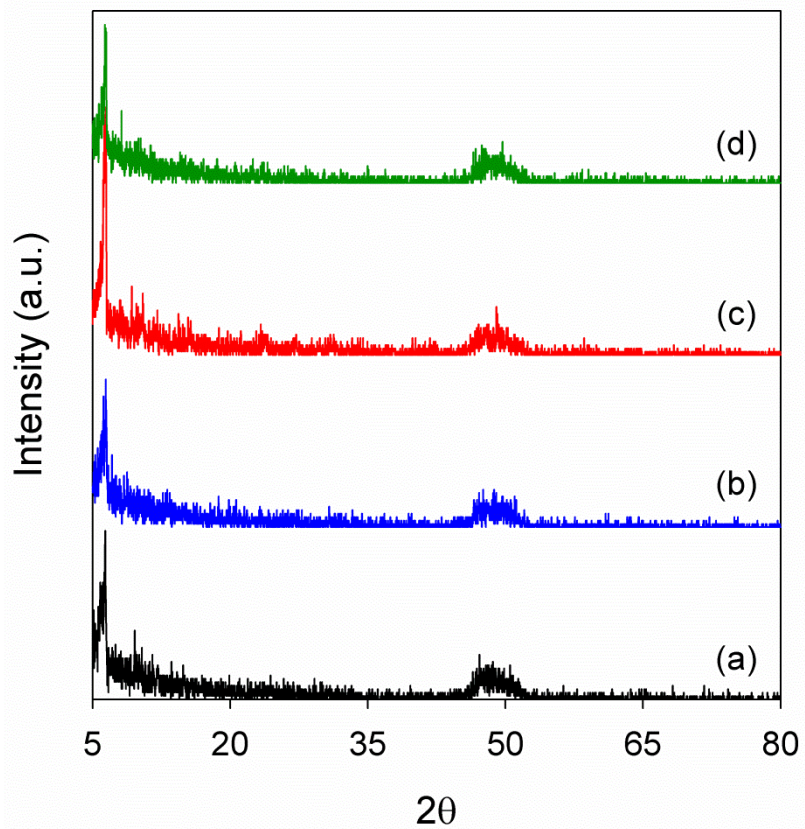
Figure 38. XRD patterns of bare 13X (a), Ag(1.0%)/13X (b), Ag(1.5%)/13X (c), and Ag-Fe(1.0-0.7%)/13X (d).
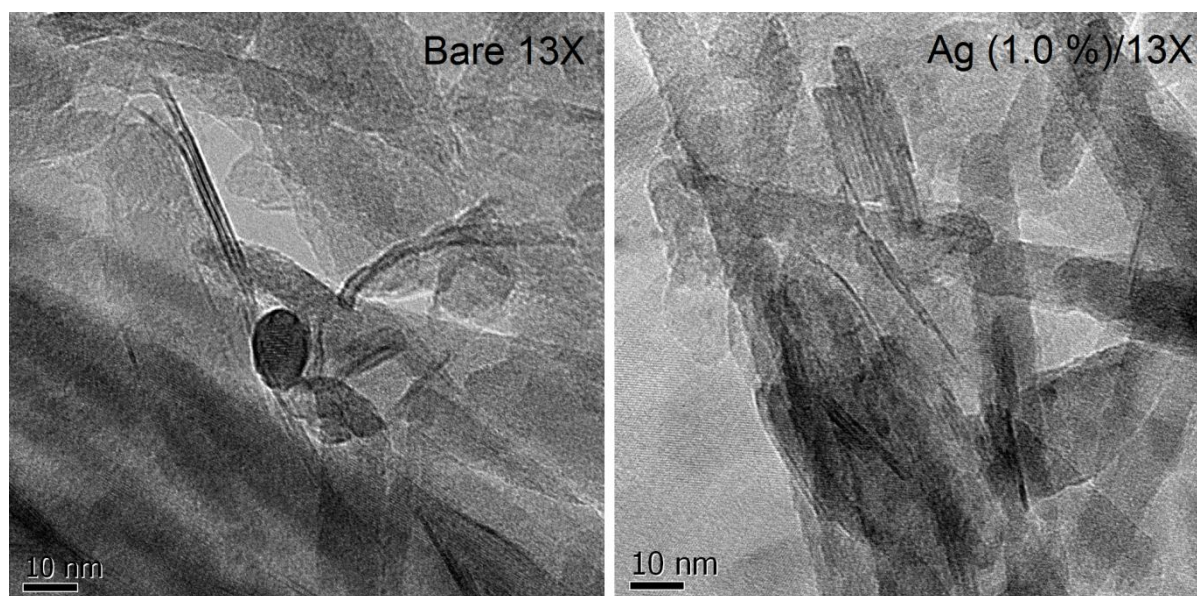
Figure 39. TEM images of the bare 13X and Ag(1.0 %)/13X.
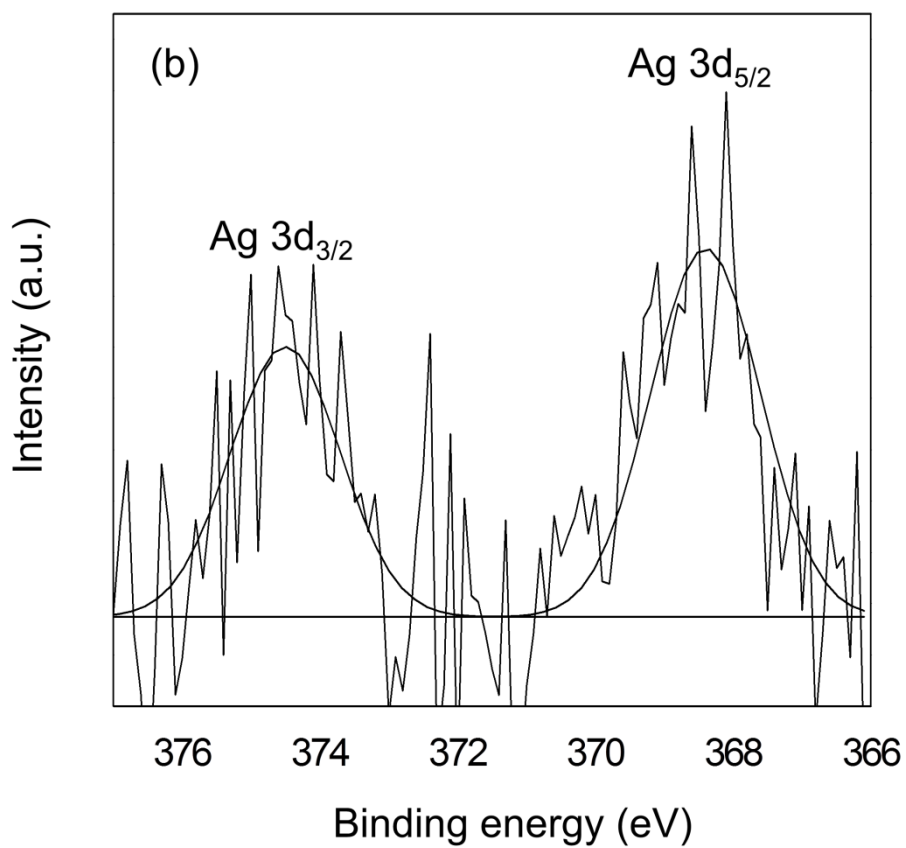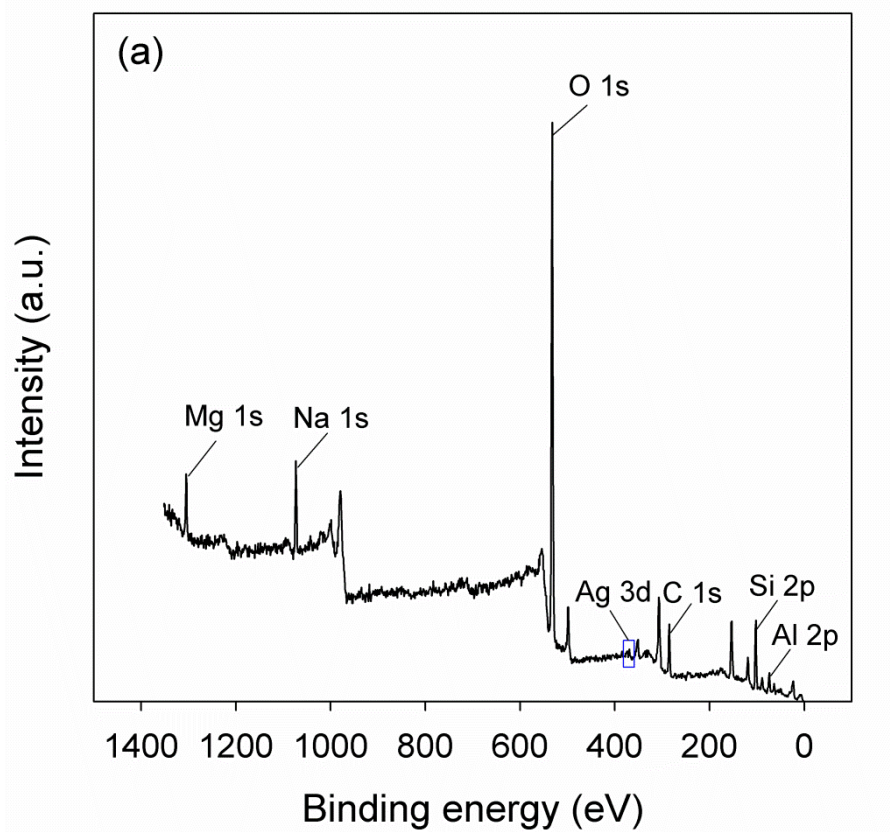
Figure 40. XPS survey spectrum for Ag(1.0 %)13X (a) and high resolution spectrum for Ag3d (b).

Figure 40 shows the XPS survey and Ag 3d spectra of Ag(1.0 %)/13X sample. Fig. 40(a) indicates that beside zeolite framework elements (Si, Al and O), Ag, Na and Mg were also present in the parent 13X, in which, Na^+ was the charged-compensating ion. The XPS high resolution spectrum for Ag 3d is shown in Fig. 40(b). Although intensities of Ag 3d peaks were relatively weak due to the low content of silver loading, appearances of one peak at binding energy (BE) of 368.1 eV for Ag $3d_{5/2}$ and another at BE of 374.1 eV for Ag $3d_{3/2}$ can be recognized, indicating the existence of highly dispersed Ag(I) species in zeolite matrix, in line with earlier report [137]. The formation of metallic silver species is expected to be negligible because oxygen available in ambient air could hinder the auto-reduction of Ag^+ ions during the calcination of the samples.

The XPS data for Ag-M(1.0-0.7)/13X samples (M: Co, Cu, Mn and Fe) are shown in Table 6. The coexistence of M and Ag in 13X framework led to slight increases in the Ag 3d binding energies compared to those of Ag/13X. This is interpreted by the fact that the addition of transition metals resulted in strong mutual effects among M, Ag and 13X, which decreased the surrounding electron cloud density about Ag, therefore increasing the binding energy [138].

Table 6. The XPS analysis data for Ag (1.0 %)/13X and Ag-M (1.0-0.7 %)/13X

Sample	Peak position (eV)				
	Ag $3d_{5/2}$	Co $2p_{3/2}$	Cu $2p_{3/2}$	Mn $2p_{3/2}$	Fe $2p_{3/2}$
Ag/13X	368.1	-	-	-	-
Ag-Co/13X	368.8	781.2	-	-	-
Ag-Cu/13X	368.4	-	933.3	-	-
Ag-Mn/13X	368.3	-	-	641.6	-
Ag-Fe/13X	368.3	-	-	-	712.8

As seen from Table 6, the binding energy of Fe $2p_{3/2}$ was at 712.8 eV, suggesting that Fe species existed in oxidized forms because the Fe $2p_{3/2}$ binding energy of iron metal is at a significant lower value (ca. 707 eV). However, it is not clear that whether Fe^{3+} or both Fe^{2+} and Fe^{3+} were present in zeolite since they have quite the same binding energy. Similar results are also observed with Co, while the Cu $2p_{3/2}$ and Mn $2p_{3/2}$ binding energies at 933.3 and 641.6 eV are assigned to CuO and MnO_2, respectively [139].

3.4.2. Ethylene adsorption on the bare and Ag-coated zeolites
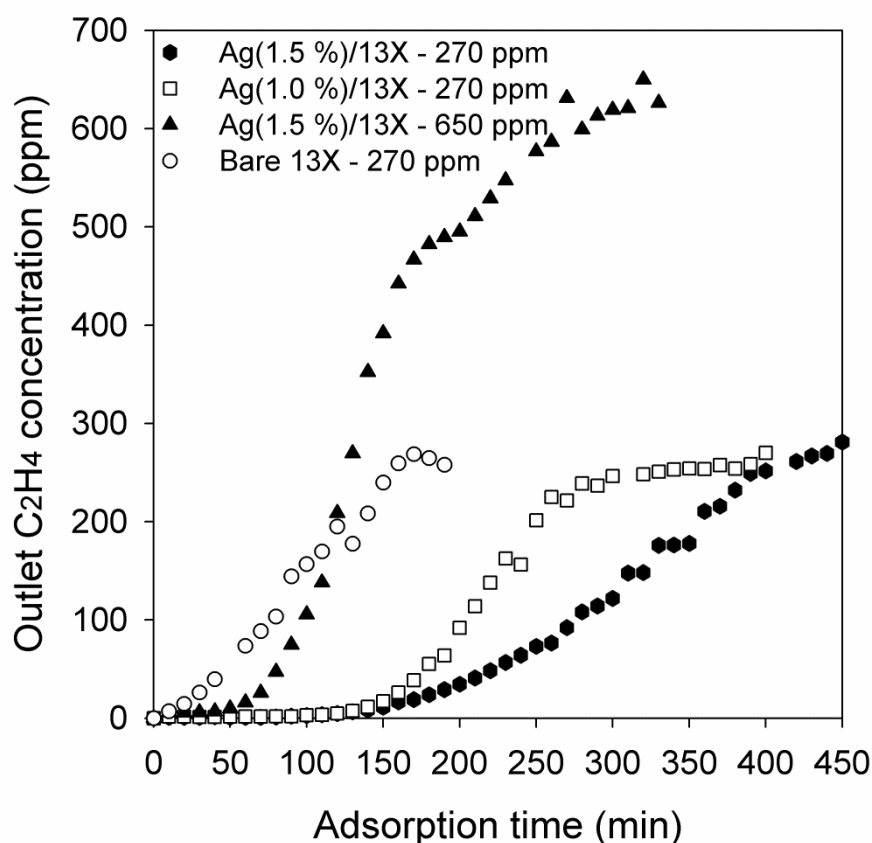
Figure 41. Effects of inlet ethylene concentration and silver loading on adsorption of ethylene (flow rate: 1 L min^{-1}).

First, the ethylene uptake capabilities of the bare and Ag-coated 13X were examined in the packed-bed reactor under dry condition. The Ag loading and ethylene concentration at the reactor inlet were varied from 1.0 to 1.5% and from 270 to 650 ppm, respectively, with the flow rate kept constant at 1 L min^{-1}. As seen from Fig. 41, the parent 13X exhibited a low ability to adsorb ethylene under flowing condition. On the other hand, the adsorption capability was significantly enhanced by incorporating Ag into the zeolite framework. With 1.0 % Ag loading, the dilute ethylene was completely removed from the gas stream for around 100 min. The ethylene adsorption capacity was estimated to be 34.6 and 85.7 µmol g^{-1} for the bare 13X and Ag (1.0%)/13X, respectively. As mentioned above, the interaction between ethylene and adsorbed oxygen plays an important role in the adsorption of ethylene. However, apart from the oxygen-ethylene interaction, the π-complexation between Ag(I) species and ethylene must have been involved in the adsorption process. The metals that can form strong π-complexation bonding are those possessing empty s-orbitals and available electrons in the d-orbitals that are necessary for back donation [140]. The prepared adsorbents contained the well dispersed Ag(I) species, as evident by XPS, with electronic configuration of $1s^2\,2s^2\,2p^6\,3s^2\,3p^6\,4s^2\,3d^{10}\,4p^6\,4d^{10}\,5s^0$, therefore forming strong π-complexes with ethylene molecules. In contrary, our preliminary experiments have shown that ethylene weakly adsorbs on reduced Ag/13X. In other words, the interaction between reduced or metallic silver and ethylene is not sufficient to detain ethylene inside the pores of zeolite at room temperature under flowing condition. Consequently, charged silver species rather than metallic silver were responsible species for the high adsorption capacity. It is evident that the 13X zeolite with unique three-dimensional network of large pores acted as a template for achieving highly dispersive silver rather than directly adsorbed ethylene. The increase in the amount of silver loading from 1.0 to 1.5% slowed down the breakthrough of the adsorbent but did not elongate the complete adsorption time. Meanwhile, the ethylene adsorption capability in terms of complete adsorption time and saturation time significantly

decreased when the initial ethylene concentration increased from 270 to 650 ppm. This result implies that the Ag/13X is suitable for the abatement of dilute ethylene which is usually less than 100 ppm in typical agricultural storage facility.
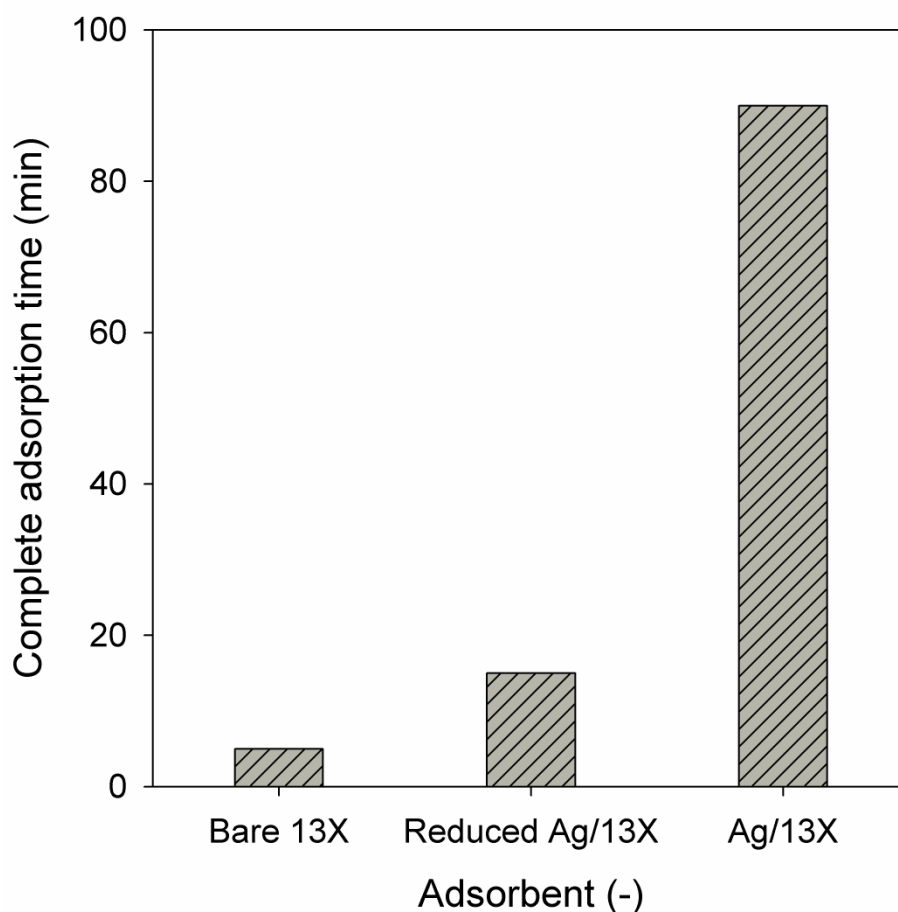
Figure 42. Complete adsorption time for bare zeolite, reduced Ag(1.0 wt%)/zeolite and Ag(1.0 wt%)/zeolite.

For information, the complete ethylene adsorption time with bare 13X, Ag(1.0 %)/13X and reduced Ag (1.0 %)/13X is given in Fig. 42. The complete ethylene adsorption time is defined as time period within which the concentration of ethylene in the outlet gas was less than 1.0 % of that at the inlet. The reduced Ag(1.0 %)/13X was obtained by reduction of

Ag(1.0 %)/13X under H_2(10 v%)/Ar atmosphere at 500 $^{\circ}$C. Adsorption experiments were carried out at room temperature, ethylene concentration of 270 ppm and gas flow rate of 1.0 L min^{-1}.

3.4.3. Adsorption and oxidation of ethylene on Ag (1.0%)/13X and Ag-M (1.0-0.7%)/13X

For comparative assessment of the performance of Ag(1.0 %)/13X and Ag-M(1.0-0.7 %)/13X in the ethylene adsorption and oxidative regeneration of the catalysts under plasma discharge condition, dilute ethylene was first adsorbed on each catalyst for 25 min before being plasma-catalytically oxidized. The initial ethylene concentration and gas flow rate were kept at 650 ppm and 2 L min^{-1}, respectively.
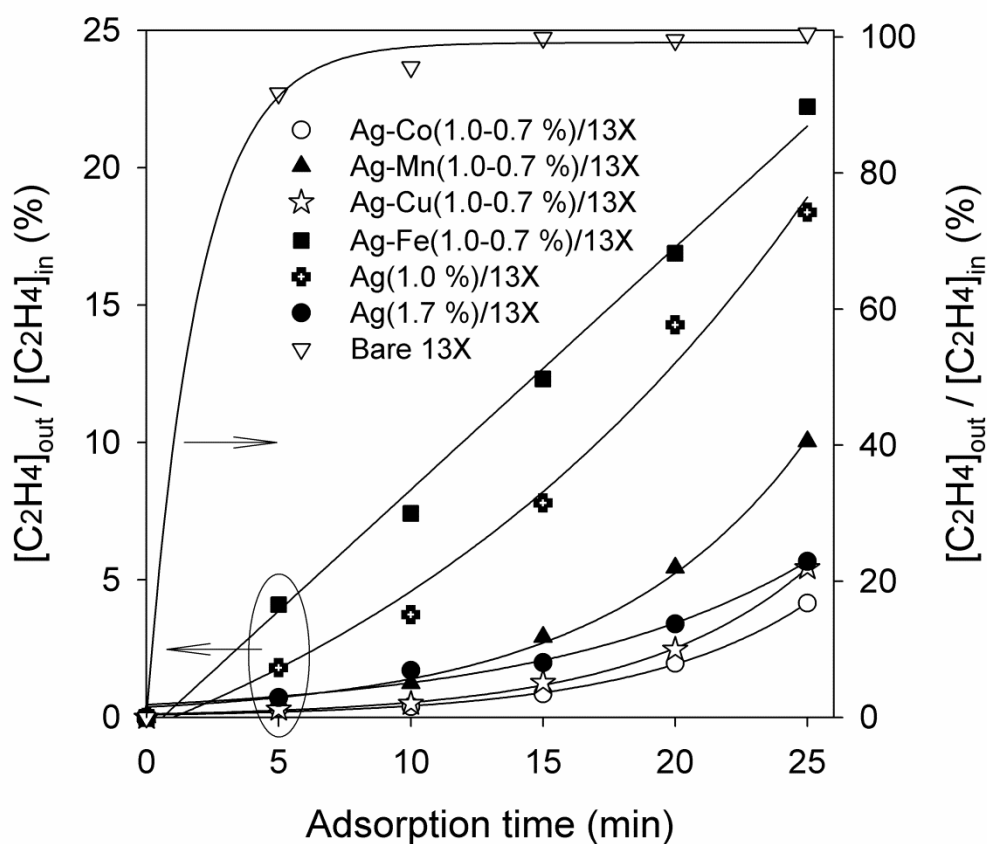
Figure 43. Ethylene adsorption on Ag(1.0 %)/13X and Ag-M(1.0-0.7 %)/13X (gas flow rate: 2 L min^{-1} and inlet ethylene concentration: 650 ppm).

84

Fig. 43 shows the temporal variations of the ethylene concentration at the reactor outlet normalized with respect to the inlet concentration. For comparison, the adsorption curves of the bare 13X and Ag(1.7 %)/13X obtained at the same conditions were also included as the references. As seen, at this flow rate (2.0 L min^{-1}), the breakthrough of Ag(1.0 %)/13X started early without showing complete adsorption, while the bare 13X was almost saturated with ethylene within only 15 min. Except Fe$_x$O$_y$, the addition of transition metal oxides substantially improved the ethylene uptake capacity to be comparable to that of Ag(1.7 %)/13X, obviously due to the new active sites provided by the second metals. Among the bimetallic catalysts, Ag-Co/13X was found to be the best medium for the adsorption of ethylene. It has been reported that unsaturated metal sites such as Cu, Fe, Mn, Co, Ni, and Zn sites in different frameworks undergo π-complexation with olefins [141]. The slight decrease in the ethylene adsorption capability observed with Ag-Fe/13X may be due to the low affinity of Fe species towards ethylene under this high flow rate condition.

Right after the adsorption of ethylene was finished, the contaminated air was shunted off to the ventilation. Instead, ethylene-free air at 2.0 L min^{-1} was fed to the reactor and the plasma was kept switched on for 25 min. The voltage applied to the reactor was 20 kV (peak value). The plasma-catalytic activity of each catalyst was evaluated in terms of ethylene desorption and formation of unwanted byproducts.

Figure 44 shows the time courses of the desorbed ethylene concentration for several zeolite-supported catalysts. Even though the amount of the ethylene desorbed was different from one another, similar tendency in desorption was observed. The concentration of ethylene increased to the maximum value in about 4 min, and then gradually decreased, except Ag-Co/13X showing maximum desorption at about 8 min. The ethylene desorption was the most with Ag-Mn/13X, and the least with Ag-Co/13X. This result may be explained by the strong ethylene adsorption of Ag-Co/13X. Despite the low affinity towards ethylene, Fe$_x$O$_y$ was able to

prevent the ethylene desorption during the plasma-catalytic oxidation stage, which may be attributed to the fast oxidation of the adsorbed ethylene on Ag-Fe/13X.
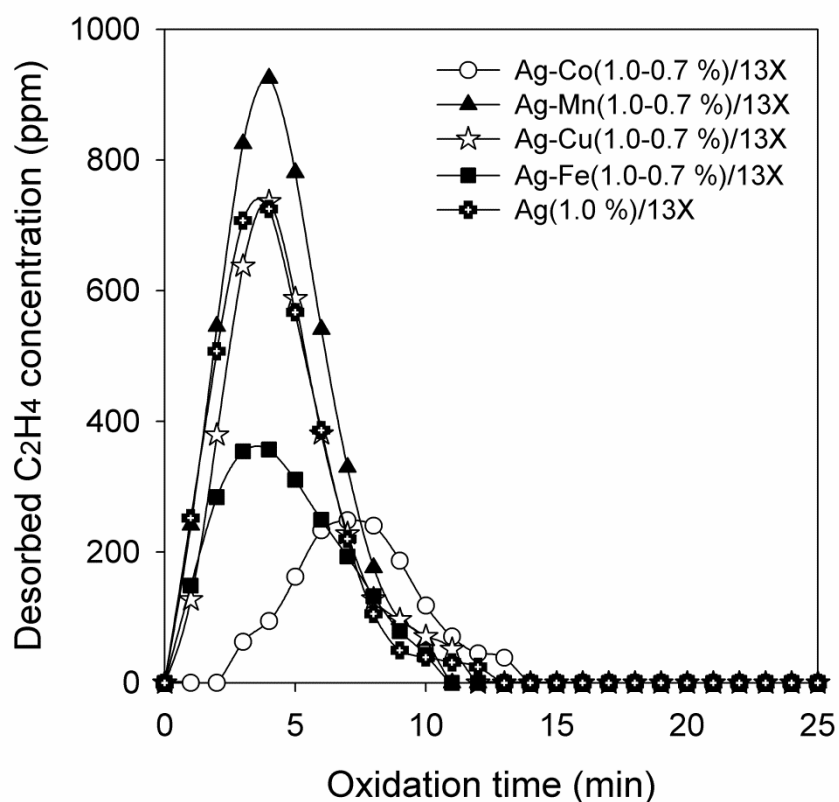
Figure 44. Ethylene desorption during the oxidation of ethylene pre-adsorbed on Ag(1.0%)/13X and Ag-M(1.0-0.7%)/13X (adsorption time: 25 min; applied voltage: 20 kV).

Beside desorbed ethylene, gaseous decomposition byproducts including carbon oxides, methane (CH_4) and formaldehyde (HCHO) were also detected in the effluent. The changes in the concentrations of carbon oxides with the plasma-catalytic oxidation time are shown in Fig. 45. For all the catalysts, CO_2 was the main byproduct. Similar to the evolution trend of the desorbed ethylene, the concentrations of CO and CO_2 first increased to the maxima, and gradually decreased thereafter. Among the catalysts investigated, Ag-Co/13X exhibited the lowest activity for the oxidation of the adsorbed ethylene, thus the lowest and the delayed CO_2 emission peak, while the opposite was true for Ag/13X. The incorporation of Fe_xO_y caused a

slight decrease in the maximum CO_2 concentration; however, the average generation rate of CO_2 was similar to the Ag-alone case.
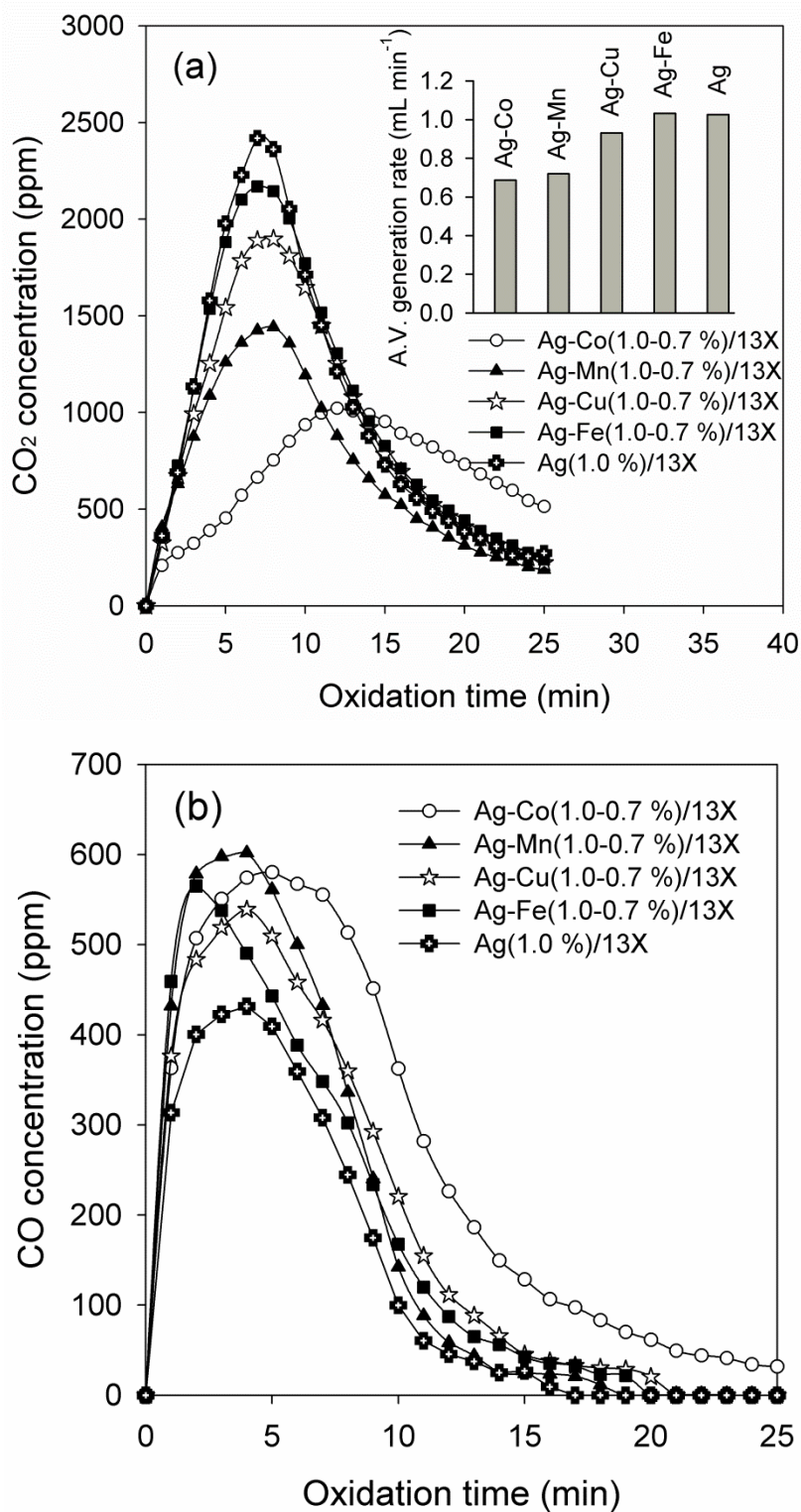
Figure 45. Concentrations of CO_2 (a) and CO (b) during oxidation of ethylene pre-adsorbed on Ag(1.0%)/13X and Ag–M(1.0–0.7%)/13X (adsorption time: 25 min; voltage: 20 kV).

As presented in the inset of Fig. 45(a), the average generation rate of CO_2 during the 25-min oxidation time was in order of Ag ≈ Ag-Fe > Ag-Cu > Ag-Mn > Ag-Co. Compared to CO_2, the production of CO was much lower and followed the reverse order of that of CO_2. It should be noted that the sluggish evolution of CO_2 compared to CO is ascribed to the difference in adsorptivity and the rate of diffusion out of the pores between CO_2 and CO, which was also previously observed on γ-alumina [98]. Generally, the diffusivity of a compound is inversely proportional to its molecular weight. Overall, Ag/13X and Ag-Fe/13X turned out to be the most appropriate for the oxidation of ethylene.

The temporal variations of CH_4 and HCHO concentrations during the plasma-catalytic oxidation are shown in Fig. 46. These compounds were produced as the minor byproducts whose concentrations did not exceed 40 ppm. The emission of CH_4 was the least with Ag-Fe/13X and Ag-Co/13X, while the formation of HCHO was not much different between the catalysts. The collation of Figs. 44 and 46 show that there is a clear correlation in the evolution of CH_4 with the desorbed C_2H_4. This result implies that the formation of this mono-carbon byproduct was favored in the gas phase within the zeolite macro-pores and inter-pellet spaces where the energetic electrons and short-lived active species were available. According to R. Aerts et al. [48], the decomposition of ethylene in the gas phase is initiated mainly by the radical and metastable ($O^{\bullet}$ and $N_2(A^3\Sigma_u^+)$) destructions of ethylene molecules, leading to the formation of CH_3, CH_2 and H species through following reactions [48,142]:

$$C_2H_4 + N_2(A^3\Sigma_u^+) \rightarrow C_2H_3 + H + N_2 \tag{R 50}$$

$$C_2H_4 + O \rightarrow CHO + CH_3 \tag{R 51}$$

$$C_2H_4 + O \rightarrow CH_2O + CH_2 \tag{R 52}$$

$$C_2H_3 + O \rightarrow CO + CH_3 \tag{R 53}$$
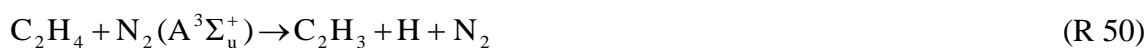
CH_4 was likely formed by the combination of the CH_3 and H.
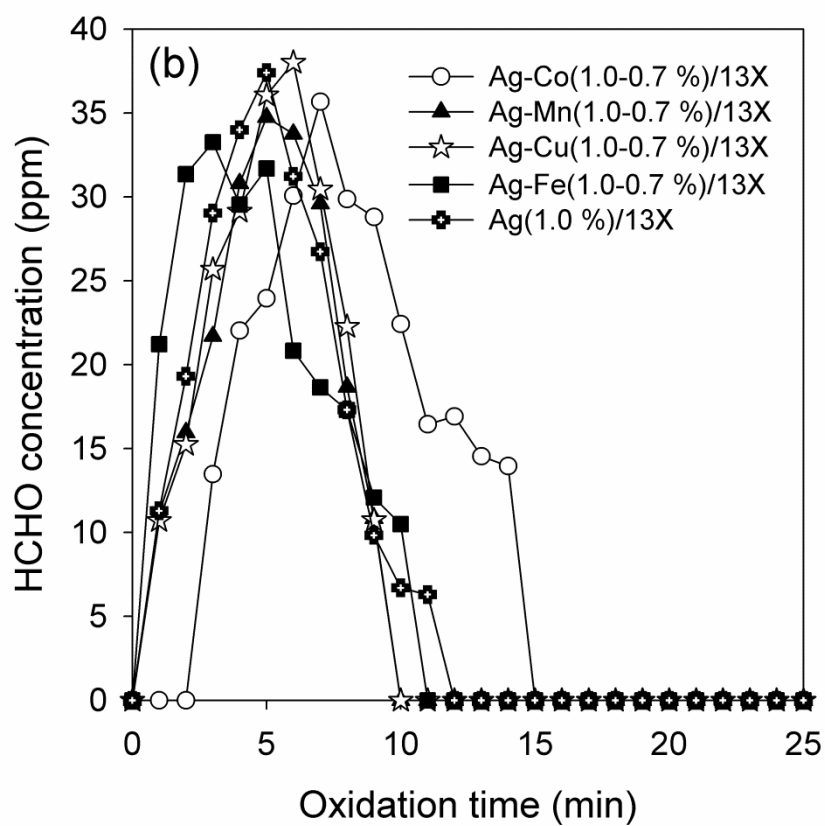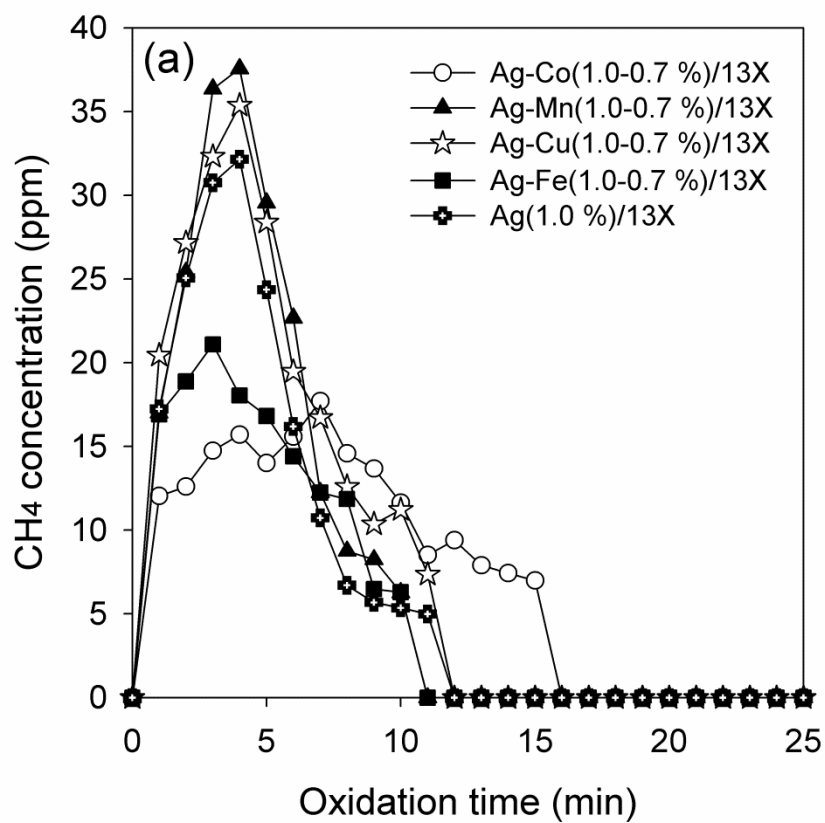
Figure 46. Concentrations of CH_4 (a) and HCHO (b) during oxidation of ethylene pre-adsorbed

on Ag(1.0%)/13X and Ag-M(1.0-0.7%)/13X (adsorption time: 25 min; applied voltage: 20 kV).

The role of electrons in the direct destruction of ethylene can be neglected [142], because electrons cannot possibly be accelerated to gain enough energy in a short distance of travel in zeolite micro-pores where ethylene was captured. The free path of electrons required to rupture the C=C bond in ethylene can be estimated by assuming that electric filed is uniformly distributed across the electrodes. By equating the electric force acting on an electron for a constant electric field (E) to Newton's second law, we obtain:

$$a = \frac{eE}{m_e} \qquad\qquad (E\ 7)$$

where e is electron charge ($=1.6\times10^{-19}$ C) and m_e is the mass of an electron ($=9.1\times10^{-31}$ kg). Since the applied voltage and discharge gap are 2×10^4 V and 10 mm, respectively, the average electric field is calculated to be 2×10^3 V mm^{-1}, and the acceleration is 3.52×10^{17} m^2 s^{-1}. The strength of C-H bond in ethylene is 4.77 eV [143], and electrons having kinetic energy (E_k) larger than 4.77 eV can break the bond, i.e., the electron velocity (v_e) should be larger than the value calculated by the following equation:

$$v_e = \sqrt{\frac{2E_k}{m_e}} = 1.3\times10^6\,\text{m/s} \qquad\qquad (E\ 8)$$

The velocity of an electron is equal to its initial velocity added to its acceleration (a) multiplied by time of travel (t). If the initial velocity is taken to be zero,

$$v_e = at \qquad\qquad (E\ 9)$$

The displacement (h) is equivalent to

$$h = \frac{1}{2}at^2 \qquad\qquad (E\ 10)$$

By combining (E 9) and (E 10), the free path required for an electron to be accelerated enough to break the bond is calculated to be 2.4 x 10^{-6} m (=2.4 μm). However, the inner diameter of the zeolite super-cages amounts to only 0.9 nm [144], which is far smaller than the free path required for the electrons to gain sufficient energy. Consequently, the formation and diffusion

into the zeolite micro-channels of the long-lived oxidizing species, namely, ozone, are crucial for the removal of the adsorbed ethylene.
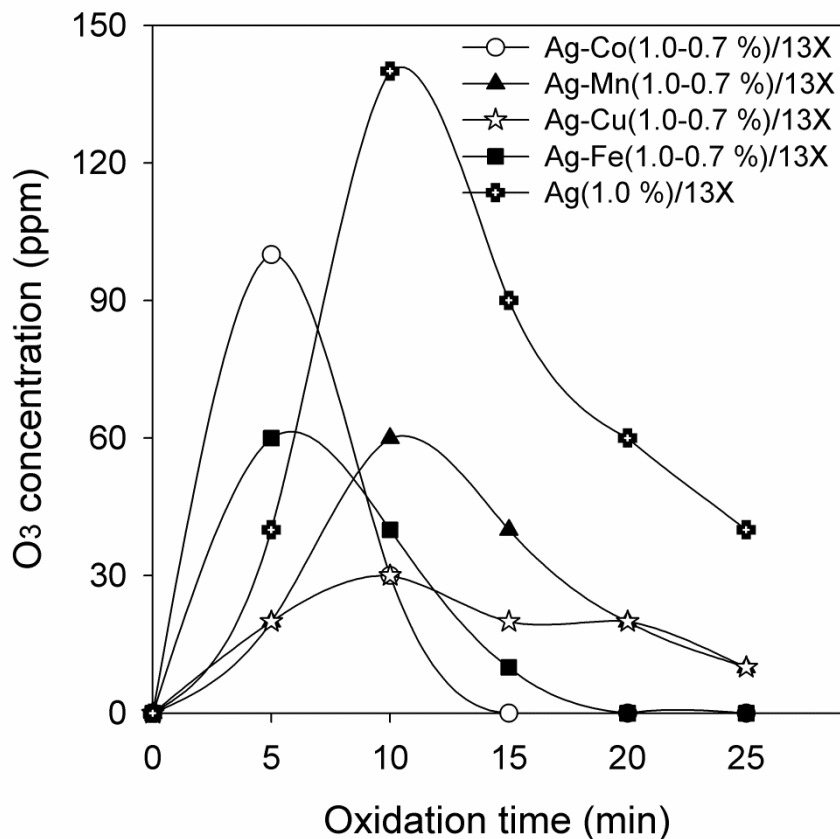
Figure 47. Concentration of residual ozone during oxidation of ethylene pre-adsorbed on Ag(1.0%)/13X and Ag-M(1.0-0.7%)/13X (adsorption time: 25 min; applied voltage: 20 kV).

The concentrations of residual ozone at the downstream of the reactor during the plasma-catalytic oxidation are shown in Fig. 47. The emission of ozone tended to increase in the early stage as the depletion of the adsorbed ethylene proceeded. After that, the emission of ozone showed a decreasing trend as time going for all the catalysts, obviously due to the increase in the reactor temperature up to around 135 ^{o}C after 25-min plasma discharge. For information, the temporal evolution of the reactor temperature with different catalysts was given in Fig. 48.
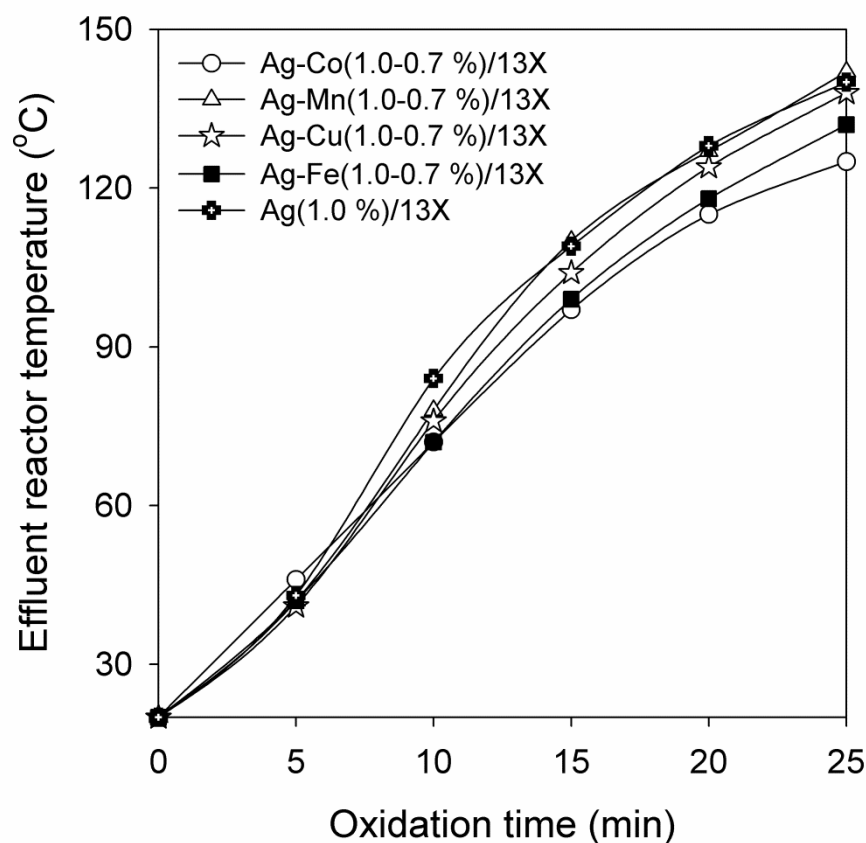
Figure 48. Effluent reactor temperature with different catalysts (applied voltage 20 kV).

It is thought that most of the ozone generated during the plasma-catalytic oxidation step was consumed to oxidize the adsorbed ethylene, but it should be noted that the desorbed ethylene could directly react with ozone in the gas phase [90]. Among the catalysts tested, Ag/13X showed the highest ozone emission with the maximum of 140 ppm at 10 min, and it was still retained at 40 ppm at the end of the plasma-catalytic oxidation step. On the contrary, the concentration of ozone obtained with Ag-Co/13X was much lower, decreasing to zero at 15 min.

For the investigation on the relationship between the generation of ozone and oxidation of adsorbed ethylene, the consumption of ozone by the desorbed ethylene should be avoided. Thus, the variations in the concentration of ozone were evaluated without pre-adsorption of ethylene.
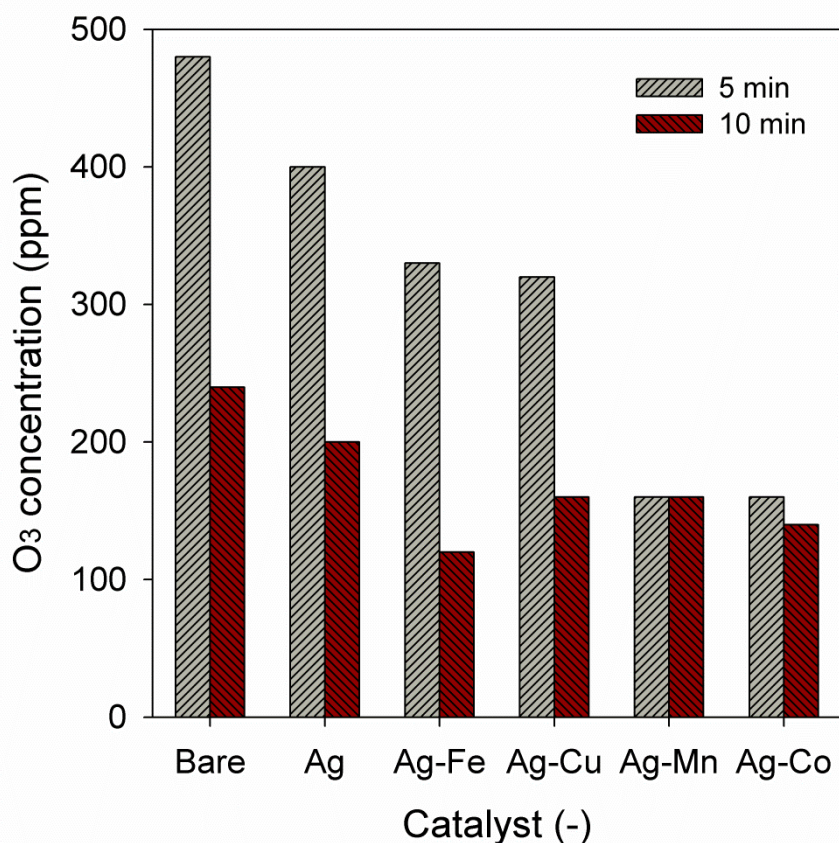
Figure 49. Residual ozone concentrations of Ag(1.0%)/13X and Ag-M(1.0-0.7%)/13X without

pre-adsorption of ethylene (applied voltage: 20 kV).

As shown above, carbon oxides were mostly produced within the first 10 min of the plasma-catalytic oxidation step, except Ag-Co/13X, suggesting that the ozone produced during this period was crucial to the removal of the adsorbed ethylene. For this reason, the concentrations of ozone were measured at 5 and 10 min after the plasma discharge started, without pre-adsorption of ethylene, which is summarized in Fig. 49. The temperatures of the reactor measured at 5 and 10 min were ca. 43 and ca. 76 ^{o}C, respectively. In general, the presence of metals in zeolite framework causes a decrease in the ozone production. Among the catalysts, Ag/13X showed the highest ozone concentration at 5 min, while those obtained with Ag-Fe/13X and Ag-Cu/13X were slightly lower. Particularly, the co-introduction of silver and manganese

or cobalt into the zeolite considerably suppressed the formation of ozone. This result is well correlated with the results in Fig. 45 where higher CO_2 concentrations were observed with Ag/13X, Ag-Fe/13X and Ag-Cu/13X than with Ag-Mn/13X and Ag-Co/13X. In addition, the concentrations of ozone obtained with Ag-Mn/13X and Ag-Co/13X hardly depended on the discharge time and therefore on the reactor temperature, obviously due to their high activity for ozone decomposition even at room temperature. The supported manganese and cobalt oxides have been reported to be excellent ozone decomposition catalysts [81,145]. It is believed that most of ozone generated by the plasma was destroyed on these metal oxides existing on the outer surface of the zeolite pellets and in the zeolite macro-pores before reaching the micro-pores. As discussed above, the ozone diffusion deep inside the zeolite pellets where most of ethylene is trapped plays a crucial role in the removal of the adsorbed ethylene. In this sense, it is natural that the use of a metal oxide with high ozone decomposition activity should decrease the formation of CO_2. In comparison, the concentrations of ozone obtained with Ag/13X, Ag-Fe/13X and Ag-Cu/13X having low ozone decomposition activities at room temperature rapidly decreased to nearly half with time due to the increase in the reactor temperature.

Here it should be emphasized that the concentration of ozone is not the only factor affecting the plasma-catalytic oxidation of the adsorbed ethylene. Indeed, the oxidation of ethylene also largely depended on the oxidation activity of catalysts. As shown in Fig. 49, the concentrations of ozone obtained with Ag-Fe/13X and Ag-Cu/13X were similar to each other, and this is the case for Ag-Mn/13X and Ag-Co/13X. Despite the similar concentration of ozone, significant discrepancy in the evolution of CO_2 was observed between these catalysts. Compared to Ag/13X, Ag-Fe/13X was able to retain high ethylene conversion to CO_2 while reducing the concentration of ozone, which suggests that Fe_xO_y had a positive catalytic effect on the oxidation of the adsorbed ethylene. On the other hand, the presences of other remaining transition metals were found to decrease the mineralization of the adsorbed ethylene to CO_2.

These observations are consistent with the previous study [78], in which it is reported that the catalytic activity of a transition metal oxide is closely related to its formation enthalpy. In the same paper, it is shown that Fe_2O_3 is the most desirable catalyst for plasma-catalytic oxidation of diesel particulate matters among TiO_2, ZnO, V_2O_5, Fe_2O_3, MnO_2, Co_3O_4 and CuO whose formation enthalpies per oxygen atom are -469.9, -348.3, -310.1, -274.7, -260.0, -222.8, and -157.3 kJ g-O_{atom}^{-1}, respectively. The moderate formation enthalpy of F_2O_3 results in a balance between the oxidation and reduction in the redox catalytic cycle, which is responsible for the high oxidation activity.

3.4.4. Adsorption and oxidation of ethylene on Ag-Fe(1.5-0.5 %)/13X
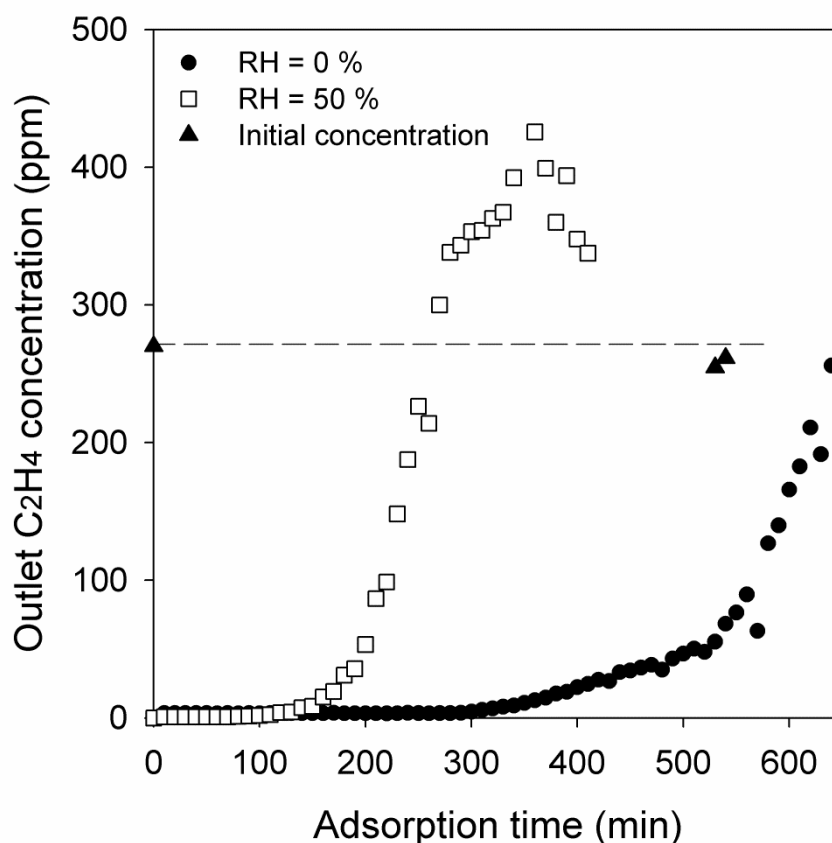
Figure 50. Effect of humidity on ethylene adsorption over Ag-Fe(1.5-0.5 %)/13X (gas flow rate: 1 L min^{-1}; inlet ethylene concentration: 270 ppm).

Taking its high ethylene oxidation rate and low ozone emission into account, Ag-Fe/13X was chosen as the catalyst for further investigation. The amount of Ag-Fe/13X packed in the reactor was 45 g, and the Ag and Fe loadings were 1.5 and 0.5%, respectively. The discharge length corresponding to 45 g of the catalyst was about 150 mm.

The effect of humidity on the dynamic adsorption of ethylene on Ag-Fe(1.5-0.5 %)/13X is shown in Fig. 50. As can be seen, the complete adsorption time and saturation time remarkably decreased when water vapor coexisted at 50 % relative humidity, which is obviously due to the competition of water with ethylene for the adsorption sites. Unexpectedly, the outlet concentration of ethylene increased beyond the inlet concentration after 260 min and then started to decease at about 360 min. The inlet concentration of ethylene was then re-checked at 530 and 540 min. The reason behind this unusual behavior can be explained by the replacement of the adsorbed ethylene by water that is a stronger adsorbate.

In the cyclic treatment, the duration of the plasma-catalytic oxidation step required to remove the adsorbed ethylene necessarily depends on the previous adsorption step, i.e., the more the amount of the ethylene adsorbed, the longer the plasma-catalytic oxidation duration required. Besides, the plasma-catalytic oxidation duration also depends on the applied voltage.

The effect of the applied voltage and adsorption time on the plasma-catalytic oxidation stage was investigated under dry condition. The voltage was varied from 15 to 17 kV, and the adsorption time from 60 to 180 min. The gas flow rate and inlet ethylene concentration were kept at 1.0 L min^{-1} and 270 ppm, respectively. During the adsorption step, the amount of ethylene adsorbed for 60 min was estimated to be 662.2 μmol (or 16.2 mL at 25 ^{o}C and 1.0 atm) and that for 180 min was 1986.6 μmol (or 48.6 mL at 25°C and 1.0 atm).
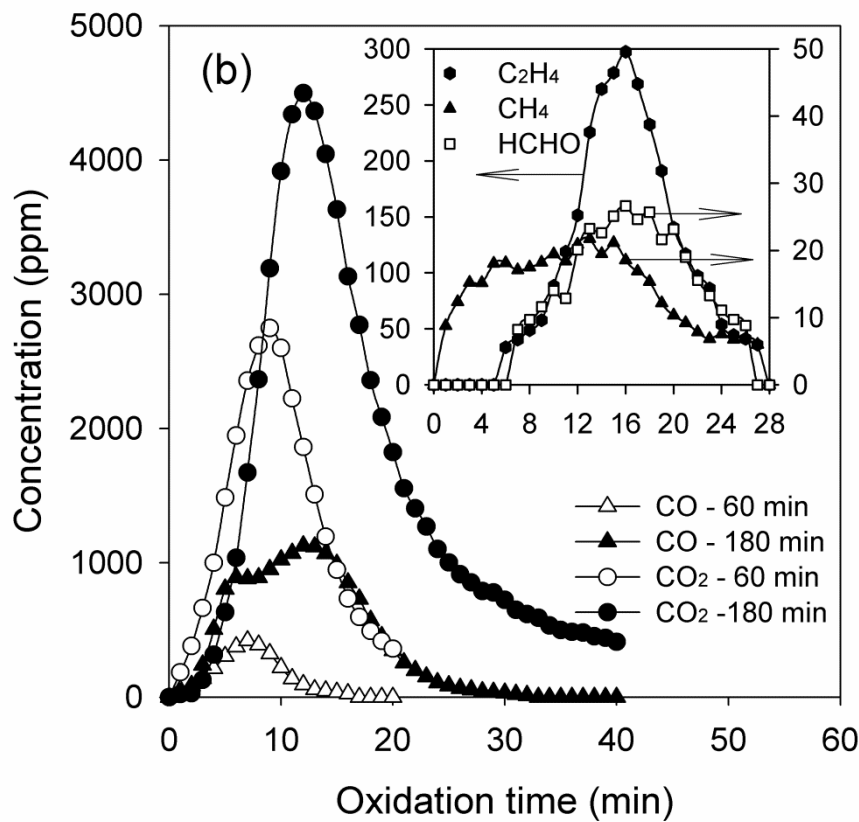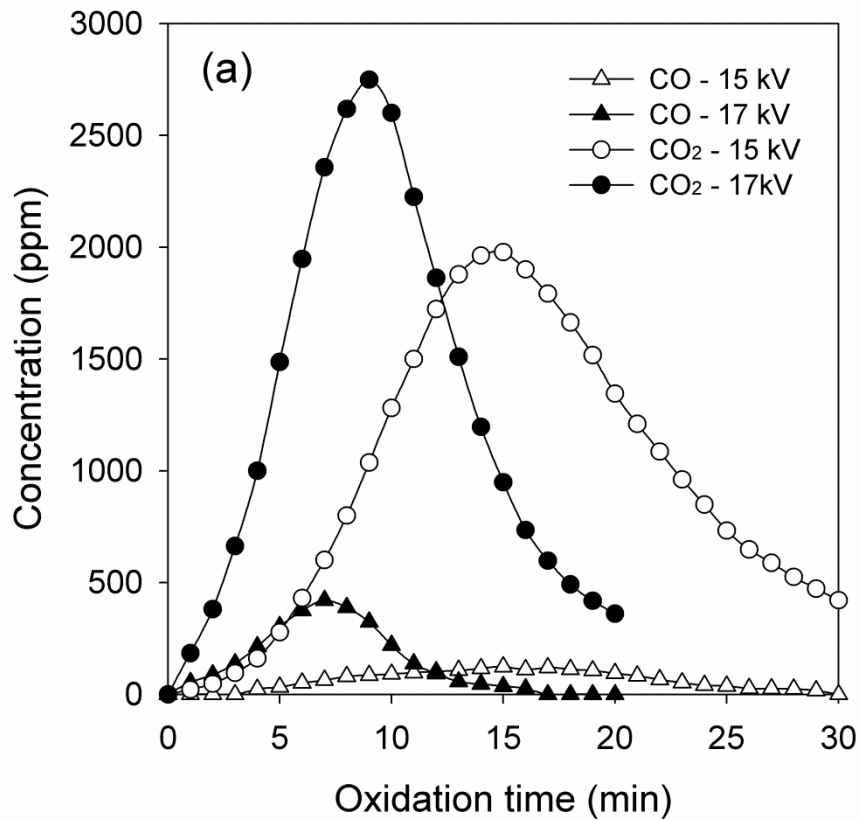
Figure 51. Effect of applied voltage (a) and adsorption time (b) on product formation with Ag-Fe(1.5-0.5%)/13X catalyst (gas flow rate: 1.0 L min^{-1}; inlet ethylene concentration: 270 ppm).

Fig. 51 shows the concentrations of the products produced and the ethylene desorbed during the plasma-catalytic oxidation. When the adsorption time was 60 min, the desorption of ethylene and formation of CH_4 and HCHO were not observed by FTIR. Only carbon oxides were detected. The result in Fig. 51(a) shows that an increase in the applied voltage decreased the time required to oxidize the adsorbed ethylene. As aforementioned, the long desorption time of CO_2 was attributed to its high adsorptivity. In that case, the time that the evolution of CO ends can be used as a measure for the oxidation time required to remove all the adsorbed ethylene. As expected, the time required to remove the adsorbed ethylene largely decreased from 30 to 17 min with increasing the applied voltage from 15 to 17 kV. In addition, the maximum concentrations of CO and CO_2 were higher at higher applied voltage, reaching their peaks earlier. This result is because more electrical energy was delivered to the reactor at higher voltage, facilitating the formation of reactive species such as ozone. As shown in Fig. 51(b), an increase in the adsorption time from 60 to 180 min while keeping the applied voltage at 17 kV caused the desorption of ethylene accompanying with the formation of CH_4 and HCHO. Besides, prolonging the adsorption time resulted in longer plasma-catalytic time required for the removal of the adsorbed ethylene. The time that the evolution of CO ended was delayed from 17 to 33 min when the adsorption time was tripled. It is noteworthy that the threefold increase in the adsorption time from 60 to 180 min increased the required plasma-catalytic time only twice. In other words, the energy efficiency for the removal of ethylene increased when the adsorption time was increased. In fact, the adsorption can last much longer since the ethylene concentration in real situations such as agricultural storage facility is far lower than the value of this work. The discharge power corresponding to 17 kV was determined to be 19 W. Based on this discharge power, it was found that the energy yield for oxidizing the adsorbed ethylene decreased from 34.4 to 24.4 J μmol^{-1} when the adsorption time was tripled. However, longer adsorption duration produced more CO and other undesirable byproducts like CH_4 and HCHO. As well, the CO_2

selectivity largely decreased from 8.9 to 2.8 with increasing the adsorption time from 60 to 180 min. Moreover, the global fraction of the adsorbed ethylene converted into gaseous compounds including desorbed ethylene also slightly decreased from 90 to 87 %. In which, the fraction of adsorbed ethylene transformed to CO_x (CO and CO_2) was evaluated to be 90 and 80 % with 60 and 180 min of adsorption, respectively.
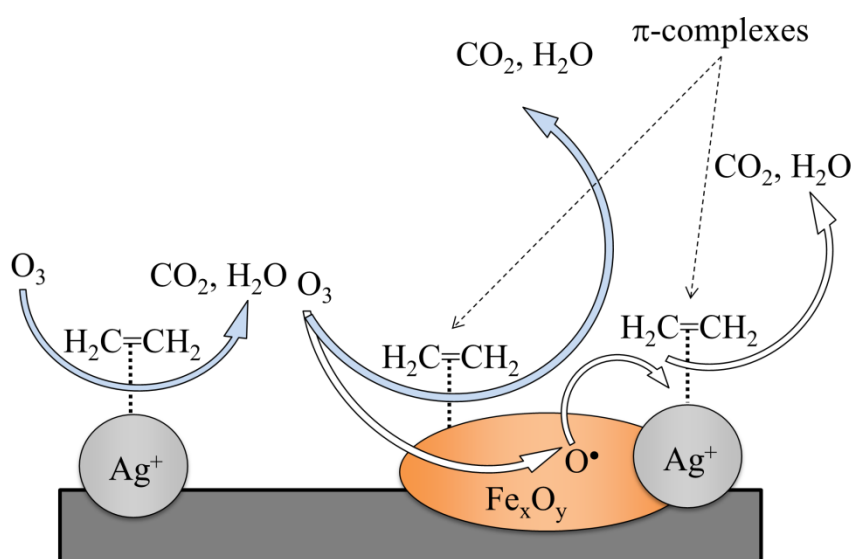
Figure 52. Schematic diagram of ethylene adsorption and oxidation on Ag-Fe/13X catalyst.

The adsorption and oxidation of ethylene on Ag-Fe/13X is schematically shown in Fig. 52. Owing to the fully filled d orbitals, Ag(I) species can strongly adsorb C_2H_4 and weaken the C=C bond strength by the π back-donation effect and therefore facilitate the oxidation of adsorbed ethylene. It has been well recognized that in the course of oxidation, the mobile atomic oxygen is transferred from the surface of transition metal oxides to silver through the silver/metal oxide interface, leading to an increase in the total amount of active atomic oxygen [146]. The spillover of oxygen may compensate the decrease in ozone concentration, allowing

high oxidation rate of the adsorbed ethylene. During the oxidation, the active oxygen on the surface of Fe_xO_y can be supplemented by ozone decomposition.

In summary, the dynamic adsorption of ethylene on 13X zeolite-supported Ag and Ag-M_xO_y (M: Co, Cu, Mn, and Fe), and plasma-catalytic oxidation of the adsorbed ethylene are investigated in this section. The experimental results show that the incorporation of Ag into zeolite affords a marked enhancement in the adsorptivity for ethylene. The addition of transition metal oxides is found to have a positive influence on the ethylene adsorption, except Fe_xO_y. The presence of the additional metal oxides, however, appeares to somewhat interrupt the diffusion of ozone (the most abundant oxidizing species generated by plasma) into the zeolite micro-pores, leading to a decrease in the plasma-catalytic oxidation efficiency of the ethylene adsorbed there. Among the second additional metal oxides, Fe_xO_y is able to reduce the emission of ozone during the plasma-catalytic oxidation stage while keeping a high effectiveness for the oxidative removal of the adsorbed ethylene. The periodical treatment consisting of a long adsorption time for enriching dilute ethylene followed by a short plasma-catalytic oxidation time may be a promising energy-efficient ethylene abatement method.

------------------------o0o------------------------

In order to further enhance the energy efficiency of the cyclic treatment, the effects of other factors such as adsorbent preparation and reactor configuration are under further investigation. Impregnation and ion exchange are commonly used techniques to alter the physicochemical properties of zeolite, differently affecting the nature and dispersion of the active component and thereby the VOC adsorption capability. Meanwhile, the reactor configuration will strongly influence the interaction between NTP and catalyst, generation of reactive species, and energy consumption.

3.5. Effect of the adsorbent/catalyst preparation method and plasma reactor configuration on the removal of dilute ethylene from air stream

3.5.1. Characterization of adsorbent/catalysts

The BET surface areas of the parent and silver modified 13X zeolites are presented in Table 7. As seen, the surface area was mainly contributed by the micropores (ca. 97 %), and it decreased by 10.2 and 5.5 % after the impregnation and ion exchange, respectively. The more significant decrease in the micropore surface area observed with Ag-IM/13X is attributed to the reduction in the accessibility to micropores by the formation of large silver clusters and particles that partially blocked the pores [147].

Table 7. Surface areas of parent 13X, Ag-IM/13X and Ag-EX/13X.

Sample	Total surface area $(m^2\ g^{-1})$	Micropore surface area $(m^2\ g^{-1})$	External surface area $(m^2\ g^{-1})$
Parent 13X	736.9	715.3	21.6
Ag-IM/13X	664.7	642.5	22.2
Ag-EX/13X	699.6	675.9	23.7

The powder XRD patterns of the parent and silver modified 13X zeolites are shown in Fig. 53. The incorporation of silver by either ion exchange or impregnation did not lead to the

appearance of any new peak corresponding to bulky metal or oxide aggregates of silver, indicating good dispersions of active component on the support. This is understandable from the high surface area of zeolite and low metal loading.
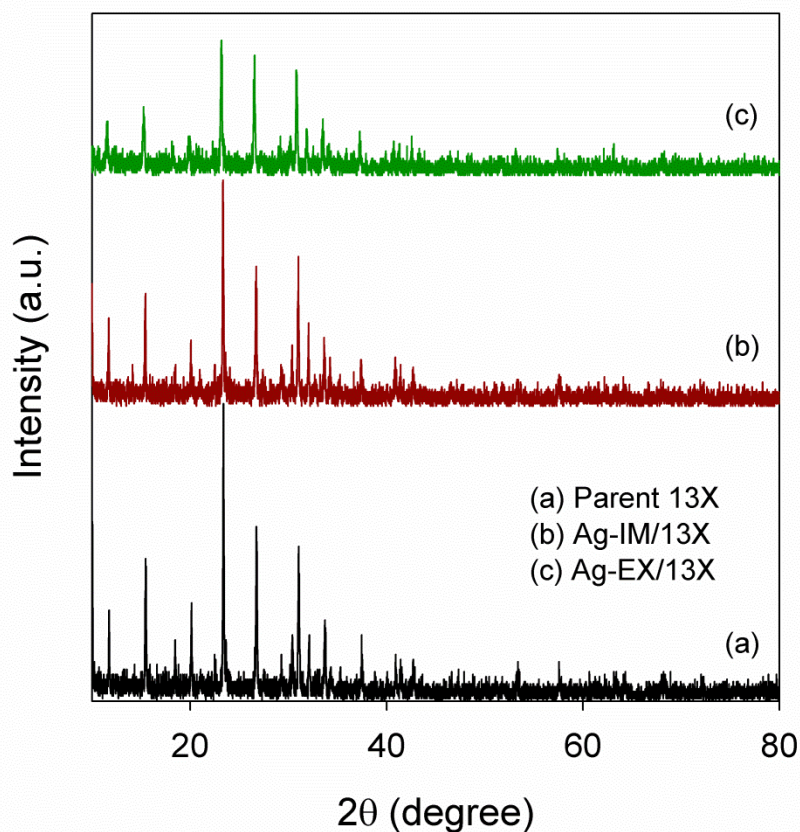
Figure 53. The XRD patterns of the parent 13X (a), Ag-IM13X (b) and Ag-EX13X (c).

All main peaks of the parent 13X were also present in the spectra of silver-loaded 13X samples, suggesting that the structure of 13X was preserved after incorporating silver into the zeolite matrix. However, a decrease in the diffraction peak intensity and therefore a loss of crystallinity were observed for both Ag-EX/13X and Ag-IM/13X, revealing the presence of metal species in the cavities and/or surface of zeolite support. This behavior was also observed in previous reports [147,148]. The reduction of XRD peak intensity was found to be more significant with

the ion-exchanged sample than the impregnated one, probably due to the partial dealumination of 13X during the long-time exchange process [149].

3.5.2. Ethylene adsorption capacities of Ag incorporated zeolites

The ethylene adsorption capability of the zeolite modified with silver was investigated in terms of complete adsorption time at room temperature without plasma ignition.
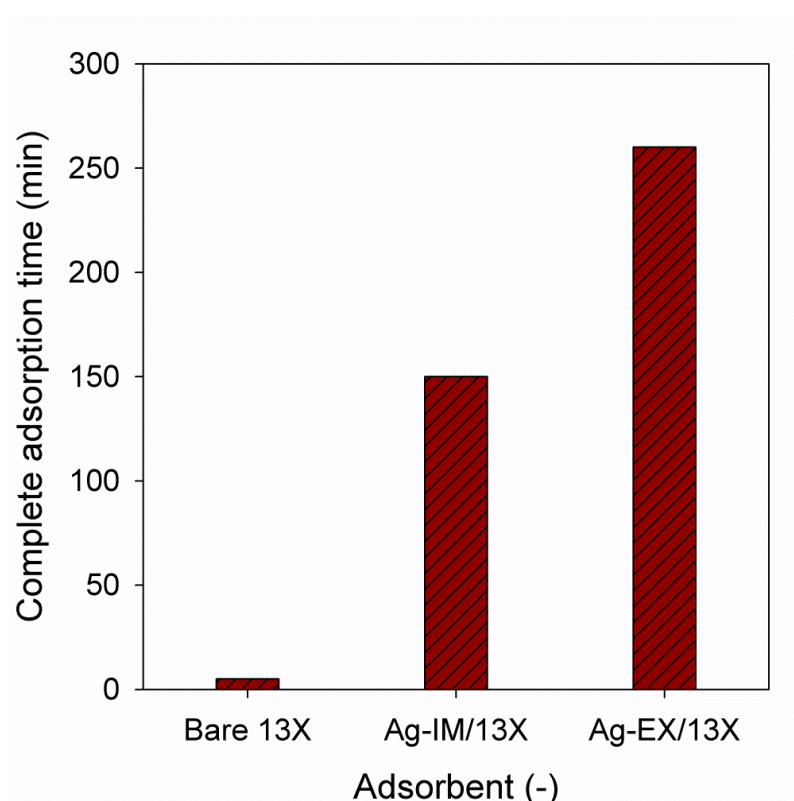
Figure 54. The complete ethylene adsorption time by Ag-IM13X and Ag-EX13X.

As aforementioned in section 3.4.2, the complete adsorption time was defined as the time period for which the outlet ethylene concentration was less than 1.0 % of the inlet concentration. From Fig. 54, the bare 13X zeolite exhibited a low ethylene adsorption capability as the adsorbate was completely detained in it within only 5 min. It has been known that the interaction of charge-compensating cation with ethylene double bond is responsible for the adsorption of ethylene on

zeolites [106]. In case of the parent 13X, ethylene is adsorbed via electrostatic interaction with Na^+ ions present in zeolite framework. This physical adsorption is weak and reversible, not sufficient to detain ethylene inside the pores of zeolite under flowing condition at atmospheric pressure and room temperature. By incorporating silver into zeolite framework, the complete adsorption time drastically increased up to 150 and 260 min corresponding to 1226.2 and 2125.5 µmol of adsorbed ethylene at 25 ^{o}C and 1.0 atm for Ag-IM/13X and Ag-EX/13X, respectively. This result evidenced that new active sites for the adsorption of ethylene were formed simply by introducing Ag species into the zeolite matrix. As previously interpreted in section 3.4.2, the formation of π-complexes of Ag species with ethylene molecules was likely responsible for the high ethylene uptake by the Ag-incorporated 13X zeolites and for the immobilization of the olefin in the micropores of the zeolite. In this sense, a fine dispersion of silver particles in zeolite matrix is important to increase the formation of such π-complexes. The oxides of silver and other transition metals have been reported to form strong π-complexation bonds with olefins through the donation of olefin π-bond electrons to the empty s-orbital of the metal and the d-π* back donation [141,150–153]. Metallic silver with a partially filled 5s orbital cannot gain electrons from the π-bond of ethylene to form π-complexes. Compared to the impregnation method, the ion exchange method can allow fine dispersion of silver particles, which can explain the superior adsorption capacity of Ag-EX/13X to Ag-IM/13X [154,155]. For further experiments, Ag-EX/13X with the best adsorption capability was used as the adsorbent/catalyst.

3.5.3. Effluent ozone concentration in different reactor configurations

It has been proven that short-lived reactive species are available for the oxidation of hydrocarbons in the inner pore volume of porous catalysts such as γ-Al_2O_3 and silica in one-stage configuration [156]. However, the diffusion and subsequent decomposition of ozone on

the catalyst surface still play important roles and strongly affect the conversion and mineralization of VOCs to CO_2 [81,145]. In order to clarify the effect of ozone on the oxidative removal of the adsorbed ethylene, the concentration of ozone at the outlet of the reactor was measured with and without pre-adsorption of ethylene.
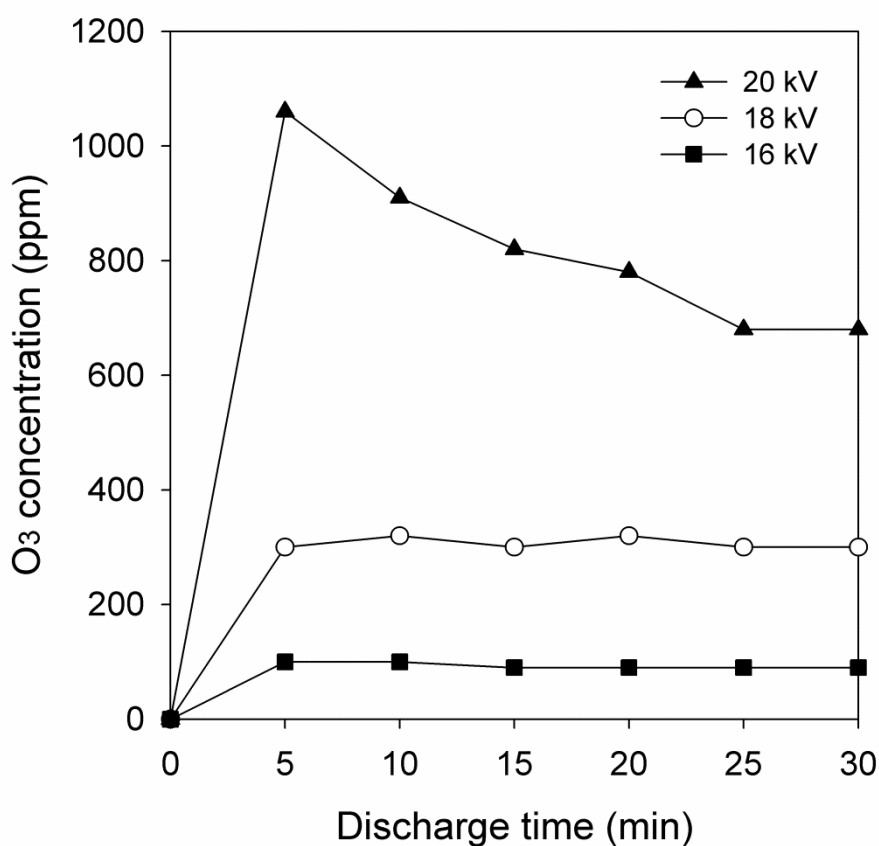
Figure 55. Outlet ozone concentration from blank DBD reactor at different applied voltages.

First, the effect of the applied voltage on the formation of ozone was examined with the blank DBD reactor (without packing) and dry synthetic air. As shown in Fig. 55, the concentration of ozone depended largely on the applied voltage which was varied from 16 to 20 kV in steps of 2 kV. At voltages of 16~18 kV, the concentration of ozone was almost stable with time around 90 ppm at 16 kV and around 300 ppm at 18 kV. As the voltage was further increased to 20 kV, the concentration of ozone increased more than threefold, compared to that

at 18 kV. However, at 20 kV, the concentration was not stable and decreased from 1000 to 700 ppm, which is attributed to the thermal decomposition arising from the increase of the reactor temperature. Considering the amount of ozone available for the oxidation of ethylene, the applied voltage was kept at 20 kV, unless stated otherwise.
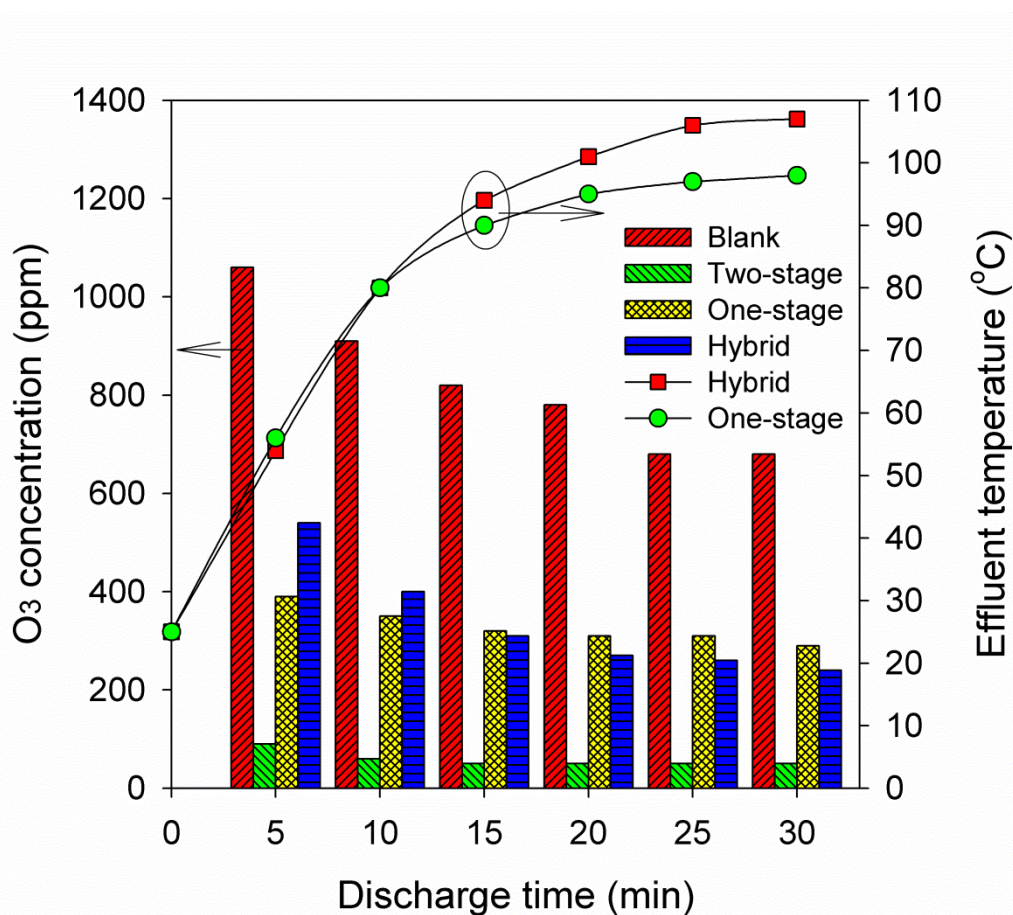
Figure 56. The outlet ozone concentration and temperature with different reactor configurations without pre-adsorbed ethylene (applied voltage 20 kV).

The dependence of ozone concentration on the reactor configuration and discharge time is shown in Fig. 56. Plasma was generated in pure synthetic air without ethylene pre-adsorption. For comparison, the ozone concentration obtained with the blank DBD reactor was also included. For all the reactor configurations, the amount of effluent ozone gradually decreased with the time-on-stream because of the thermal decomposition [157]. At the same voltage, the concentration of ozone greatly varied with the reactor configuration. Particularly, for the two-

stage configuration, more than 90 % of the ozone formed in the first stage of the reactor was catalytically decomposed as it passed through the packing region. As seen, the outlet ozone concentration of the blank reactor remained unchanged at about 700 ppm after 25 min, while that of the two-stage reactor decreased to 50 ppm after 15 min. This result clearly showed that most of the ozone generated in the gas phase migrated into the zeolite's pores to be catalytically decomposed. The high catalytic activity of the packing material for the decomposition of ozone has a beneficial effect on the oxidation of VOCs because the atomic oxygen (nascent oxygen) formed from the ozone decomposition is an effective oxidizing agent [71,156]. Meanwhile, the amounts of ozone emitted from the one-stage and hybrid reactor did not largely differ from each other, and were both higher than that of the two-stage reactor. During the first 10 min, the concentration of ozone in the hybrid reactor was slightly higher than the one-stage reactor due to the additional ozone generated in the front blank part of the hybrid reactor. However, the situation was reversed after 15 min, obviously due to the increase in the reactor temperature. As seen, the temperature of the hybrid reactor was higher than that of the one-stage reactor after 15 min due to the higher discharge power, reaching 107 ^{o}C in 30 min. The discharge powers of the two-stage, one-stage and hybrid reactors determined from the Lissajous voltage-charge figures were 8.1, 9.5 and 16.9 W, respectively. The concentration of the effluent ozone followed the order: blank > hybrid ≈ one-stage > two-stage.
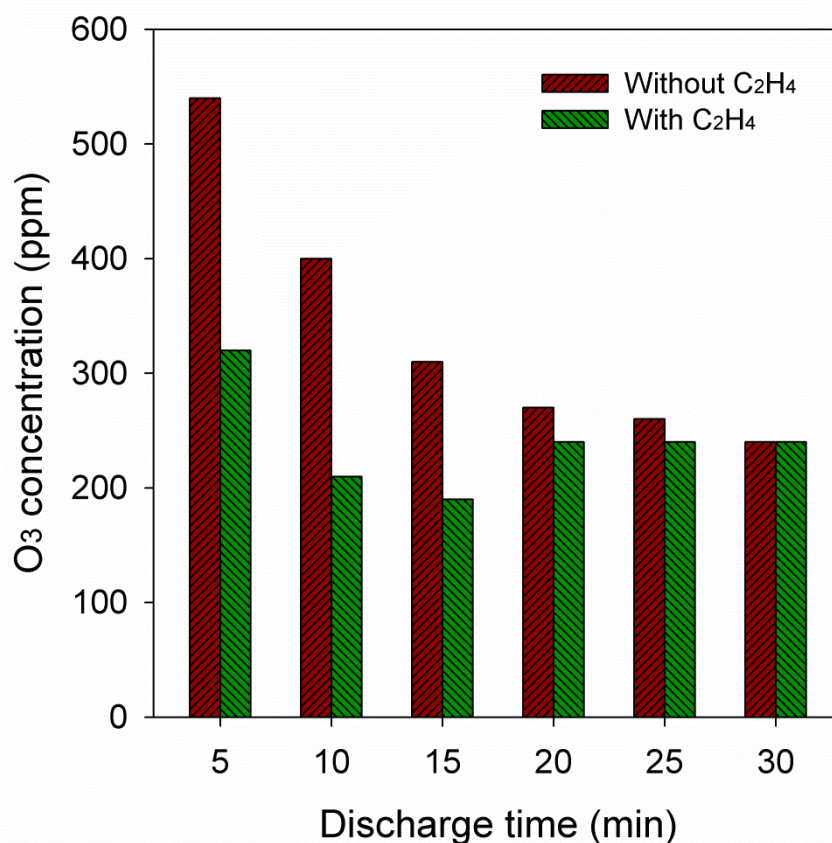
Figure 57. Outlet ozone concentration of hybrid reactor with and without pre-adsorbed ethylene (applied voltage 20 kV).

The variations of outlet ozone concentration of the hybrid reactor with and without pre-adsorbed ethylene with time are shown in Fig. 57. The concentration of ozone without pre-adsorbed ethylene decreased with time from 540 to 240 ppm after 30 min. On the other hand, the amount of ozone emitted from the reactor when ethylene was pre-adsorbed on Ag-EX/13X for 100 min displayed a different behavior. During the first 15 min, a large portion of the ozone was directly consumed by the adsorbed ethylene, lowering the outlet ozone concentration and reaching a minimum of 190 ppm. The concentration of ozone then gradually increased until it became almost the same as the case without pre-adsorbed ethylene. This result indicated that ozone was directly consumed by the adsorbed ethylene.

3.5.4. Formation of products during the oxidation of the adsorbed ethylene

The removal of ethylene from air stream was carried out sequentially, with 100-min adsorption of dilute ethylene on the Ag-EX/13X followed by plasma-catalytic oxidation of the adsorbed ethylene. The amount of ethylene adsorbed for 100 min was estimated to be 817.5 μmol on the basis of 25 ^{o}C and 1.0 atm. The FTIR spectra of the plasma-treated gases for 10 min of discharge are shown in Fig. 58. The carbon-containing products observed in the one- and two-stage reactors were only carbon oxides (CO and CO_2) and no desorbed ethylene. However, traces of formaldehyde (HCHO) and desorbed ethylene (C_2H_4) were detected in the hybrid reactor, as shown in the insets of Fig. 58.
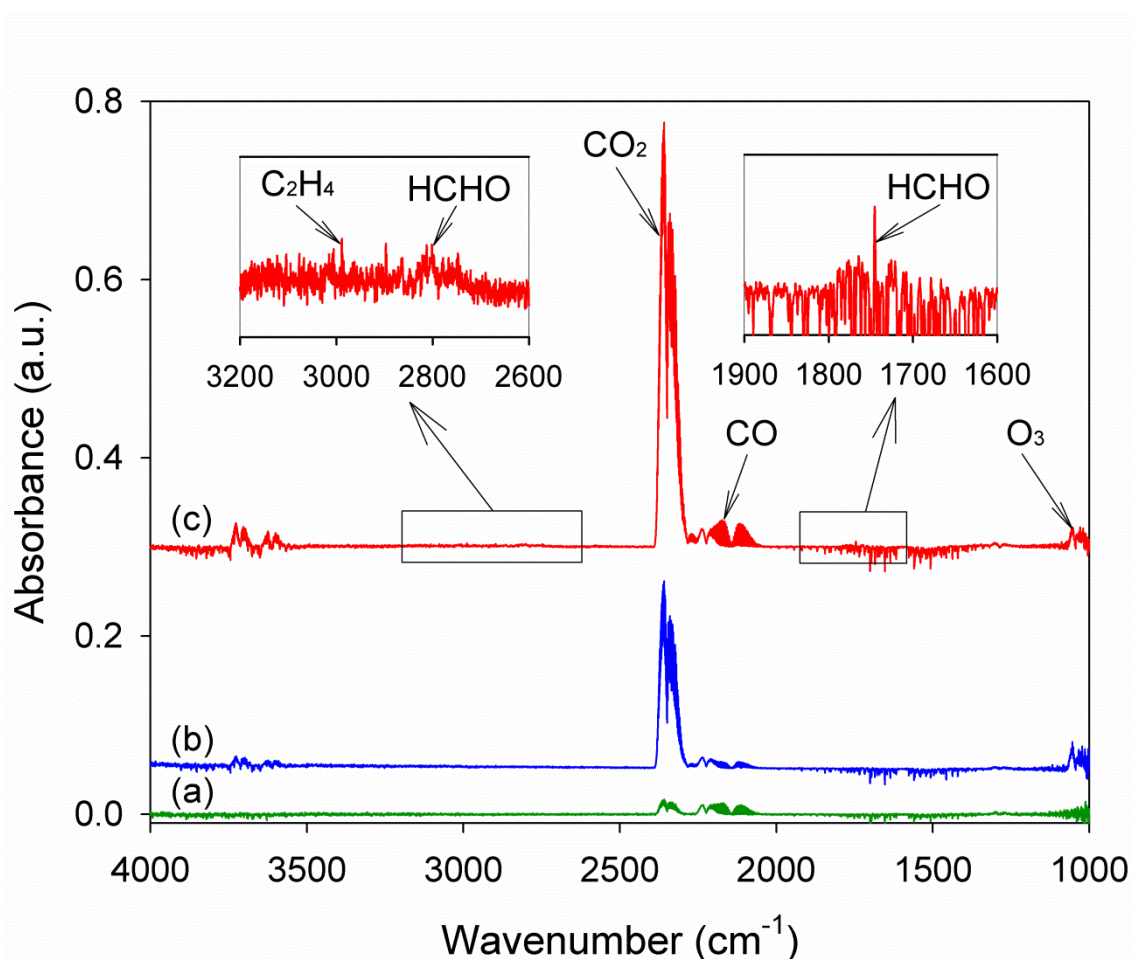
Figure 58. FTIR spectra of effluent gases at the outlet of two-stage (a), one-stage (b), and hybrid (c) reactors at 10 min of plasma oxidation.

At the same applied voltage and treatment time, the hybrid reactor exhibited the highest intensities of CO and CO_2, indicating its high performance in the oxidation of the adsorbed ethylene. The formation of HCHO along with the desorption of C_2H_4 suggests that HCHO was formed favorably in plasma gas phase mainly by radical destruction of gaseous ethylene molecules through the reaction (R 51) (section 3.4.3) and following reaction [48,142]:

$$C_2H_4 + {}^\bullet OH \rightarrow CH_2O + {}^\bullet CH_3 \qquad\qquad (R\ 54)$$

At the same reactor temperature, desorption of C_2H_4 was observed only with the hybrid reactor, which can be ascribed to the fast oxidation of the adsorbed ethylene to carbon oxides and water. The produced carbon oxides and water then compete with the ethylene for the adsorption sites. The adsorptivities of carbon oxides and water vapor on the zeolite are greater than that of ethylene, and it is natural that they should replace the adsorbed ethylene.

Figure 59 shows the concentration of CO_2 during the oxidation step with three reactor configurations. As seen, the two-stage reactor hardly emitted any CO_2 during the first 10 min. After that, the concentration of CO_2 gradually increased up to 550 ppm, and then followed a slow decreasing trend. This result indicates that in the absence of the plasma-induced short-lived species (such as $O(^1D)$, $O(^3P)$ and OH radicals), ozone was diffused from the plasma phase and subsequently decomposed on the catalyst surfaces to form atomic oxygen, which in turn oxidized the adsorbed ethylene to CO_2. Nevertheless, the CO_2 concentration at the outlet of the one-stage reactor rapidly increased and reached a maximum at about 1150 ppm within the first 10 min of oxidation. Although the generation of ozone was less effective in the one-stage reactor due to its low gas phase volume, the short-lived oxidizing species were probably available in the inner pores of the zeolite to involve in the oxidation of the adsorbed ethylene. In addition, the higher CO_2 production in the one-stage reactor than in the two-stage reactor at the same applied voltage within 50 min also suggests the participation of the short-lived species in the oxidation process. The electrical discharges might hardly occur within the zeolite micro-

110

pores that are on angstrom scale, therefore, direct formation of the short-lived species could be neglected. However, since the short-lived species could be stabilized on the catalyst surface, it is expected that they would diffuse from the gas phase deep into the micro-pores of the zeolite [156].
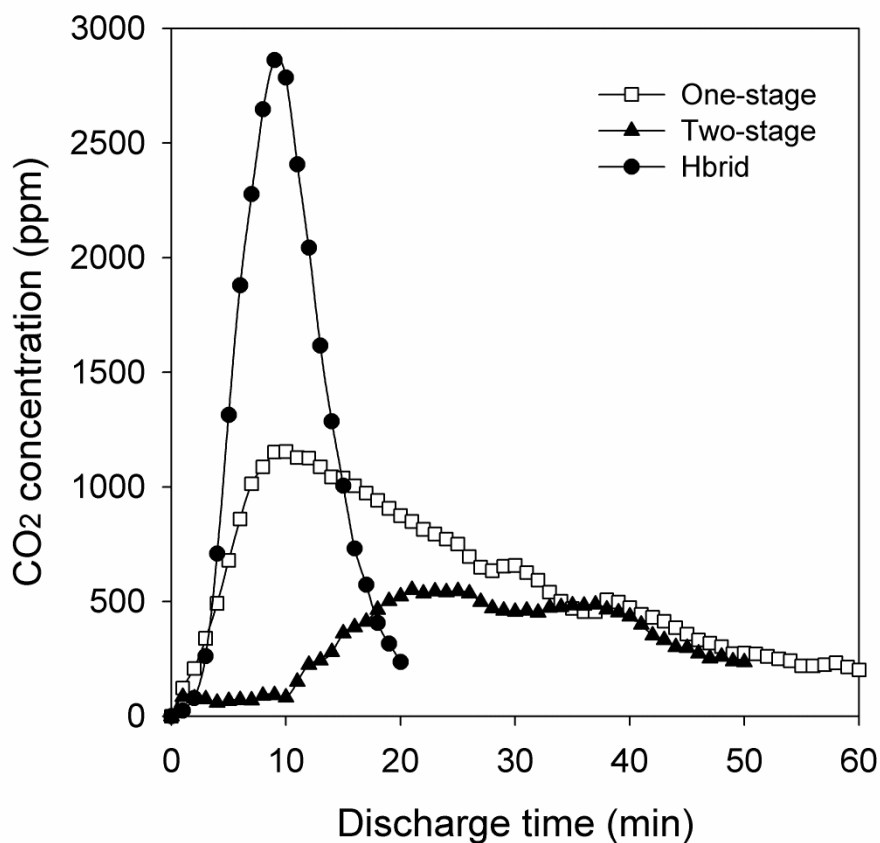
Figure 59. CO_2 concentration with different reactor configurations (adsorption time 100 min, applied voltage 20 kV).

Interestingly, the hybrid reactor exhibited a different behavior compared to the former configurations where the CO_2 concentration drastically increased up to around 2800 ppm after 10 min and then quickly decreased at the same rate. While the CO_2 concentration curves of the one- and two-stage reactors had long tails with more than 50 min, the emission of CO_2 for the hybrid reactor almost finished within 20 min. It is noteworthy that the discharge power of the

111

hybrid reactor was only about two times higher than those of the one- and two-stage reactors, resulting in lower energy consumption. Based on 20-min plasma oxidation time, the mineralization efficiencies of the two-stage, one-stage and hybrid reactors were estimated to be 10, 42, and 63 % respectively. The fast temporal evolution of CO_2 concentration for the hybrid reactor clearly showed the synergistic effects of the one- and two-stage configurations along with the effective utilization of ozone, formed in the first blank stage and the short-lived species, generated in the second packed stage for oxidation of the adsorbed ethylene.
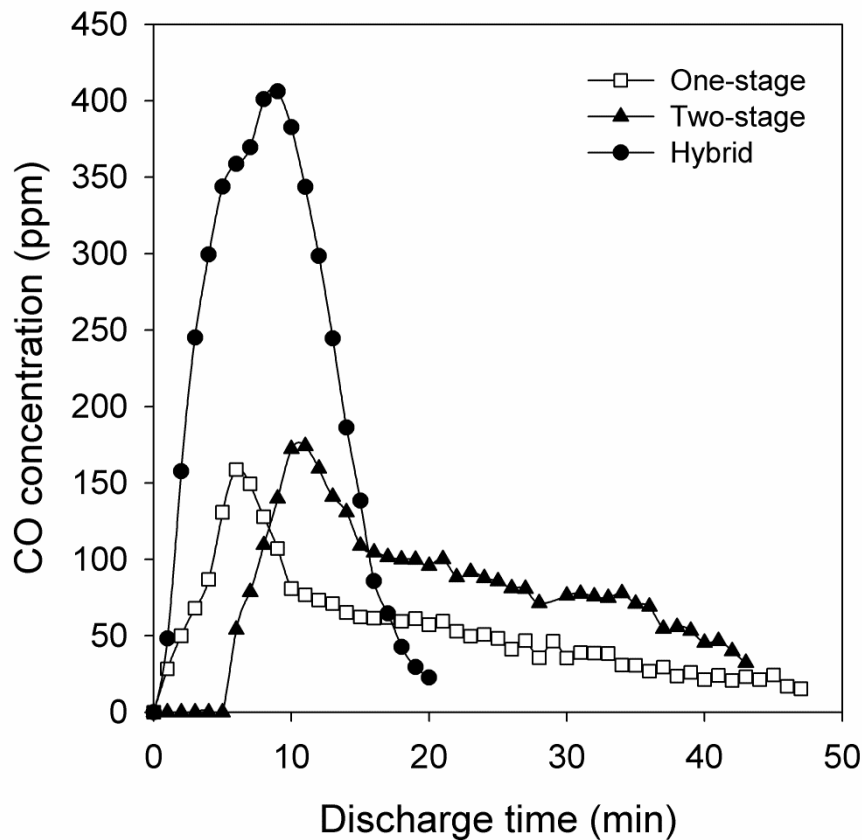
Figure 60. The CO concentration for different reactor configurations (adsorption time: 100 min, applied voltage: 20 kV).

A similarity in the evolution of CO was observed, as shown in Fig. 60. The two-stage reactor started emitting CO only after 5 min of oxidation. However, CO was detected at the

112

outlet of both the one-stage and hybrid reactors soon after plasma initiation. It was noted that during the oxidation step, the emission of CO from the one-stage reactor was less than that from the two-stage reactor. The high production of CO_2 along with low CO content of the one-stage reactor indicates that the complete oxidation of VOCs occurred when the catalysts were directly exposed to plasma discharges even with zeolite support whose micro-pores might not be sufficiently large enough for the plasma to sustain.
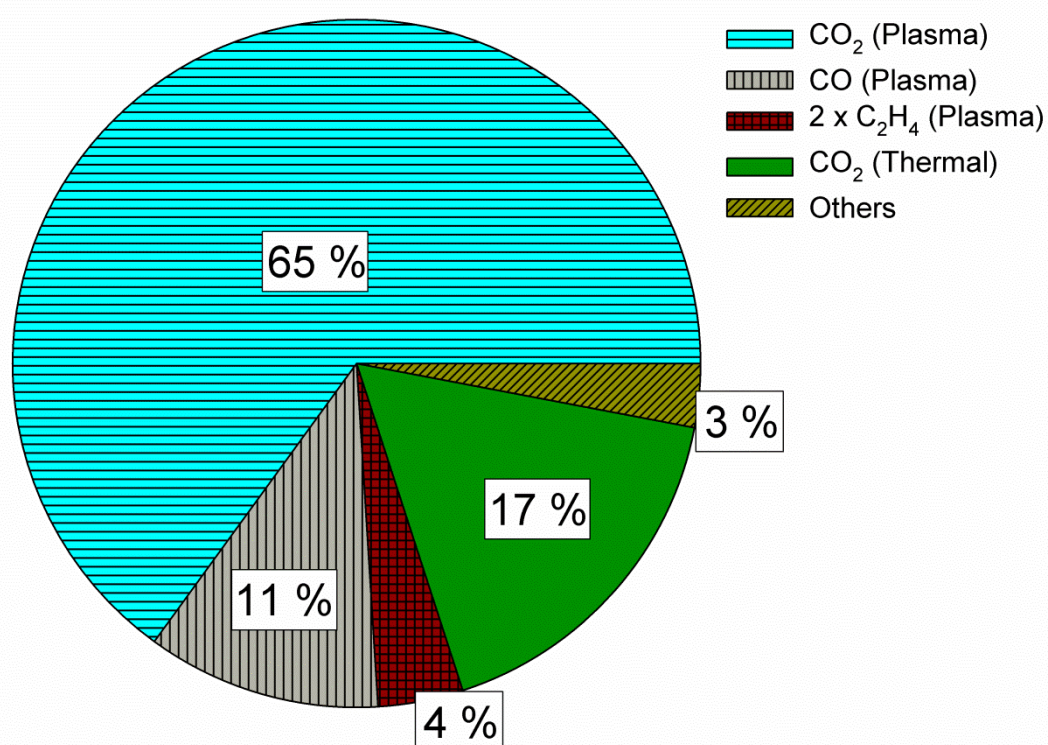
Figure 61. Contributions of C-containing products produced in hybrid reactor by plasma and thermal treatment to the carbon balance.

The contributions of C-containing products to the carbon balance for the hybrid reactor are shown in Fig. 61. The adsorbed ethylene was mainly converted into CO_x with a fraction of 76 % within ca. 30 min of plasma discharges. Meanwhile, desorbed ethylene accounted for only about 4 % of the total carbon. After the oxidation step, the reactor was thermally treated at 350

^{o}C using an electrical furnace. The C-containing species detected at the reactor outlet during post-thermal-treatment was only CO_2, which made up about 17 % in the carbon balance.

3.5.5. Multi-cycle treatment of ethylene-contaminated air using the hybrid reactor
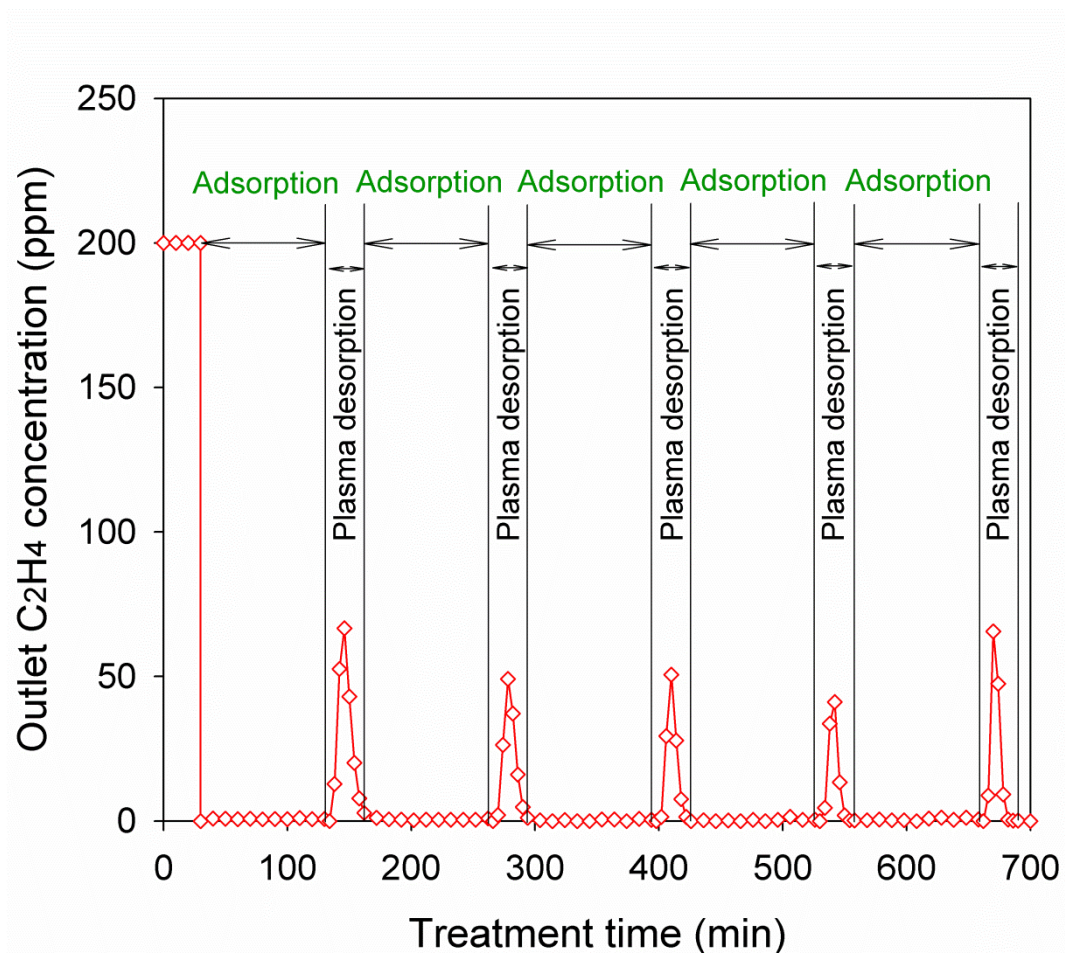
Figure 62. Outlet ethylene concentration during five cycles of treatment.

The variations in the ethylene concentration at the outlet of the hybrid reactor during five consecutive cycles of treatment are shown in Fig. 62. The experimental conditions were the same with those described in Fig. 60. Each cycle included a 100-min adsorption step followed by a 32-min plasma oxidation step. As seen, there was no significant deactivation of the adsorbent/catalyst during the five cycles corresponding to 11 h of treatment. Complete

114

adsorption of ethylene was observed for all five adsorption steps. In addition, the outlet concentration of ethylene at 10 min of the sixth adsorption step was checked and still remained smaller than 1.0 % of the initial concentration. Unexpectedly, the desorption of ethylene took place in the plasma oxidation steps. However, the amount of ethylene desorbed did not excess 4 % of total ethylene adsorbed. Based on the first cycle, the energy efficiency was estimated to be ca. 2.4 g $(kWh)^{-1}$.

In summary, 13X zeolite-supported Ag was employed as the dual-functional adsorbent/catalyst for the plasma-catalytic abatement of dilute ethylene. The adsorbent/catalyst prepared by ion exchange (Ag-EX/13X) exhibited better adsorption capability than the parent 13X and Ag-IM/13X prepared by impregnation method. The oxidative transformation of the adsorbed ethylene was then performed by using three different reactor configurations such as one-stage (i.e., adsorbent/catalyst in direct contact with plasma), two-stage (i.e., adsorbent/catalyst located downstream of the plasma region) and the combination of the two (hybrid). The oxidation of the adsorbed ethylene to CO_2 in the two-stage configuration can be explained by the diffusion of ozone into zeolite micro-pores, which was, however, much slower than in the one-stage and hybrid configurations. When compared at identical applied voltage of 20 kV (inlet ethylene: 200 ppm; adsorption time: 100 min; plasma oxidation time: 20 min), the mineralization efficiency of the hybrid reactor was greater than the sum of those of one- and two-stage reactors, i.e., 63, 42, and 10 %, respectively. Using the hybrid configuration, ozone and other reactive species were more effectively produced, thereby shortening the oxidation time of ethylene and therefore achieving a higher energy efficiency which was evaluated to be ca. 2.4 g $(kWh)^{-1}$.

CHAPTER 4: A STUDY ON SCALING UP OF PLASMA REACTOR

4.1. Introduction

In designing a robust NTP reactor to be industrially used for VOC abatement, the scaling up reactor is an important and difficult task. In which, effect of scalability on the reactor performance (e.g., energy transfer and VOC decomposition efficiencies) should be investigated.

In this chapter, a one-stage plasma-catalysis reactor similar to one described in Section 2.2.6 was used as a standard reactor. In which, the 50 mm-long plasma region was fully packed with γ-alumina. The use of γ-alumina instead of 13X zeolite aimed to reduce VOC adsorption for continuous plasma treatment test. Ethylene with a concentration 1660 ppm in dry air was used as a model VOC.
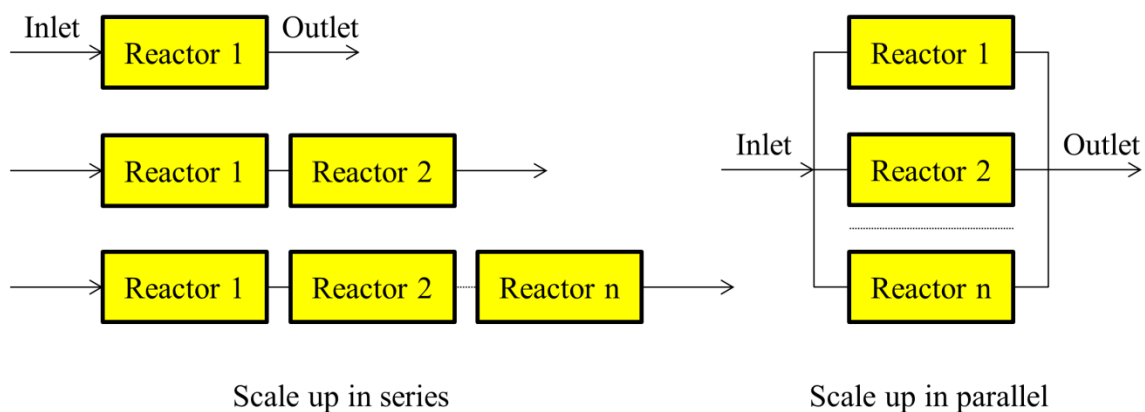
Figure 63. Scaling up of plasma reactor.

The reactor was scaled up in either series or parallel by varying the number of standard reactors, n, from 1 to 3 (see Figure 63). The scaled-up reactor was energized by one AC power supply at a frequency of 400 Hz. To investigate the scale-up effects, the inlet gas flow rate was

increased from 0.7 to 1.4 and 2.1 L min^{-1} as the number of standard reactors increased from 1 to 2 and 3, respectively. The electrical and gas concentration measurements are previously described in Chapter 3.

4.2. The behaviors of scaled-up reactor

4.2.1. Equivalent electrical circuit

For electrical analysis, each standard reactor could be simply treated as a capacitor, C_s (Fig. 64). This capacitor comprises two components connected in series, i.e., C_{gp} formed by gas-pellet layer and C_d formed by dielectric layer. In fact, when plasma proceeds, the equivalent circuit of the reactor includes not only capacitor but also resistor formed by electrical discharges [34].

$$C_s = \frac{C_{gp}C_d}{C_{gp}+C_d}$$
(E 11)

As the reactor was scaled up in series, the reactor length was directly proportional to the number of standard reactors and therefore, the capacitances of the gas-pellet and dielectric layers were nC_{gp} and nC_d, respectively. The capacitance of the scaled-up reactor (in series), C_{Series}, is calculated as follows:

$$C_{Series} = \frac{nC_{gp}\times nC_d}{nC_{gp}+nC_d} = n\frac{C_{gp}C_d}{C_{gp}+C_d}$$
(E 12)

As the reactor was scaled-up in parallel, the equivalent circuit contains n capacitors C_s connected in parallel and therefore, the equivalent capacitance $C_{Parallel}$ is calculated by following equation:

$$C_{Parallel} = n \times C_s = n \frac{C_{gp}C_d}{C_{gp} + C_d} \qquad\qquad (E\ 13)$$
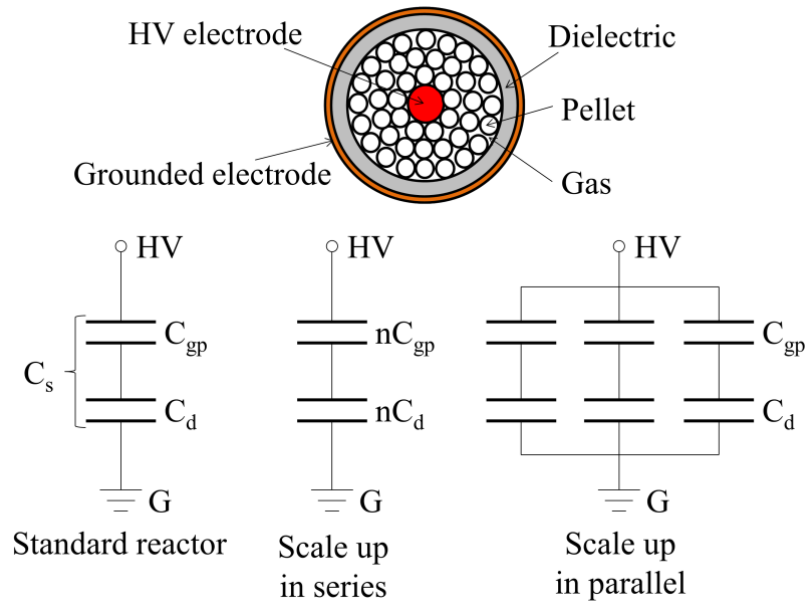
Figure 64. Equivalent circuit of NTP reactor as scaled up in series and parallel.

From equations E 12 and 13, the equivalent capacitance of the reactor does not depend on the way reactor is scaled up (i.e., in series and parallel). In fact, there were no obvious differences in the experimental results obtained for the two cases.

4.2.2. Discharge power

Figure 65 shows the discharge power as a function of the applied voltage and number of standard reactors. The discharge power increased linearly with increasing the applied voltage simply because the higher the applied voltage, the stronger the average electric field between the two electrodes. It is natural that at the same applied voltage, the multiplication of the standard

reactor led to more discharge power and therefore dissipated energy because the discharge volume of scaled-up reactor was also multiplied.
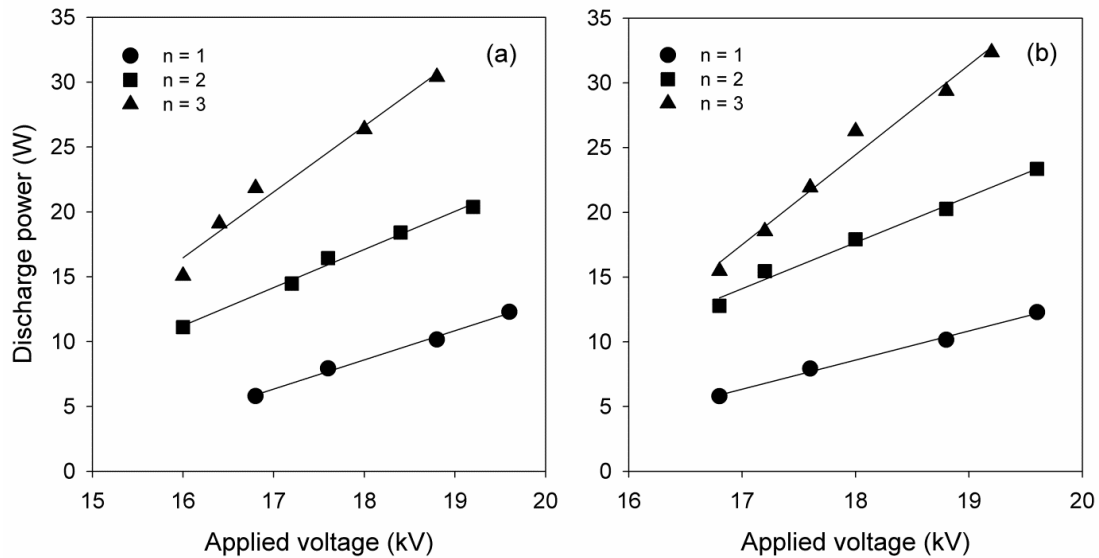
Figure 65. Discharge power of DBD packed-bed reactor scaled up in series (a) and parallel (b).

4.2.3. Energy transfer efficiency

The energy efficiency is defined as the percentage ratio of the discharge power to the input power recorded on the power source. The energy transfer efficiency of the scaled-up reactor is plotted as functions of applied voltage and number of standard reactors (Fig. 66). An increase in the applied voltage slightly increased the energy transfer efficiency. Meanwhile, scaling up the reactor is effective for getting high energy transfer efficiency. Larger-sized reactors had higher energy transfer efficiencies. For example, at an applied voltage of ca. 19 kV, the energy transfer efficiency was ca. 20, 30 and 40 % for n = 1, 2 and 3, respectively. From practical point of view, a system with high efficiency of energy transfer from power source to the reactor is desirable.
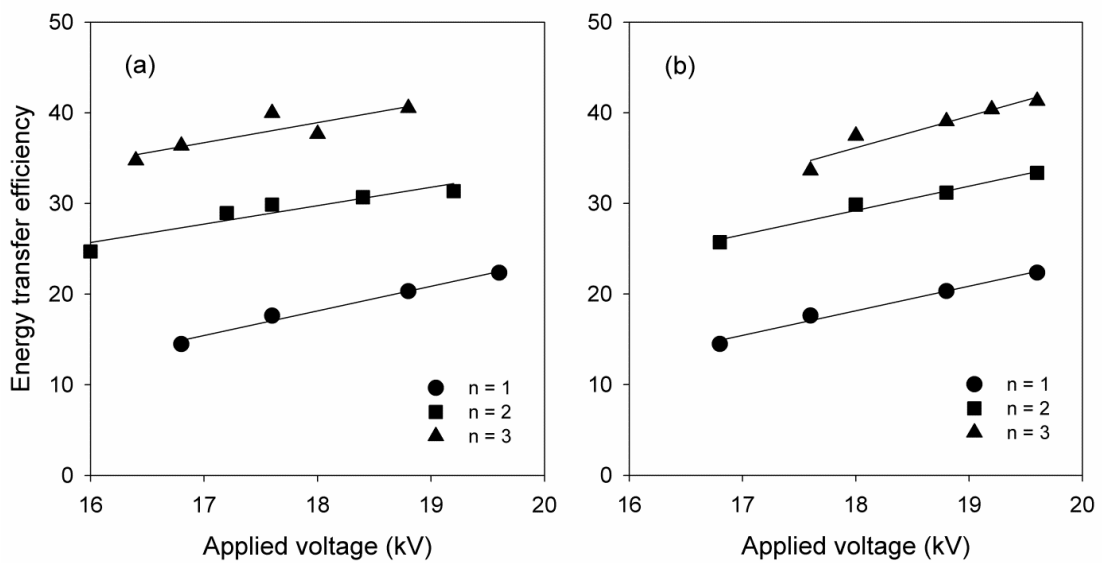
Figure 66. Energy transfer efficiency of DBD reactor as scaled up in series (a) and parallel (b).

4.2.4. Specific input energy
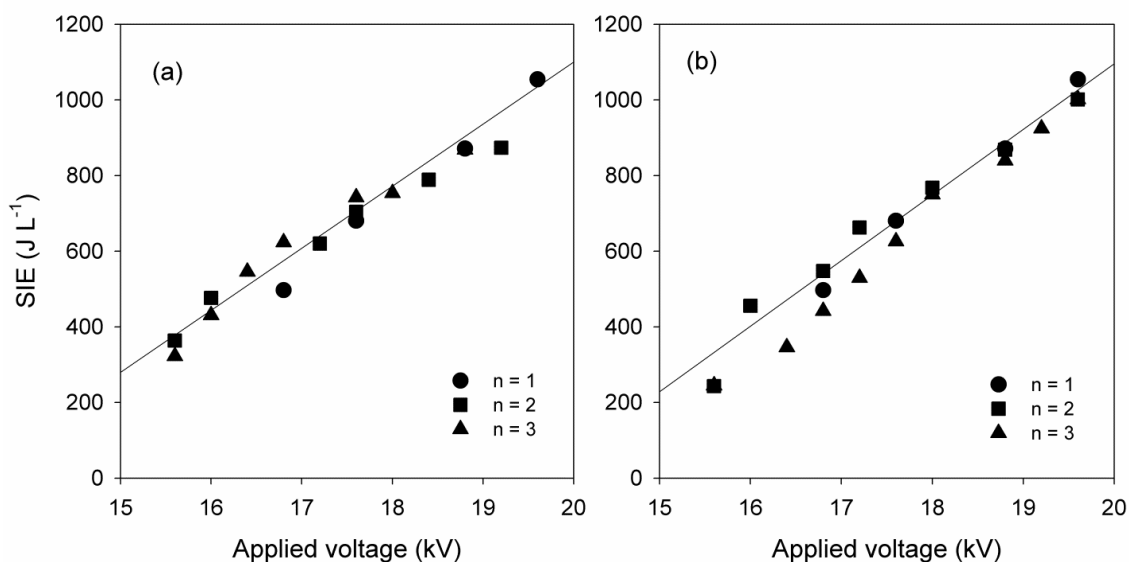
Figure 67. Applied voltage dependence of SIE of DBD packed-bed reactor scaled up in series (a) and parallel (b).

The specific input energy is an important parameter to be considered when scaling up the plasma reactor because it is related to the operating cost of the treatment process. The applied voltage dependence of SIE of the reactors is shown in Fig. 67. Although the discharge power and energy transfer efficiency increased with increasing the number of standard reactors, the SIE hardly depended on the scale of reactor and increased linearly with the applied voltage.

4.2.5. VOC decomposition efficiency
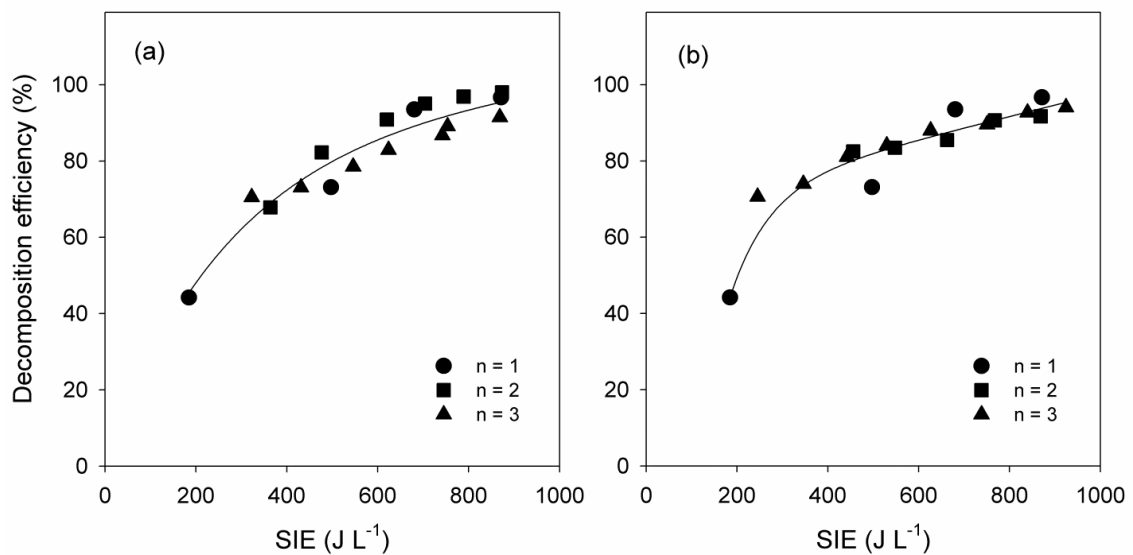
Figure 68. SIE dependence of VOC decomposition efficiency of DBD packed-bed reactor scaled up in series (a) and parallel (b).

From Fig. 67, the SIE could be considered to be independent on the scale of reactor. Thus, to investigate the scale up effect on the reactor performance in terms of VOC removal, the VOC decomposition efficiency was evaluated as a function of SIE. As seen from Fig. 68, all experimental results seem to locate on the same curve, regardless of the number of standard reactors or reactor size. In other words, the scale up of reactor did not affect the SIE and VOC decomposition efficiency. Based on the results obtained with the standard reactor, one can

predict the amount of energy needed and size of the real reactor to treat a polluted gas with known VOC concentration and flow rate.

In summary, the scale-up effects on the DBD packed-bed reactor performance were studied in this chapter. Generally, there was no obvious difference in the results as the reactor was scaled up in series and parallel. The large-sized reactor was effective for the energy transfer efficiency. However, the SIE and VOC decomposition efficiency were independent on the size of reactor. The energy required and reactor size to treat a gas with known VOC concentration and flow rate therefore could be predicted from the results obtained for the standard reactor. From the required input energy, the power source should be designed to match with the reactor, in order to gain high energy transfer efficiency.

CHAPTER 5: CONCLUSIONS

In this thesis, the combination of NTP with catalysis and catalysis/adsorption has been investigated for VOC abatement towards enhancing the VOC decomposition and energy efficiencies.

The experimental results have confirmed the great potential of NTP as an effective tool for end-of-pipe waste gas treatment. By producing various reactive species such as OH, $O(^1D)$, $O(^3D)$, O_3 and N_2^*, NTP is able to transform VOCs into simpler and less harmful compounds (e.g., HCHO, CO_x and H_2O) under mild conditions of temperature and pressure. The coupling of NTP with appropriate catalysts brings synergetic effects in terms of improving VOC decomposition efficiency and reducing formation of byproducts. Meanwhile, the combination of NTP with catalysis/adsorption in a cyclic treatment largely enhances the energy efficiency of the process.

From this thesis, it is possible to conclude that the one-stage combination of NTP with an ozone decomposing catalyst is not advantageous for treatment of ozone-reactive VOCs because a major part of plasma-induced ozone is rapidly catalytically decomposed in plasma to molecular oxygen without participation in the VOC oxidation. In such a case, the generation of ozone in plasma stage is crucial for oxidative transformation of VOCs and the use of ozone decomposing catalyst for ozone recycle is effective in the post plasma region. However, as dealing with persistent compounds (e.g., acetone), the activity for ozone decomposition of catalyst to produce more reactive species, namely atomic oxygen becomes important and positively affects the removal of VOCs.

The combination of adsorption with plasma-catalytic oxidation for VOC abatement is very efficient in the sense of energy consumption and ozone emission, especially at low VOC

concentrations. The adsorption of VOCs on zeolite strongly depends on the physicochemical natures of both VOCs and zeolite and it can be greatly enhanced by proper modification of zeolite with transition metals using impregnation or ion exchange methods. In the cyclic process, NTP is able to regenerate the adsorbent by oxidative desorption of adsorbed VOCs without external heating. Both ozone and short lived-species produced in plasma play important roles in the catalytic oxidation reactions. The short-lived species are believed to be stabilized on the catalyst surface and diffuse deep into the micro-pores of zeolite to oxidize adsorbed VOCs. Ozone also takes part in the oxidative transformation of adsorbed VOCs into CO_x and H_2O. A reactor which has a sufficient volume fraction of plasma gas phase is favorable to effectively produce ozone for catalytic oxidation of VOCs adsorbed within zeolite micropores. In comparison with a reactor operating under continuous plasma conditions, the cyclic plasma reactor working under a long-time adsorption step followed by a short-time oxidation one is beneficial for achieving the high energy efficiency.

It is drawn from the investigation of scaling up a NTP reactor that the specific input energy and VOC decomposition efficiency do not depend on the reactor size as well as the way reactor scaled up (i.e., in series or parallel). Based on these results, the input energy and reactor size can be predicted, and therefore it is possible to design a NTP reactor for treatment of a specific gas stream with known VOC concentration and gas flow rate. From the required input energy, the power source should be selected to match with the designed NTP reactor in order to gain the highest energy transfer efficiency.

REFERENCES

[1]   L. Marelli, Contribution of natural sources to air pollution levels in the EU - a technical basis for the development of guidance for the Member States, 2007.

[2]   F. Popescu, I. Ionel, Anthropogenic air pollution sources, in: A. Kumar (Ed.), Air Quaity, InTech, 2010: pp. 1–23.

[3]   R.C. Flagan, J.H. Seinfeld, Fundamentals of air pollution engineering, Prentice Hall, 1988.

[4]   M. Qiu, S. Zhan, H. Yu, D. Zhu, S. Wang, Facile preparation of ordered mesoporous MnCo2O4 for low-temperature selective catalytic reduction of NO with NH3, Nanoscale. 7 (2015) 2568–2577.

[5]   Air pollution, Eur. Environ. Agency. (n.d.). http://www.eea.europa.eu/themes/air/intro.

[6]   Air pollution fact sheet 2013, European Evironment Agency, 2013.

[7]   S. Genc, Z. Zadeoglulari, S.H. Fuss, K. Genc, The adverse effects of air pollution on the nervous system, J. Toxicol. 2012 (2012) 1–23.

[8]   A.O. Rusu, E. Dumitriu, Destruction of volatile organic compounds by catalytic oxidation, Environ. Eng. Manag. J. 2 (2003) 273–302.

[9]   Environmental statistics yearbook 2012, South Korean Ministry of Environment, 2012.

[10]   V. Rao, L. Tooly, J. Drukenbrod, 2008 national emissions inventory□: review , analysis and highlights, USA Evironmental Protection Agency, 2013.

[11]   M. Sanchez, S. Karnae, K. John, Source Characterization of Volatile Organic Compounds Affecting the Air Quality in a Coastal Urban Area of South Texas, 5 (2008) 130–138.

[12]   J.C. Jones, Atmospheric pollution, Ventus publishing ApS, 2008. doi:10.1016/0269-7491(88)90162-5.

[13]   J.W. Li, K.L. Pan, S.J. Yu, S.Y. Yan, M.B. Chang, Removal of formaldehyde over MnxCe1−xO2 catalysts: Thermal catalytic oxidation versus ozone catalytic oxidation, J. Environ. Sci. (2014).

[14]   H.H. Kim, J.H. Kim, A. Ogata, Adsorption and oxygen plasma-driven catalysis for total oxidation of VOCs, Int. J. Plasma Environ. Sci. Technol. 2 (2008) 106–112.

[15]   K. Everaert, J. Baeyens, Catalytic combustion of volatile organic compounds, J. Hazard. Mater. 109 (2004) 113–39.

[16] M. Hosseini, T. Barakat, R. Cousin, A. Aboukaïs, B.-L. Su, G. De Weireld, et al., Catalytic performance of core–shell and alloy Pd–Au nanoparticles for total oxidation of VOC: The effect of metal deposition, Appl. Catal. B Environ. 111-112 (2012) 218–224.

[17] S.C. Kim, W.G. Shim, Catalytic combustion of VOCs over a series of manganese oxide catalysts, Appl. Catal. B Environ. 98 (2010) 180–185.

[18] J. Łojewska, A. Kołodziej, J. Żak, J. Stoch, Pd/Pt promoted Co3O4 catalysts for VOCs combustion, Catal. Today. 105 (2005) 655–661.

[19] E. Rezaei, J. Soltan, Low temperature oxidation of toluene by ozone over MnOx/γ-alumina and MnOx/MCM-41 catalysts, Chem. Eng. J. 198-199 (2012) 482–490.

[20] M.H. Castaño, R. Molina, S. Moreno, Catalytic oxidation of VOCs on MnMgAlOx mixed oxides obtained by auto-combustion, J. Mol. Catal. A Chem. 398 (2015) 358–367.

[21] S. Azalim, M. Franco, R. Brahmi, J.-M. Giraudon, J.-F. Lamonier, Removal of oxygenated volatile organic compounds by catalytic oxidation over Zr-Ce-Mn catalysts., J. Hazard. Mater. 188 (2011) 422–7.

[22] S.M. Saqer, D.I. Kondarides, X.E. Verykios, Catalytic oxidation of toluene over binary mixtures of copper, manganese and cerium oxides supported on γ-Al2O3, Appl. Catal. B Environ. 103 (2011) 275–286.

[23] S. Azalim, R. Brahmi, M. Agunaou, a. Beaurain, J.-M. Giraudon, J.-F. Lamonier, Washcoating of cordierite honeycomb with Ce–Zr–Mn mixed oxides for VOC catalytic oxidation, Chem. Eng. J. 223 (2013) 536–546.

[24] B. de Rivas, C. Sampedro, M. García-Real, R. López-Fonseca, J.I. Gutiérrez-Ortiz, Promoted activity of sulphated Ce/Zr mixed oxides for chlorinated VOC oxidative abatement, Appl. Catal. B Environ. 129 (2013) 225–235.

[25] M. Konsolakis, S.A.C. Carabineiro, P.B. Tavares, J.L. Figueiredo, Redox properties and VOC oxidation activity of Cu catalysts supported on Ce₁ -xSmxOδ mixed oxides., J. Hazard. Mater. 261 (2013) 512–21.

[26] D. Delimaris, T. Ioannides, VOC oxidation over MnOx–CeO2 catalysts prepared by a combustion method, Appl. Catal. B Environ. 84 (2008) 303–312.

[27] X. Chen, S.A.C. Carabineiro, S.S.T. Bastos, P.B. Tavares, J.J.M. Órfão, M.F.R. Pereira, et al., Exotemplated copper, cobalt, iron, lanthanum and nickel oxides for catalytic oxidation of ethyl acetate, J. Environ. Chem. Eng. 1 (2013) 795–804.

[28] C. Yk, L. Chuah, N.M. Adam, B.A.A. Yousef, Prediction of catalytic converter efficiency in natural gas engine for nitrogen monoxide and carbon monoxide emission control, Adv. Mech. Eng. Its Appl. 3 (2012) 268–277.

[29] S.S. Kolekar, S.H. Gaikwad, M.A. Anuse, Selective liquid-liquid extraction of platinum (IV) from ascorbate media by n-n-octylaniline: analysis of real samples, in: Proc. Int. Symp. Solvent Extr., 2002: pp. 588–603.

[30] D. Chatterjee, O. Deutschmann, J. Warnatz, Detailed surface reaction mechanism in a three-way catalyst, R. Soc. Chem. 119 (2001) 371–384.

[31] The impact of gasoline fuel sulfur on catalytic emission control systems, Manufacturers of Emission Controls Association, 1998.

[32] V. Nehra, Atmospheric non-thermal plasma sources, Int. J. Eng. 2 (2008) 53–68.

[33] T. Kuwahara, M. Okubo, T. Kuroki, H. Kametaka, T. Yamamoto, Odor removal characteristics of a laminated film-electrode packed-bed nonthermal plasma reactor., Sensors (Basel). 11 (2011) 5529–42.

[34] K.G. Kostov, R.Y. Honda, L.M.S. Alves, M.E. Kayama, Characteristics of dielectric barrier discharge reactor for material treatment, 1 (2009) 322–325.

[35] U. Kogelschatz, Dielectric-barrier discharges □: their history, discharge physics , and industrial applications, Plasma Chem. Plasma Process. 23 (2003) 1–46.

[36] X. Xu, Dielectric barrier discharge - properties and applications, Thin Solid Films. 390 (2001) 237–242.

[37] U. Kogelschatz, Filamentary, patterned, and diffuse barrier discharges, IEEE Trans. Plasma Sci. 30 (2002) 1400–1408.

[38] V.I. Parvulescu, M. Magureanu, P. Lukes, Plasma chemistry and catalysis in gases and liquids, Wiley-VCH, Weinheim, Germany, 2012.

[39] H.-H. Kim, Nonthermal plasma processing for air-pollution control: a historical review, current issues, and future prospects, Plasma Process. Polym. 1 (2004) 91–110.

[40] H.H. Kim, G. Prieto, K. Takashima, S. Katsura, A. Mizuno, Performance evaluation of discharge plasma process for gaseous pollutant removal, J. Electrostat. 55 (2002) 25–41.

[41] T. Zhu, J. Li, Y. Jin, Y. Liang, G. Ma, Decomposition of benzene by non-thermal plasma processing: Photocatalyst and ozone effect, Int. J. Environ. Sci. Tech. 5 (2008) 375–384.

[42] J. Chae, S. Moon, H. Sun, K. Kim, V.A. Vassiliev, E.M. Mikholap, A study of volatile organic compounds decomposition with the use of non-thermal plasma, KSME Int. J. 13 (1999) 647–655.

[43] M.S. Gandhi, A. Ananth, Y.S. Mok, J.-I. Song, K.-H. Park, Time dependence of ethylene decomposition and byproducts formation in a continuous flow dielectric-packed plasma reactor, Chemosphere. 91 (2013) 685–91.

[44] F. Holzer, F.D. Kopinke, U. Roland, Influence of ferroelectric materials and catalysts on the performance of non-thermal plasma (NTP) for the removal of air pollutants, Plasma Chem. Plasma Process. 25 (2005) 595–611.

[45] Y.-F. Guo, D.-Q. Ye, K.-F. Chen, J.-C. He, W.-L. Chen, Toluene decomposition using a wire-plate dielectric barrier discharge reactor with manganese oxide catalyst in situ, J. Mol. Catal. A Chem. 245 (2006) 93–100.

[46] C.-L. Chang, T.-S. Lin, Decomposition of toluene and acetone in packed dielectric barrier discharge reactors, Plasma Chem. Plasma Process. 25 (2005) 227–243.

[47] C. Zheng, X. Zhu, X. Gao, L. Liu, Q. Chang, Z. Luo, et al., Experimental study of acetone removal by packed-bed dielectric barrier discharge reactor, J. Ind. Eng. Chem. (2013) 1–8.

[48] R. Aerts, X. Tu, C. De Bie, J.C. Whitehead, A. Bogaerts, An investigation into the dominant reactions for ethylene destruction in non-thermal atmospheric plasmas, Plasma Process. Polym. 9 (2012) 994–1000.

[49] H.H. Kim, A. Ogata, Nonthermal plasma activates catalyst: from current understanding and future prospects, Eur. Phys. J. Appl. Phys. 55 (2011) 13806.

[50] H.H. Kim, A. Ogata, Interaction of nonthermal plasma with catalyst for the air pollution control, Int. J. Plasma Environ. Sci. Technol. 6 (2012) 43–48.

[51] Z. Jia, A. Vega-Gonzalez, M. Ben Amar, K. Hassouni, S. Tieng, S. Touchard, et al., Acetaldehyde removal using a diphasic process coupling a silver-based nano-structured catalyst and a plasma at atmospheric pressure, Catal. Today. 208 (2013) 82–89.

[52] J.C. Whitehead, Plasma catalysis: A solution for environmental problems, Pure Appl. Chem. 82 (2010) 1329–1336.

[53] F. Thevenet, L. Sivachandiran, O. Guaitella, C. Barakat, a Rousseau, Plasma–catalyst coupling for volatile organic compound removal and indoor air treatment: a review, J. Phys. D. Appl. Phys. 47 (2014) 224011.

[54] M. Lu, R. Huang, J. Wu, M. Fu, L. Chen, D. Ye, On the performance and mechanisms of toluene removal by FeOx/SBA-15-assisted non-thermal plasma at atmospheric pressure and room temperature, Catal. Today. 242 (2015) 274–286.

[55] H.-H. Kim, A. Ogata, M. Schiorlin, E. Marotta, C. Paradisi, Oxygen Isotope (18O2) Evidence on the Role of Oxygen in the Plasma-Driven Catalysis of VOC Oxidation, Catal. Letters. 141 (2011) 277–282.

[56] H.L. Chen, H.M. Lee, S.H. Chen, M.B. Chang, S.J. Yu, S.N. Li, Removal of volatile organic compounds by single-stage and two-stage plasma catalysis systems: A review of the performance enhancement mechanisms, current status, and suitable applications, Environ. Sci. Technol. 43 (2009) 2216–2227.

[57] S. Chavadej, K. Saktrakool, P. Rangsunvigit, L.L. Lobban, T. Sreethawong, Oxidation of ethylene by a multistage corona discharge system in the absence and presence of Pt/TiO2, Chem. Eng. J. 132 (2007) 345–353.

[58] H. Kim, S. Oh, A. Ogata, S. Futamura, Decomposition of benzene using Ag/TiO2 packed plasma-driven catalyst reactor□: influence of electrode configuration and Ag-loading amount, 96 (2004) 189–194.

[59] D.-Z. Zhao, X.-S. Li, C. Shi, H.-Y. Fan, A.-M. Zhu, Low-concentration formaldehyde removal from air using a cycled storage–discharge (CSD) plasma catalytic process, Chem. Eng. Sci. 66 (2011) 3922–3929.

[60] M. Magureanu, D. Dobrin, N.B. Mandache, B. Cojocaru, V.I. Parvulescu, Toluene oxidation by non-thermal plasma combined with palladium catalysts., Front. Chem. 1 (2013) 7.

[61] M. Lu, R. Huang, J. Wu, M. Fu, L. Chen, D. Ye, On the performance and mechanisms of toluene removal by FeOx/SBA-15-assisted non-thermal plasma at atmospheric pressure and room temperature, Catal. Today. 242 (2015) 274–286.

[62] M. Magureanu, N.B. Mandache, V.I. Parvulescu, C. Subrahmanyam, a. Renken, L. Kiwi-Minsker, Improved performance of non-thermal plasma reactor during decomposition of trichloroethylene: Optimization of the reactor geometry and introduction of catalytic electrode, Appl. Catal. B Environ. 74 (2007) 270–277.

[63] L. Ye, F. Feng, J. Liu, Z. Liu, K. Yan, Plasma induced toluene decomposition on alumina-supported Mn-based composite oxides catalysts, J. Phys. Conf. Ser. 418 (2013) 012116.

[64] A. Maciuca, C. Batiot-Dupeyrat, J.-M. Tatibouët, Synergetic effect by coupling photocatalysis with plasma for low VOCs concentration removal from air, Appl. Catal. B Environ. 125 (2012) 432–438.

[65] U. Roland, F. Holzer, F.-D. Kopinke, Improved oxidation of air pollutants in a non-thermal plasma, Catal. Today. 73 (2002) 315–323.

[66] S. Futamura, H. Einaga, H. Kabashima, L.Y. Hwan, Synergistic effect of silent discharge plasma and catalysts on benzene decomposition, Catal. Today. 89 (2004) 89–95.

[67] C. Ayrault, J. Barrault, N. Blin-Simiand, F. Jorand, S. Pasquiers, A. Rousseau, et al., Oxidation of 2-heptanone in air by a DBD-type plasma generated within a honeycomb monolith supported Pt-based catalyst, Catal. Today. 89 (2004) 75–81.

[68] C. Subrahmanyam, A. Renken, L. Kiwi-Minsker, Novel catalytic dielectric barrier discharge reactor for gas-phase abatement of isopropanol, Plasma Chem. Plasma Process. 27 (2006) 13–22.

[69] P. Yinsheng, Z. Shi, T. Liang, D. Jingfa, Study of the promoting effects in ethylene epoxidation, Catal. Letters. 12 (1992) 307–318.

[70] S. Imamura, M. Ikebata, T. Ito, T. Ogita, Decomposition of ozone on a silver catalyst, Ind. Eng. Chem. Res. 30 (1991) 217–221.

[71] P. Nikolov, K. Genov, P. Konova, K. Milenova, T. Batakliev, V. Georgiev, et al., Ozone decomposition on Ag/SiO2 and Ag/clinoptilolite catalysts at ambient temperature., J. Hazard. Mater. 184 (2010) 16–19.

[72] X. Tang, J. Chen, Y. Li, Y. Li, Y. Xu, W. Shen, Complete oxidation of formaldehyde over Ag/MnOx–CeO2 catalysts, Chem. Eng. J. 118 (2006) 119–125.

[73] V. Vamathevan, R. Amal, D. Beydoun, G. Low, S. McEvoy, Silver metallisation of titania particles: effects on photoactivity for the oxidation of organics, Chem. Eng. J. 98 (2004) 127–139.

[74] J. Karuppiah, E.L. Reddy, P.M.K. Reddy, B. Ramaraju, R. Karvembu, C. Subrahmanyam, Abatement of mixture of volatile organic compounds (VOCs) in a catalytic non-thermal plasma reactor., J. Hazard. Mater. 237-238 (2012) 283–9.

[75] V. Demidyuk, J.C. Whitehead, Influence of Temperature on Gas-Phase Toluene Decomposition in Plasma-Catalytic System, Plasma Chem. Plasma Process. 27 (2006) 85–94.

[76] S. Bhatia, A.Z. Abdullah, C.T. Wong, Adsorption of butyl acetate in air over silver-loaded Y and ZSM-5 zeolites: experimental and modelling studies., J. Hazard. Mater. 163 (2009) 73–81.

[77] H.H. Kim, A. Ogata, S. Futamura, Complete oxidation of volatile organic compounds (VOCs) using plasma-driven catalysis and oxygen plasma, Int. J. Plasma Environ. Sci. Technol. 1 (2007) 46–51.

[78] S. Yamamoto, S. Yao, S. Kodama, C. Mine, Y. Fujioka, Investigation of transition metal oxide catalysts for diesel PM removal under plasma discharge conditions, Open Catal. J. 1 (2008) 11–16.

[79] S. Yao, S. Yamamoto, S. Kodama, C. Mine, Y. Fujioka, Characterization of catalyst-supported dielectric barrier discharge reactor, Open Catal. J. 2 (2009) 79–85.

[80] T. Zhu, Y.D. Wan, J. Li, X.W. He, D.Y. Xu, X.Q. Shu, et al., Volatile organic compounds decomposition using nonthermal plasma coupled with a combination of catalysts, Int. J. Environ. Sci. Technol. 8 (2011) 621–630.

[81] H.Q. Trinh, Y.S. Mok, Plasma-catalytic oxidation of acetone in annular porous monolithic ceramic-supported catalysts, Chem. Eng. J. 251 (2014) 199–206.

[82] H. Einaga, A. Ogata, Benzene oxidation with ozone over supported manganese oxide catalysts: effect of catalyst support and reaction conditions., J. Hazard. Mater. 164 (2009) 1236–41.

[83] L. Ye, F. Feng, J. Liu, X. Tang, X. Zhang, Y. Huang, et al., Toluene decomposition by a two-stage hybrid plasma catalyst system in dry air, IEEE Trans. Plasma Sci. 42 (2014) 3529–3538.

[84] M. Jin, J.H. Kim, J.M. Kim, J.-K. Jeon, J. Jurng, G.-N. Bae, et al., Benzene oxidation with ozone over MnOx/SBA-15 catalysts, Catal. Today. 204 (2013) 108–113.

[85] T. Oda, H. Kuramochi, R. Ono, Trichloroethylene decomposition by the nonthermal plasma Combined with manganese-dioxide supported alumina, Int. J. Plasma Environ. Sci. Technol. 2 (2008) 50–55.

[86] S. Delagrange, L. Pinard, J. Tatibouet, Combination of a non-thermal plasma and a catalyst for toluene removal from air: Manganese based oxide catalysts, Appl. Catal. B Environ. 68 (2006) 92–98.

[87] Z. Lian, J. Ma, H. He, Decomposition of high-level ozone under high humidity over Mn–Fe catalyst: The influence of iron precursors, Catal. Commun. 59 (2015) 156–160.

[88] L.A. Zaloznaya, S.N. Tkachenko, G. V. Egorova, I.S. Tkachenko, a. V. Sobolev, E.Z. Golosman, et al., Ozone decomposition and benzene oxidation catalysts based on iron and manganese oxides as industrial wastes from water decontamination by ozone treatment, Catal. Ind. 1 (2009) 224–228.

[89] Q. Ye, T. Zhang, F. Lu, J. Li, Z. He, F. Lin, Dielectric barrier discharge in a two-phase mixture, J. Phys. D. Appl. Phys. 41 (2008) 025207.

[90] J.-O. Jo, S.B. Lee, D.L. Jang, Y.S. Mok, Plasma–catalytic ceramic membrane reactor for volatile organic compound control, IEEE Trans. Plasma Sci. 41 (2013) 3021–3029.

[91] N. Blin-Simiand, P. Tardiveau, A. Risacher, F. Jorand, S. Pasquiers, Removal of 2-heptanone by dielectric barrier discharges − The eeffect of a catalyst support, Plasma Process. Polym. 2 (2005) 256–262.

[92] V. Demidiouk, J.O. Chae, Decomposition of volatile organic compounds in plasma-catalytic system, IEEE Trans. Plasma Sci. 33 (2005) 157–161.

[93] W.S. Kang, D.H. Lee, J.-O. Lee, M. Hur, Y.-H. Song, Combination of plasma with a honeycomb-structured catalyst for automobile exhaust treatment, Environ. Sci. Technol. 47 (2013) 11358–11362.

[94] C. Barakat, P. Gravejat, O. Guaitella, F. Thevenet, A. Rousseau, Oxidation of isopropanol and acetone adsorbed on TiO2 under plasma generated ozone flow: Gas phase and adsorbed species monitoring, Appl. Catal. B Environ. 147 (2014) 302–313.

[95] T. Ohshima, T. Kondo, N. Kitajima, M. Sato, S. Member, Adsorption and Plasma Decomposition of Gaseous Acetaldehyde on Fibrous Activated Carbon, IEEE Trans. Ind. Appl. 46 (2010) 23–28.

[96] H.-H. Kim, A. Ogata, S. Futamura, Oxygen partial pressure-dependent behavior of various catalysts for the total oxidation of VOCs using cycled system of adsorption and oxygen plasma, Appl. Catal. B Environ. 79 (2008) 356–367.

[97] C. Klett, X. Duten, S. Tieng, S. Touchard, P. Jestin, K. Hassouni, et al., Acetaldehyde removal using an atmospheric non-thermal plasma combined with a packed bed: role of the adsorption process., J. Hazard. Mater. 279 (2014) 356–64.

[98] Y.S. Mok, D.H. Kim, Treatment of toluene by using adsorption and nonthermal plasma oxidation process, Curr. Appl. Phys. 11 (2011) S58–S62.

[99] K.-J. Kim, H.-G. Ahn, The effect of pore structure of zeolite on the adsorption of VOCs and their desorption properties by microwave heating, Microporous Mesoporous Mater. 152 (2012) 78–83.

[100] E. Díaz, S. Ordóñez, A. Vega, J. Coca, Adsorption characterisation of different volatile organic compounds over alumina, zeolites and activated carbon using inverse gas chromatography, J. Chromatogr. A. 1049 (2004) 139–146.

[101] Y. Yu, L. Zheng, J. Wang, Adsorption behavior of toluene on modified 13X molecular sieves, J. Air Waste Manag. Assoc. 62 (2012) 1227–32.

[102] K.-J. Kim, H.-G. Ahn, The effect of pore structure of zeolite on the adsorption of VOCs and their desorption properties by microwave heating, Microporous Mesoporous Mater. 152 (2012) 78–83.

[103] N. Patdhanagul, T. Srithanratana, K. Rangsriwatananon, S. Hengrasmee, Ethylene adsorption on cationic surfactant modified zeolite NaY, Microporous Mesoporous Mater. 131 (2010) 97–102.

[104] N. Sue-aok, T. Srithanratana, K. Rangsriwatananon, S. Hengrasmee, Study of ethylene adsorption on zeolite NaY modified with group I metal ions, Appl. Surf. Sci. 256 (2010) 3997–4002.

[105] R.L. Van Mao, G.P. Mclaughlin, Ethylene recovery from low grade gas stream by adsorption on zeolites and controlled desorption, Can. J. Chem. Eng. 66 (1988) 686–690.

[106] R.W. Triebe, F.H. Tezel, K.C. Khulbe, Adsorption of methane, ethane and ethylene on molecular sieve zeolites, Gas Sep. Purif. 10 (1996) 81–84.

[107] T. Watanabe, Acetone decomposition by water plasmas at atmospheric pressure, Chem. Eng. Sci. 69 (2012) 296–303.

[108] G.-F. Xu, Y. Gao, A. Shiue, C.-M. Ma, C.-T. Chang, Vapor photocatalytic degradation characteristics of acetone and dichloromethane using TiO2 nanotube in indoor environment, Nanosci. Nanotechnol. Lett. 3 (2011) 778–783.

[109] J.J. Orlando, The atmospheric oxidation of diethyl ether: chemistry of the C2H5–O–CH(O.)CH3 radical between 218 and 335 K, Phys. Chem. Chem. Phys. 9 (2007) 4189–4199.

[110] N. Patdhanagul, K. Rangsriwatananon, K. Siriwong, S. Hengrasmee, Combined modification of zeolite NaY by phenyl trimethyl ammonium bromide and potassium for ethylene gas adsorption, Microporous Mesoporous Mater. 153 (2012) 30–34.

[111] P.L. Hanst, S.T. Hanst, Infrared spectra for quantitative analysis of gases, Infrared Anal. Inc., Anaheim, CA. (1993).

[112] S.L. Hsu, R. Wu, A. Materials, Preparation of silver nanoparticle with different particle sizes for low- temperature sintering, Int. Conf. Nanotechnol. Biosens. 2 (2011) 55–58.

[113] A.M. Harling, D.J. Glover, J.C. Whitehead, K. Zhang, The role of ozone in the plasma-catalytic destruction of environmental pollutants, Appl. Catal. B Environ. 90 (2009) 157–161.

[114] M.S. Gandhi, A. Ananth, Y.S. Mok, J.-I. Song, K.-H. Park, Effect of porosity of α-alumina on non-thermal plasma decomposition of ethylene in a dielectric-packed bed reactor, Res. Chem. Intermed. 40 (2013) 1483–1493.

[115] W. Li, G. V Gibbs, S.T. Oyama, R. V April, Mechanism of ozone decomposition on a manganese oxide catalyst. 1. In situ Raman spectroscopy and ab initio molecular orbital calculations, 7863 (1998) 9041–9046.

[116] W.G. Mallard, F. Westley, J.T. Herron, R. Hampso, NIST chemical kinetics database: Version 2Q98. Gaithersburg, MD, USA: NIST, (1998).

[117] T. Yamamoto, VOC decomposition by nonthermal plasma processing-a new approach, J. Electrostat. 42 (1997) 227–238.

[118] M.T. Islam, N. Rodríguez-Hornedo, S. Ciotti, C. Ackermann, Fourier transform infrared spectroscopy for the analysis of neutralizer carbomer and surfactant-carbomer interactions in aqueous, hydroalcoholic, and anhydrous gel formulations, AAPS J. 6 (2004) 1–7.

[119] M.R.H.M. Haris, S. Kathiresan, S. Mohan, FT-IR and FT-Raman spectra and normal coordinate analysis of poly methyl methacrylate, Der. Pharma. Chem. 2 (2010) 316–323.

[120] S.D. Walsangikar, N.M. Bhatia, M.S. Bhatia, Structural modification and evaluation of ibuprofen to overcome gi side effects, Int. J. A. PS. BMS. 2 (2013) 138–148.

[121] J.B. Dholakiya, H.J. Patel, K.H. Patel, R.M. Patel, Novel acrylic copolymers derived from Paracetamol: determination of reactivity ratio, microbial screening and thermal properties, Der Chem. Sin. 2 (2011) 112–128.

[122] J. Cao, Biotemplating of highly porous oxide ceramics, Cuvillier Verlag, Göttingen, 2005.

[123] N.F. Jaafar, A. Abdul Jalil, S. Triwahyono, M.N. Muhd Muhid, N. Sapawe, M.A.H. Satar, et al., Photodecolorization of methyl orange over α-Fe2O3-supported HY catalysts: The effects of catalyst preparation and dealumination, Chem. Eng. J. 191 (2012) 112–122.

[124] S. Boxiong, Y.A.O. Yan, M.A. Hongqing, L.I.U. Ting, Ceria modified MnOx/TiO2-pillared clays catalysts for selective catalytic reduction of NO with NH3 at low temperature, Chinese J. Catal. 32 (2011) 1803–1811.

[125] Q.H. Trinh, M.S. Gandhi, Y.S. Mok, Adsorption and plasma-catalytic oxidation of acetone over zeolite-supported silver catalyst, Jpn. J. Appl. Phys. 04 (2015) 01AG04. http://stacks.iop.org/1347-4065/54/i=1S/a=01AG04.

[126] X. Zhu, X. Gao, C. Zheng, Z. Wang, M. Ni, X. Tu, Plasma-catalytic removal of a low concentration of acetone in humid conditions, RSC Adv. 4 (2014) 37796.

[127] W. Li, S.T. Oyama, Mechanism of ozone decomposition on a manganese oxide catalyst. 2. Steady-state and transient kinetic studies, J. Am. Chem. Soc. 120 (1998) 9047–9052.

[128] A. Ogata, K. Saito, H.-H. Kim, M. Sugasawa, H. Aritani, H. Einaga, Performance of an ozone decomposition catalyst in hybrid plasma reactors for volatile organic compound removal, Plasma Chem. Plasma Process. 30 (2009) 33–42.

[129] J. Van Durme, J. Dewulf, W. Sysmans, C. Leys, H. Van Langenhove, Efficient toluene abatement in indoor air by a plasma catalytic hybrid system, Appl. Catal. B Environ. 74 (2007) 161–169.

[130] A.M. Vandenbroucke, R. Morent, N. De Geyter, C. Leys, Non-thermal plasmas for non-catalytic and catalytic VOC abatement, J. Hazard. Mater. 195 (2011) 30–54.

[131] D. V Lopaev, E.M. Malykhin, V. a Namiot, UV absorption of vibrationally excited ozone, J. Phys. B At. Mol. Opt. Phys. 41 (2008) 085104.

[132] D. Marinov, V. Guerra, O. Guaitella, J.-P. Booth, A. Rousseau, Ozone kinetics in low-pressure discharges: vibrationally excited ozone and molecule formation on surfaces, Plasma Sources Sci. Technol. 22 (2013) 055018.

[133] B. Eliasson, M. Hirth, U. Kogelschatz, Ozone synthesis from oxygen in dielectric barrier discharges, J. Phys. D. Appl. Phys. 20 (1987) 1421.

[134] T. Yamamoto, K. Ramanathan, P.A. Lawless, D.S. Ensor, J.R. Newsome, N. Plaks, et al., Control of volatile organic compounds by an AC energized ferroelectric pellet reactor and a pulsed corona reactor, IEEE Trans. Ind. Appl. 28 (1992) 528–534.

[135] S. Yagi, M. Tanaka, Mechanism of ozone generation in air-fed ozonisers, J. Phys. D Appl. Phys. 12 (1979) 1509–1520.

[136] L. Sivachandiran, F. Thevenet, A. Rousseau, Non-thermal plasma assisted regeneration of acetone adsorbed TiO2 surface, Plasma Chem. Plasma Process. 33 (2013) 855–871.

[137] S. Dzwigaj, Y. Millot, J.-M. Krafft, N. Popovych, P. Kyriienko, Incorporation of silver atoms into the vacant T-atom sites of the framework of SiBEA zeolite as mononuclear Ag(I) evidenced by XRD, FTIR, NMR, DR UV−vis, XPS, and TPR, J. Phys. Chem. C. 117 (2013) 12552–12559.

[138] A. Jodaei, D. Salari, A. Niaei, M. Khatamian, N. Caylak, Preparation of Ag-M (M: Fe, Co and Mn)-ZSM-5 bimetal catalysts with high performance for catalytic oxidation of ethyl acetate, Environ. Technol. 32 (2011) 395—406.

[139] C.D. Wagner, W.M. Riggs, L.E. Davis, J.F. Moulder, Handbook of X-ray photoelectron spectroscopy, (1979).

[140] P. Baeza, G. Aguila, F. Gracia, P. Araya, Desulfurization by adsorption with copper supported on zirconia, Catal. Commun. 9 (2008) 751–755.

[141] H. Kim, J. Park, Y. Jung, The binding nature of light hydrocarbons on Fe/MOF-74 for gas separation., Phys. Chem. Chem. Phys. 15 (2013) 19644–50.

[142] R. Aerts, X. Tu, W. Van Gaens, J.C. Whitehead, A. Bogaerts, Gas purification by nonthermal plasma: A case study of ethylene, Environ. Sci. Technol. 47 (2013) 6478–6485.

[143] M.C. Petty, Molecular Electronics: From Principles to Practice, West Sussex PO19 8SQ, England, 2007.

[144] S. Mentus, Z. Mojovic, V. Radmilovic, The use of NaX zeolite as a template to obtain a mono-atomic pt dispersion by impregnation with Pt(II) acetylacetonate/acetone solution, J. Serbian Chem. Soc. 74 (2009) 1113–1123.

[145] P. Konova, M. Stoyanova, a Naydenov, S. Christoskova, D. Mehandjiev, Catalytic oxidation of VOCs and CO by ozone over alumina supported cobalt oxide, Appl. Catal. A Gen. 298 (2006) 109–114.

[146] G. V. Mamontov, V. V. Dutov, V.I. Sobolev, O. V. Vodyankina, Effect of transition metal oxide additives on the activity of an Ag/SiO2 catalyst in carbon monoxide oxidation, Kinet. Catal. 54 (2013) 487–491.

[147] A.M. Garrido Pedrosa, M.J.B. Souza, D.M. a. Melo, A.S. Araujo, Cobalt and nickel supported on HY zeolite: Synthesis, characterization and catalytic properties, Mater. Res. Bull. 41 (2006) 1105–1111.

[148] P. Lahot, M. Rani, S. Maken, Separation and effect of residual moisture in liquid phase adsorption of xylene on Y zeolites, Brazilian J. Chem. Eng. 31 (2014) 497–502.

[149] M. Ziółek, Z. Dudzik, Influence of cation exchange on the structure and properties of Faujasite-type zeolites, React. Kinet. Catal. Lett. 12 (1979) 213–217.

[150] R.T. Yang, E.S. Kikkinides, New sorbents for olefin/paraffin separations by adsorption via p-complexation, AIChE J. 41 (1995).

[151] J. Padin, R.T. Yang, New sorbents for olefin/paraffin separations by adsorption via p-complexation: synthesis and effects of substrates, Chem. Eng. Sci. 55 (2000) 2607–2616.

[152] E.J. Baerends, D.E. Ellis, P. Ros, A theoretical study of the interaction of ethylene with transition metal complexes, Theor. Chim. Acta. 27 (1972) 339–354.

[153] A. Wooten, P.J. Carroll, A.G. Maestri, P.J. Walsh, Unprecedented alkene complex of zinc(II): structures and bonding of divinylzinc complexes, J. Am. Chem. Soc. 128 (2006) 4624–4631.

[154] T.I. Korfinyi, Comparison of (non)-sulfided NiNaY zeolite catalysts prepared by ion-exchange and impregnation by xenon adsorption and 129Xe NMR, Catal. Letters. 17 (1993) 105–116.

[155] D. Divakar, M. Romero-Sáez, B. Pereda-Ayo, A. Aranzabal, J.A. González-Marcos, J.R. González-Velasco, Catalytic oxidation of trichloroethylene over Fe-zeolites, Catal. Today. 176 (2011) 357–360.

[156] F. Holzer, U. Roland, F. Kopinke, Combination of non-thermal plasma and heterogeneous catalysis for oxidation of volatile organic compounds Part 1 . Accessibility of the intra-particle volume, Appl. Catal. B Environ. 38 (2002) 163–181.

[157] K. Hayashi, H. Yasui, M. Tanaka, S. Futamura, S. Kurita, K. Aoyagi, Temperature dependence of toluene decomposition behavior in the discharge–catalyst hybrid reactor, IEEE Trans. Ind. Appl. 45 (2009) 1553–1558.

LIST OF PUBLICATIONS

1. Q.H. Trinh and Y.S. Mok, Non-Thermal Plasma Combined with Cordierite-Supported Mn and Fe Based Catalysts for the Decomposition of Diethylether. Catalysts, 5 (2015) 800-814.

2. Q.H. Trinh and Y.S. Mok, Effect of the adsorbent/catalyst preparation method and plasma reactor configuration on the removal of dilute ethylene from air stream. Catalysis Today, accepted, doi:10.1016/j.cattod.2015.01.027.

3. Q.H. Trinh, S.B. Lee and Y. S. Mok, Removal of ethylene from air stream by adsorption and plasma-catalytic oxidation using silver-based bimetallic catalysts supported on zeolite. Journal of Hazardous Materials, 285 (2015) 525–534.

4. Q.H. Trinh, M. S. Gandhi and Y.S. Mok, Adsorption and plasma-catalytic oxidation of acetone over zeolite-supported silver catalyst. Japanese Journal of Applied Physics54 (2015), 01AG04.

5. Q.H. Trinh and Y.S. Mok, Plasma-catalytic oxidation of acetone in annular porous monolithic ceramic-supported catalysts. Chemical Engineering Journal, 251 (2014) 199–206.

6. H.Q. Trinh, J.O. Jo, S.B. Lee and Y.S. Mok, Preparation of red nitride phosphor from powder mixture of metal nitrides using spark plasma sintering. Current Applied Physics 14 (2014) 1051e1056.

7. Q.H. Trinh, S.B. Lee and Y.S. Mok, Hydrophobic Coating of Silicate Phosphor Powder Using Atmospheric Pressure Dielectric Barrier Discharge Plasma. American Institute of Chemical Engineers, 60 (2014) 829-838.

8. S.B. Lee, **Q.H. Trinh**, J.O. Jo, J.B Jung, T.H. Im and Y.S. Mok, Hydrophobic Coating on Fish Feed Using Dielectric Barrier Discharge Plasma Polymerization. Applied Chemical Engineering, 25 (2014) 174 – 180.

9. D.I. Jang, T.H. Im, **Q.H. Trinh**, J.O. Jo, Y.S. Mok, S.B. Lee and H.J. Ramos, Surface Coating Treatment of Phosphor Powder Using Atmospheric Pressure Dielectric Barrier Discharge Plasma. Applied Chemical Engineering, 25 (2014), 455-462.